Doctoral theses at NTNU, 2023:76

Eric James Ryan

Onshore to offshore correlation of ore-forming hydrothermal systems

Geological investigations of the Reinfjord Ultramafic Complex and Southwestern Barents Sea

Doctoral thesis

NTNU
Norwegian University of Science and Technology
Thesis for the Degree of
Philosophiae Doctor
Faculty of Engineering
Department of Geoscience and Petroleum

NTNU
Norwegian University of
Science and Technology

Eric James Ryan

Onshore to offshore correlation of ore-forming hydrothermal systems

Thesis for the Degree of Philosophiae Doctor

Trondheim, March 2023

Norwegian University of Science and Technology
Faculty of Engineering
Department of Geoscience and Petroleum

NTNU
Norwegian University of
Science and Technology

NTNU
Norwegian University of Science and Technology

Thesis for the Degree of Philosophiae Doctor

Faculty of Engineering
Department of Geoscience and Petroleum

ISBN 978-82-326-6754-3 (printed ver.)
ISBN 978-82-326-5879-4 (electronic ver.)
ISSN 1503-8181 (printed ver.)
ISSN 2703-8084 (online ver.)

Doctoral theses at NTNU, 2023:76

Printed by NTNU Grafisk senter

Abstract

Demand for mineral resources continues to grow, while political pressure, legitimate environmental concerns, and important ethical questions slow the development of new mineral resources. Simultaneously, emerging technologies promise to open new frontiers, and exploration into subsea mineral resources has been rapidly expanding. While Mid Ocean Ridges and other deep-sea deposits receive significant attention, fewer researchers have investigated near shore continental shelves. These domains are a continuation of onshore continental landmass, and as such are likely to contain similar resources those extracted on land today, in a setting possibly mitigating some environmental and ethical concerns. We consider the onshore – offshore correlation of ore-forming hydrothermal system and their presence on the Norwegian continental shelf, exploring various aspects of such hydrothermal systems at a variety of crustal depths.

The roots of hydrothermal systems can extend to great depths, with mantle isotope signatures commonly found in both mineral and hydrocarbon resources. We investigate structures at a variety of depths, from the lower crustal domain in the Reinfjord Ultramafic Complex to near-surface basins in the Barents Sea and exhumed continental crust on Bjørnøya, documenting the role hydrothermal fluids play in each setting. Finally, we extrapolate our knowledge from an onshore hydrothermal system to the offshore domain, correlating grand-scale structures and regional geology to relate Pb – Zn mineralizations on Bjørnøya to Pb – Zn mineralizations on the Loppa High. Our studies incorporate regional geophysical surveys, including potential field and seismic data, with field studies, sampling, fluid inclusion analysis, electron backscatter diffraction, electron microprobe analysis and more to create a detailed description of each field area.

Hydrothermal fluids play a major role in deformation at all crustal depths, enabling both shear and seismicity along lower crustal faults, and promoting faulting in shallow basinal settings. By investigating fluids and the structures along which the flow, we gain a better understanding of deformation processes at both lower and upper crustal depths. Finally, the grand-scale structures along which fluids flow allow us to trace mineralized hydrothermal systems from the onshore to the offshore domain, opening new frontiers in exploration geology.

Preface

This thesis is the result of a four-year PhD project at the Norwegian University of Science and Technology, Department of Geoscience and Petroleum (IGP), in Trondheim, Norway. The work has been carried out under the supervision of main supervisor, Associate Professor Bjørn Eske Sørensen, Professor Rune Berg Edland Larsen, Professor Christine Fichler, all of IGP, and Professor Giulio Viola at the Department of Biological, Geological, and Environmental Sciences at the University of Bologna, in Bologna, Italy.

The project included a total of one semester of course work, during which five courses were completed, including:

1. GB8105 - Applied Geophysics and Petrology for Exploration of Natural Resources
2. TPG410 – Seismic Interpretation
3. IFEL8000 – Research Methodology, Theory of Science and Ethics
4. AG836 – Rift Basin Reservoirs: From Outcrop to Model
5. DEEP9400 – Solid Earth – Fluid Earth Interactions

In addition, more than one year of duty work was completed, including the organization of practical microscopy exercises in TGB4125 Mineralogy and TGB4130 Petrology; the creation, organization, and evaluation of pandemic student projects in TGB4130 Petrology; field instruction of students on Elba for TGB4265 Advanced Structural Geology, and on Elba and in Cornwall for TGB4120 Prospecting and Formation of Selected Ore-Deposits; coordination with Petroleum Experts LTD for licensing of the Move™ software; publication of outreach material through NRK and the NTNU TechZone blog; assistance with the acquisition and operation of a DJI Phantom RTK drone; the assistance of masters-level students during field work in Reinfjord; and finally participation on the Norwegian Research School for Dynamics and Evolution of Earth and Planets board as the NTNU PhD representative.

Acknowledgements

While this PhD project has only lasted four short years, I have been roaming the halls of the Norwegian University of Science and Technology for over a decade! In that time, I have indebted myself to enough students, colleagues, laboratory researchers, professors, and other helpful people to fill this entire volume with names. Before that, before even moving to Norway, I learned the value of hard work, resilience, and focus through countless coaches, athletes, and teachers. For most of you, a single, but sincere thank you will have to suffice. Thank you.

I never imagined attempting a doctoral degree. Nothing was further from my mind in the Fall of 2012, when at a very early morning lecture I tried to understand Bjørn Eske Sørensen's explanation of miller indices. Crystal symmetry is complicated enough, without a Danish professor explaining things to a half-asleep American student, using a language in which we both have been considered mediocre, at best. I am still shocked that the wild Dane, pushing through a two-hour lecture in his cycling suit, with his helmet and cycling shoes tightly donned, and myself, a sleepy C-average student, find ourselves working together 10 years later, travelling the world and publishing articles in quality journals. It is unbelievable. Bjørn, thank you for the journey and your tremendous enthusiasm and dedication to your students and my project.

After mineralogy, my perspective on geology started to change, first through field courses and later comprehensive field work. Our class travelled around Norway and Europe; finally seeing what we had previously only read about in books. On Elba, structural geology and Professor Giulio Viola opened my eyes to a fascinating world where science and adventure merged. Investigating outcrops accessible only via open-water swimming or rappelling may not have improved our work, but it enlightened me. Elba and Giulio inspired me to stay in Norway and begin my masters and hopefully soon complete my doctoral degree. Thank you, Giulio.

During this project, my advisors Bjørn Eske Sørensen, Rune Berg Edland Larsen, Christine Fichler, and Giulio Viola guided me every step of the way. I sincerely thank you all, for your patience, hard work, thorough reviews, and engagement. Some of us have had the privilege of travelling to Reinfjord, Svalbard, and Bjørnøya, to name a few. Oddmund Hansen

graciously hosted us in Reinfjord, where helicopters, boats, ATV's and a jacuzzi ensured successful field seasons, despite the arctic weather's best efforts. On Svalbard, I participated in an incredible course, led by Professors Alvar Braathen, Jan Tveranger, and Per Terje Osmundsen. I was fortunate enough to join a rare group of exceptionally talented geologists and even better people. Whether you end up in the industry, academia, or something entirely different, the world of geology is lucky to have you and we are lucky to call you friends. Finally, our voyage to Bjørnøya, by sailboat, impacted my future more than I could imagine. For an incredible Arctic journey and one of life's defining moments, I thank Captain Martin Halvorsen and Professor Atle Mørk, for his coordination and personal sacrifice in making the trip possible and covering its cost.

I thank my parents for enduring the challenge I was as a boy, taking me sailing, turning me into a skier, and putting up with a son on the other side of the globe for the last 14 years. Both my sister and I are unbelievably fortunate to have received so much love and support. And my sister, thank you for always being my big sister. Your daughter came at the perfect moment to distract me from challenges that often seemed insurmountable, with endless cuddles, laughs, and love.

I thank my in-laws, for giving Marte and I the freedom to live out our dreams and supporting us constantly, despite our wild schedules and unorthodox plans. And finally, I thank my wife Marte, the hardest to thank because it is impossible to thank someone for all that there is. Together we have made bold decisions in uncertain times, and diligently worked through challenge and opportunity with uncommon dedication and some sacrifice. The end of this PhD project is for us not the end of sleepless nights, weeks spent at the keyboard, and moments of pressure and consequence, but rather the beginning. Thank you for joining me on our journey, the likes of which few are privileged to live. It is only fitting that as I write this you are sitting next to me, halfway across Vestfjorden, both of us rocking in the waves with computers in our laps, working hard towards our future, and not seasick yet. Let's remember to leave our laptops behind and head out on deck, a little more often than we have so far.

See you on the seas,
Eric

Table of Contents

1 Rationale

The demand for mineral resources grows higher year by year (Hannington et al., 2017). Emerging economies, expanding populations, and a push towards a more sustainable future all contribute to this growth, which is expected to continue until the end of the 21st century (Vidal et al., 2021). Simultaneously, political pressures, legitimate environmental concerns, and important concerns regarding human rights and working conditions make the development of new resources difficult (Bebbington et al., 2008; Lawrence and Moritz, 2019), if at times not impossible. This balance between high demand and difficult development inspires academics and prospectors alike to search for mineral resources in new frontiers. One frontier garnering increased in the subsea domain, both far offshore (Hein et al., 2013; Wedding et al., 2015) and along submerged continental shelves (Hannington et al., 2017).

International organizations, mining companies, and governments have begun to show more and more interest in offshore mine development (Hein et al., 2013; Wedding et al., 2015; Hannington et al., 2017). As interest grows, funding is directed towards research groups focusing on topics relevant to offshore mineral development, making more, higher-quality research a reality. In Norway, the petroleum industry has surveyed parts of the ocean space for decades, creating enormous publicly available datasets, fostering a willingness to cooperate with researchers at academic institutions in Norway and abroad. Oceans, and particular Mid Ocean Ridges (MOR) receive wide-spread attention regarding their mineral resource potential (Hein et al., 2013; Hannington et al., 2017), although mineral extraction and even prospecting, along these distant structures seems exceedingly difficult (Hannington et al., 2017). The combination of increased funding, growing demand, and the availability of critical datasets has opened the door for increased exploration of continental shelves.

Continental shelves contain a variety of important mineral deposits (Rona, 2008), many of which have been critical for global development. Approximately one-third of continental land masses are submerged beneath shallow seas as continental shelves (Harris et al., 2014). The submerged shelf areas are likely to contain similar mineral deposits to those on land and could

help meet future mineral demand if developed responsibly (Hannington et al., 2017; Beaulieu et al., 2017). In contrast to MOR deposits, continental shelves are near shore, reducing logistical challenges and the likelihood of inclement weather negatively affecting both exploration and production in the MOR domain (Lesage, 2020; Ellefmo, 2022). Important environmental concerns may be more manageable along shelves than at MOR, following our increased understanding of these environments when compared to their deep MOR counterparts. Finally, continental shelves are, owing to their significant hydrocarbon potential, frequently well-mapped and well-explored. Considering this, continental shelves have the potential to help meet future mineral demand and contribute to the sustainable development of society.

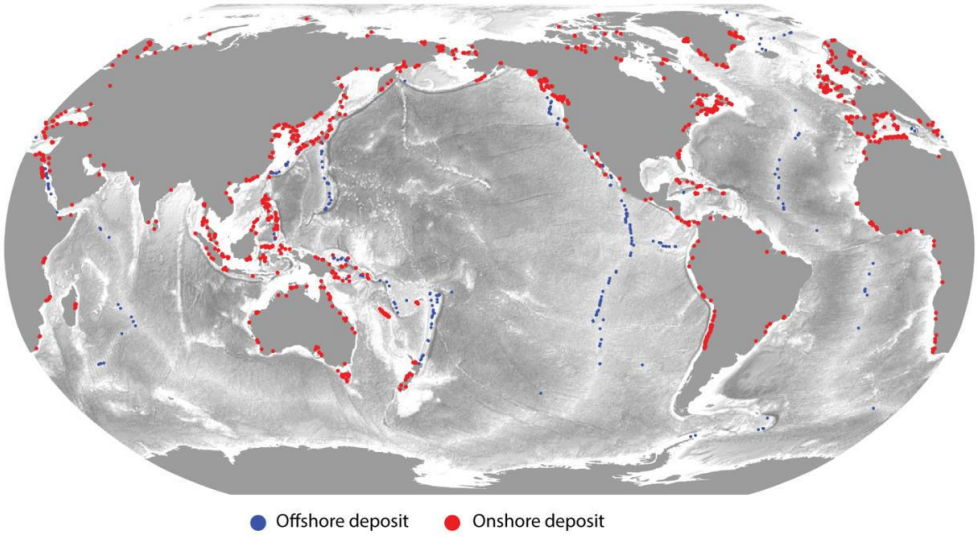

Figure 1.Map of global offshore sulfide and onshore coastal deposits, modified from Hannington et al. (2017).

Through basic research and an increased understanding of mineral systems, we hope to help meet future mineral demand in a responsible manner. There is a significant knowledge gap

between the knowledge required to develop offshore mineral resources sustainably and responsibly, and that which we have today (Hannington et al., 2017; Miller et al., 2018; Van Doorn et al., 2022). We hope that this work will help to resolve this knowledge-gap, and, if possible, through sustainable and environmentally acceptable practices, contribute to the development of mineral resources on continental shelves

2 Aims and objectives

The “Onshore-offshore correlation of ore-forming hydrothermal systems” is an enormous topic. Such a correlation encompasses the breadth of geological and geophysical disciplines, a challenge for any project. This thesis tackles the problem from a structural geological perspective, while drawing on geophysical data, geochemistry, and extensive microanalysis, strengthening our conclusions. To further narrow the scope of our work we developed clearly defined research goals, which we have endeavored to answer.

2.1 The role of hydrothermal systems in deep rift settings

The deepest reaches of hydrothermal systems are severely underexplored. By investigating the lower crustal Reinfjord Ultramafic Complex and structures related to the exsolution of hydrothermal fluids at more than 40 km depth, we attempt to describe the role of hydrothermal systems in deep rift settings. Recent studies have demonstrated a link between deep earthquakes and the exsolution of fluids at Earth’s surface (Lee et al., 2016), and deep-fluid signatures are present in both hydrocarbons (Finlay et al., 2010; Fetter et al., 2019) and important sulfide deposits (Blundell et al., 2003; Schmidt Mumm and Wolfgramm, 2004). By investigating the spectacularly preserved outcrops of the Reinfjord Ultramafic Complex we aimed to better understand deformation processes and fluid migration through the lower crust

2.2 The role of hydrothermal systems in island arc deposits

Island arcs are associated with a variety of mineral deposits. This project aimed to investigate the Lykling gold deposits, in the Bømlo region of southwestern Norway. The gold deposit is emplaced within the Lykling Ophiolite, the volcanic and sedimentary Geitung Unit (494 ± 2 Ma), and the subaerial volcanic and sedimentary Siggjo Complex (473 ± 2 Ma) (Nordås et al., 1985; Pedersen and Dunning, 1997). Island arc deposits are often associated with hydrothermal systems, spawning from intrusive bodies emplaced in arcs (Mitchell and Bell, 1973). Common deposit types include mercury, porphyry copper, and gold veins, like those mined around

Lykling. Large faults play an important role in the development of island arcs, including control over magmatic emplacement and the creation of faults systems (Leclerc et al., 2016), the latter of which may act as fluid pathways with the potential to exert a direct control on mineral deposits. Our study aimed to describe in detail the genesis of the Lykling gold deposit, from a structural and geochemical perspective, and potentially extrapolate our findings to the near-shore coastal domain and other arc settings.

2.3 The role of hydrothermal systems in epithermal deposits on continental shelves

Continental shelves contain some of the largest mineral deposits known (Hannington et al., 2017). Most shelves are unexplored, as they are submerged beneath shallow seas forming a barrier between prospecting geologists and their quarry. Up to one-third of continental land mass, like that which is explored in land today, is hidden beneath near-shore seas (Harris et al., 2014), indicating a significant potential to uncover new mineral resources within these areas. Our study investigates a known hydrothermal mineralization on Bjørnøya (Flood, 1967) in the Barents Sea, and aims to compare this with other similar mineralizations in the surrounding submerged continental shelf, providing an onshore – offshore correlation of hydrothermal mineral systems. We describe in detail the structural setting, fluid source, and timing of potential mineralizations, creating an ore formation model for the Pb – Zn mineralizations in the Barents Sea.

2.4 The extrapolation of onshore data to the nearshore and offshore domains

The lower, mid, and upper crustal domains all present unique opportunities at the intersection of structural and ore geology. Using large crustal scale structures visible in seismic and potential field data, as well as field and well core data, we aim to uncover new areas for mineral exploration on the Barents Sea and provide a methodology for extrapolating land-based knowledge to the offshore domain in other continental shelf regions. Large crustal-scale fault, which are easily recognizable in geophysical data (Gernigon and Brönner, 2012; Gernigon et al., 2014; Gernigon et al., 2018), may contribute to fluid migration in rifted basinal settings

(Curewitz and Karson, 1997). By combining geophysical and lithological data we extrapolate detailed onshore ore-system knowledge to the offshore domain.

2.5 Deliverables

To disseminate our work, we created a detailed publication plan including both research articles and conference presentations. The body of this thesis (Chapter 1, 2, and 3) constitutes most of this work in the form of three peer-reviewed journal articles:

(1) Infiltration of volatile-rich mafic melt in lower crustal peridotites provokes lower crustal earthquakes (Ryan et al., 2022)
(2) Fault-linkage on Southeastern Bjørnøya: Implications for structural interpretations surrounding fertile ore-forming fault systems in the offshore domain
(3) Genesis of Pb – Zn mineralizations in the Barents Sea and consequences for offshore ore exploration on continental shelves

In addition to the journal articles, we disseminated our work through international conferences including the Geological Winter Conference, The Nordic Geological Winter Meeting, and the Fall Meeting of the American Geophysical Union. A complete list of publications both relating to and completed in parallel to this thesis is available in section 12. We hope this thesis answers the research questions and enlightens our readers regarding the present knowledge and still-unanswered-questions regarding the onshore-offshore correlation of ore-forming hydrothermal systems.

3 Explored avenues

This PhD project started with a broad investigation of a variety of avenues, aiming to address our research questions. Our ambitious plan was to document ore-forming hydrothermal systems at lower crustal, mid-crustal, and upper crustal levels and relate these to present day Norwegian coastal and continental shelf geology. While some avenues were further explored and resulted in journal articles, others were cast by the wayside at early stages in their development. The latter investigations still provided valuable results and useful insights, some of which are detailed here.

3.1 Near-shore extrapolation using geophysical data along coastal Norway

This project began with a nationwide cartographic investigation, correlating areas of mineral interest onshore to large-scale structures in the offshore domain. Using public data from the Geological Survey of Norway (NGU), the Geological Survey of Finland (GTK), The Norwegian Petroleum Directorate (NPD), potential field data from Olesen et al. (2010), as well as geochemical and seismic data from Aker BP and Lundin, we aimed to extrapolate onshore knowledge and mineral deposit plays to the offshore domain (Fig. 2), by comparing onshore mineral provinces, with potential field data and grand-scale fault complexes and shear zones. Our findings were presented through a variety of conference proceedings (Section 15). Ultimately, inherent challenges regarding data and methodology resulted in a redirection of our focus to other areas of investigation.

While interesting, this method is significantly limited by the resolution and ambiguity of available geophysical data, the scarcity of deep bore holes, a lack of constraints in the “well-known” onshore domain, the miniscule target size of ore deposits regarding both potential field and seismic resolution, and most critically the geological configuration of the Norwegian coastline. The latter being characterized by a series of east to east-southeast verging nappes which change rapidly in a direction roughly normal to the coast, i.e., there is not necessarily a correlation between onshore and offshore geology, even in the relatively near-shore domain. Considering these challenges, we found it prudent to focus our efforts on the more promising

aspects of this PhD project, two of which – the Lykling gold deposit and the Bjørnøya Pb – Zn mineralization were identified through this ultimately abandoned cartographic investigation.

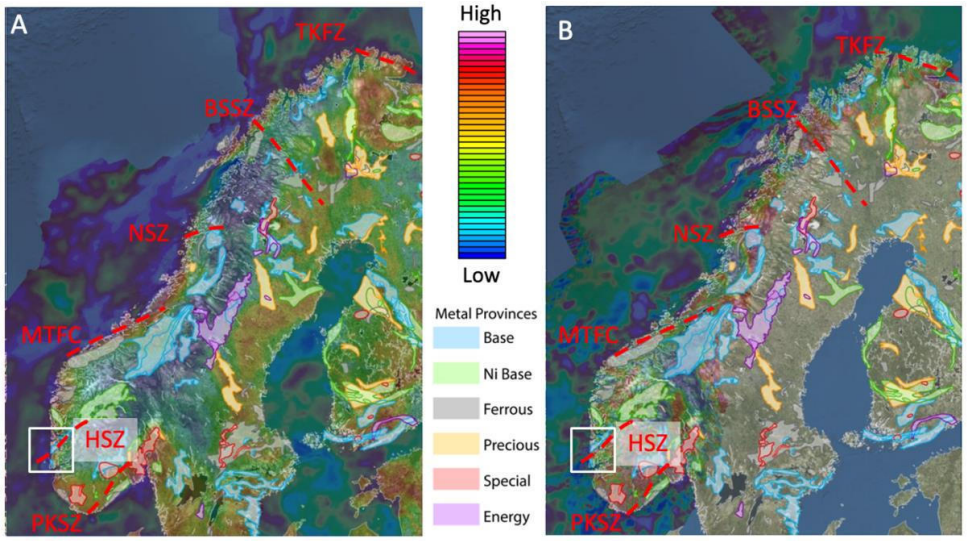

Figure 2. (A) Gravity and (B) magnetic anomaly maps from the Geological Survey of Norway, with mineral provinces for base, Ni base, ferrous, precious, special and energy metals from the Geological Survey of Finland. (TKFZ) Trollfjord Komagelv fault zone, (BSSZ) Bothnian - Senja shear zone, (NSZ) Nesna shear zone, (MTFC) Møre Trøndelag fault complex, (HSZ) Hardangerfjord Shear zone, (PKSZ) Porsgrun Kristiandsand shear zone. Modified from (Ryan et al., 2019).

3.2 Bømlo and the Lykling gold deposit

One of the area's identified through out coastal mapping investigation included the Lykling Gold Deposit, located in Bømlo, southwest Norway and emplaced within island arc ophiolite complex formed originally as a part of the Iapetus ocean (Nordås et al., 1985). Following the Caledonian orogeny, extension along major detachments, such as the Hardangerfjord shear zone (Fossen and Hurich, 2005) reworked the Lykling Ophiolite. This deformation is reflected by the ubiquity of extensional structures in the area. Large, up to 2 meter wide quartz veins cut across the ophiolite, exploiting the contacts between intermediate dykes or shear zones and the host rocks (Amaliksen, 1980). Previous fluid inclusion studies indicate that the gold was emplaced with

these quartz veins at epi- to mesothermal conditions (Wullf, 1993). Considering its near shore position and potential relation to both traceable tectonic lineaments and major tectonic events, we considered the Lykling Gold Deposit an interesting candidate for further work regarding the role of hydrothermal fluids in structural ore settings.

We spent 10 days in the field, mapping, collecting samples and creating 3D outcrop models throughout the Lykling deposit. We observed numerous, subvertical (85 – 90°) NE-SW trending quartz veins with lineations indicating oblique slip in a transtensional environment. Many of the veins formed along dolerite dykes, which themselves contain significant quantities of sulfide minerals. A second subset of veins trends to the WNW-ESE, forming a conjugate set of faults with the primary vein structures. The well-preserved structures with exceptional exposure allow for a detailed tectonic reconstruction of the paleo-stress field and tectonic setting. To investigate other relevant factors regarding the mineralization we took numerous samples, prepared 24 thin sections, and planned a detailed isotope and fluid inclusion study. Unfortunately, this work was abandoned for reasons beyond our control.

Following the onset of the COVID-19 pandemic, we chose to limit any further work in Lykling due to constraints regarding the planning of new field seasons, the shutdown of all laboratories and the university, and other challenges related to the pandemic lockdown. Considering the new time constrains, we directed our focus the Reinfjord Ultramafic Complex and Bjørnøya-based sections of our study. While we did little to develop our research on Lykling, apart for the early workings of a draft manuscript, we hope our data may come of use through student projects or future work at the Norwegian University of Science and Technology.

3.3 Bjørnøya – further investigations into isotopic and geochronological histories

Our work on Bjørnøya, presented in detail in chapters 2 and 3, sought to unravel the structural and ore-forming history of the Pb – Zn deposit on Bjørnøya and other potential deposits in the Barents Sea Region. A significant part of this work aimed to date the mineralization and coeval structural features which we documented on Bjørnøya. Unfortunately, these efforts failed. We were unable to date the mineralization using and radiogenic isotope methods, including Rb/Sr at

the Scottish Universities Environmental Research Centre (SUERC), U/Pb and the Geological Survey of Norway (NGU). In each case, Rb and U levels were below detection limits. A final attempt was considered using the Re-Os system at the Canadian Centre for Isotopic Microanalysis (CCIM), however considering the complete lack of Fe-sulfides in large-enough quantities for an isotope study, we abandoned these following the advice of CCIM. Still, through our work we were able to suggest limited age constrains, helping to place the hydrothermal and structural events into a broader geological framework. We hope our failed attempts will help guide future work trying to tackle the dating-question in the Bjørnøya and Barents Sea region.

4 Geological background

4.1 Norwegian geology and the Caledonian Orogeny

Stretching from the Archean to recent times, Norway displays a rich geological history (Torsvik and Cocks, 2005). While the buildup and collapse of the Caledonian Orogeny dominates this story, the bulk of our work is based on investigations of pre-Caledonian rocks. The following overview highlights key events through time creating a framework which the events documented in this thesis may be inserted.

The paleocontinent Baltica, beneath present day Northern Europe, the Atlantic and Barents Sea continental shelves, and stretching east to the Caspian Sea ad Ural mountains, formed through a series of rift and collision events, starting with the Rodinian supercontinent 1 Gyr ago (Cocks and Torsvik, 2005). The late Paleoproterozoic NW-SE trending collision between Archean terranes and Paleoproterozoic crust, known as the Svecofennian Orogeny, deformed the northeast section of the Baltic shield (Daly et al., 2006). In the Mesoproterozoic and Neoproterozoic, the WNW-ESE trending Timian orogeny affected the region, as assemblages from a Paleocene ocean were accreted onto the northeastern margins of Baltica during the Late Vendian (ca. 600 – 570 Ma) period (Roberts and Siedlecka, 2002).

As a part of Rodinia, Baltica was connected with the Laurentian terrane from which many of the Caledonian nappes would eventually be derived (Cocks and Torsvik, 2005). Baltica and Laurentia were separated during a period of rifting and ocean spreading, forming the Iapetus Ocean. The timing of this event is contested, with estimates ranging from 700 to 550 Ma (Robert et al., 2021). Recent estimates place the opening of the Iapetus around 590 Ma and relate the rifting event to the emplacement of the Central Iaeptus Magmatic Province (Ernst and Bleeker, 2010). Through the Cambrian, the margins of Baltica were tectonically very active, while the craton itself formed a shallow platform (Cocks and Torsvik, 2005) from 544 to 490 Ma. At the end of this period, the Iapetus Ocean reached its maximum extent, before a change in geodynamics led to a closure of the ocean. The closure of the Iapetus Ocean began in the early Ordovician, with the subduction of oceanic crust beneath both Laurentia and Baltica (Gee et al.,

2008). As the ocean closed during the mid to late Silurian, Laurentia was subducted beneath Baltica, forming the Caledonian orogeny (Gee, 1975; Torsvik and Cocks, 2005; Gee et al., 2008).

The Caledonian Orogeny, resulting from the collision of Baltica, Laurentia and possibly a number of smaller terrains, (Corfu et al., 2014) set the stage for Norway's present-day geology. Starting during the Silurian, around 425 Ma, Baltica collided with and was subducted beneath Laurentia, accreting nappes and possibly smaller terranes in the process (Torsvik and Cocks, 2005; Corfu et al., 2014). As the north to north-northeast trending Caledonian thrust front migrated across Norway from with an easterly to east-southeasterly vergence, coeval extension and transtension began in the hinterland forming crustal-scale detachments and educting eclogite facies rocks (Andersen et al., 1991). The collapse of the Caledonian orogeny has been followed by multi-stage rifting since the late Paleozoic resulting in important sedimentary basins along the Norwegian continental shelf and eventually the opening of the Atlantic Ocean and Norwegian Greenland Sea.

The events documented in this thesis are snapshots of this long geological history. From the Ediacaran magmatism which forming the Seiland Igneous Province (Larsen et al., 2018) to the Carboniferous rifting surrounding Bjørnøya in the Southwest Barents Sea (Worsley et al., 2001), we investigate the specific moments in time during which the geology was of particular interest to understanding hydrothermal mineral systems, across a transect of crustal levels. We hope that our results shed further light on how Norway and the mineral deposits on the surrounding continental shelves developed.

4.2 The Seiland Igneous Provence

The Seiland Igneous Province (SIP) lies within the Central Iapetus Magmatic Province (CIMP), which formed across Baltica and Laurentia over a period of 100 Mya, starting around 620 Ma. The CIMP is preserved as a spread of large igneous provinces across Northeastern Canada, Greenland, Northern Norway, and Svalbard (Roberts et al., 2006). The SIP itself covers over 5000 square kilometers and contains four ultramafic igneous bodies and six deep roots extending to at least 9 kilometers depth (Roberts et al., 2006; Pastore et al., 2016; Larsen et al., 2018). The

ultramafic rocks were emplaced at depths between 25 and 35 kilometers into lower crustal gabbros (Larsen et al., 2018). The timing of the SIP is loosely constrained the Ediacaran between 570 and 560 Ma and is geochemically correlated to Scandinavian magmatism between 610 and 560 Ma (Roberts et al., 2006; Larsen et al., 2018). The magmatic rocks comprising the SIP are particularly fertile, with early komatiitic to picritic dykes containing 16–22 wt% MgO, 611 ppm Ni, and 1594 ppm Cr, as well as between 0.5 and 1 % magmatic sulfides and local PGE-Cu-Ni reefs, as in the Reinfjord ultramafic complex (RUC) (Fig.3) (Larsen et al., 2018).

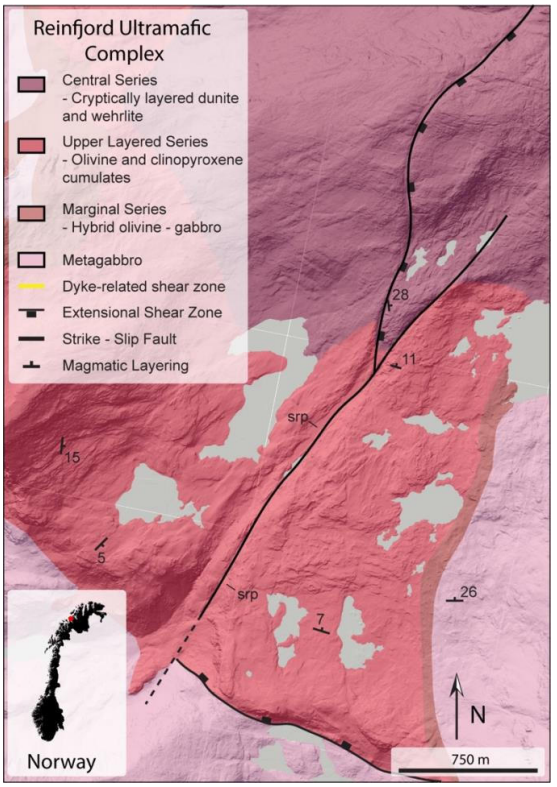

Figure 3. Map of the Reinfjord Ultramafic Complex, modified from Ryan et al. (2022).

Our field study was conducted entirely within the RUC, a near-vertical and concentric conduit system for mantle derived melts (Grant et al., 2016; Larsen et al., 2018) with spectacular examples of magmatic (Grant et al., 2016; Larsen et al., 2018) and tectonic (Sørensen et al.,

2019) structures. The magmatic rocks of the RUC were emplaced in series including gabbronorite, pyroxenite and peridotite bearing stages, divided into a lower-layered, upper-layered and central series of ultramafic rocks emplaced within the Langstrand gabbronorite (Grant et al., 2016; Larsen et al., 2018). The complex also hosts significant marginal zones at the contact with the gabbroic host rock and Cu-Ni-PGE reef deposits (Larsen et al., 2018). This project, following the work of Sørensen et al. (2019) aimed to further investigate the tectonic structures and their role in facilitating fluid migration within the lower crust.

Ore-forming processes with the SIP and RUC necessitate significant volatile fluxing of both sulfuric and carbonic fluids (Larsen et al., 2018). Many of the sulfides observed within the RUC are directly associated with shear zones containing carbonate and plagioclase with numerous CO_2-rich fluid inclusions. The presence of CO_2 may aid in the precipitation of some metals (Lowenstern, 2001), particularly through a corresponding increase in oxygen fugacity, reducing the solubility of sulfur in dykes associated with the shear zones, causing sulfur saturation and segregation, as described by Piaoer et al. (2012) for the Kalatongke Cu-Ni sulfide deposits in Western China. CO_2 is further suggested to play a role in moving sulfides from the mantle to higher crustal levels (Blanks et al., 2020). Finally, recent studies link the fluxing of CO_2 fluids to deformation and the formation of structures along which more fluids may migrate in the RUC and other ultramafic rocks (Sørensen et al., 2019), indicating that the presence of CO_2 fluids is critical for both sulfide mineralizations and the flux of both sulfide compounds and CO_2 to higher crustal levels along specific structures.

Sørensen et al. (2019) describe numerous extensional shear zones and brittle faults within the RUC, all formed at lower crustal depths. The shear zones range from sub-millimeter to centimeter scale in width, and are associated with reaction between olivine, clinopyroxene and CO_2, reacting to form dolomite and enstatite, two order of magnitude grain size reduction, and the formation of some pseudotachylytes. Reaction-related strain softening and fracturing following volume-expanding carbonation reactions enabled progressive deformation along the shear zone and the migration of deep fluids to higher crustal levels. The geometry and development of these structures, and their relation to fluid migration, is investigated in detail in section 9 of this thesis.

4.3 The Barents Sea

A variety of collisional and rifting events have formed what is the present-day Barents Sea (Fig. 4), now a passive margin dominated by stable sedimentary basins (Faleide et al., 2008). The Svecofennian, Timian and Caledonian orogenies have all affected the crustal structure and composition beneath the Barents Sea. Similarly, the development of the SIP, RUC and similar magmatic intrusions in the Barents Sea (Fichler and Pastore, 2022) and on Svalbard (Gumsley et al., 2020), associated with the break-up of Rodinia and opening of the Iapetus ocean (Hartz and Torsvik, 2002; Robert et al., 2021) or continental arc magmatism (Koehl et al., 2022), have altered the composition and geometry of the region.

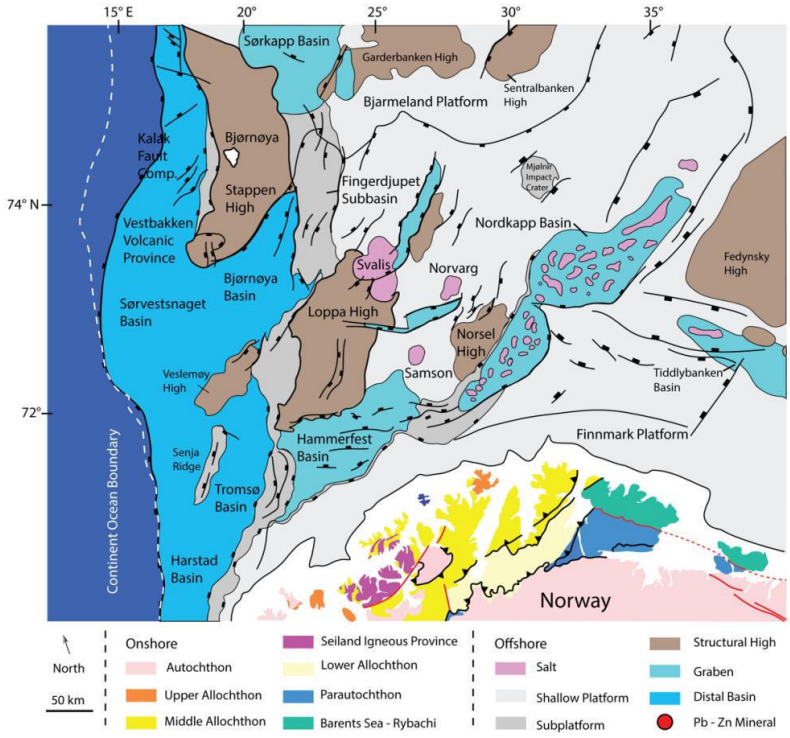

Figure 4. Map of the Barents Sea region, modified from Gabrielsen et al. (1990), and Gernigon and Brönner (2012).

Recent work relates the recent development of the Barents Sea region with the structural and lithological records of these ancient events. The reactivation of Caledonian structures in the Barents Sea is often implicated in later tectonic events (Ritzmann and Faleide, 2007; Gernigon and Brönner, 2012; Gernigon et al., 2014; Blaich et al., 2017). Gresseth et al. (2021) convincingly document the influence of structures formed during post-Caledonian orogenic collapse on Late Paleozoic and Mesozoic basin development, while Serck et al. (2017) describe a similar occurrence within the Fingerdjupet Subbasin (Fig. 04). Gernigon et al. (2018) document the influence of both Caledonian and even Timian structures on the development of younger basins and basement highs elsewhere in the Barents Sea. The current geometries of both the Loppa (Indrevær et al., 2017) and Stappen (Worslex et al., 2001) Highs are heavily influenced both the existence of deep paleo-structures, namely the Selis Ridge and Paleo-Stappen High. The deep structures delineating the structural highs in the Barents Sea had the potential to act as fluid conduits, which in conjunction with a number of other features may create ore-forming systems, as described by Robb (2004). CO_2-outgassing in major continental rifts (Lee et al., 2016) and the presence of mantle isotope signature in carbonate-hosted epithermal Pb-Zn deposits (Davidheiser-Kroll et al., 2014) highlight the link between the deep structures and upper crustal resources.

The resource potential of passive margins and sedimentary basins is well-documented, particularly on land (Arndt et al., 2017). No work has been done regarding the exploration of mineral resources in the Barents Sea, apart from the subaerially exposed Bjørnøya Pb – Zn deposits, described by Flood (1967) and a number of unpublished reports, and a slightly more substantial, though still limited, body of work regarding mineral deposits located on the more distal Svalbard (Flood, 1967; Segalstad, 2006; Boyd et al., 2016). Despite this, the submerged basins of the Barents Sea are very likely to contain significant mineralizations, based on the wide-spread presence of deposits in similar geological settings elsewhere (Leach et al., 2005). Geological constraints surrounding both Bjørnøya and the Loppa High indicate that they may lie within fertile ore-settings.

Bjørnøya, positioned near the center of the Stappen High (Fig. 4), was first mapped and described in detail by Andersson (1901) and Holtedahl (1920), the latter of which took a

particular interest in the pre-Caledonian Hecla Hoek basement rocks. Since then, a few studies have unraveled the geological history of Bjørnøya and placed it within a greater Barents Sea context (Lepvrier et al., 1989; Braathen et al., 1999; Worslex et al., 2001). Three units predating the Caledonian Orogeny are exposed on Bjørnøya, including the 650 – 541 Ma Russehamna formation, the 485 – 470 Ma Sørhamna formation and the 470 – 458 Ymerdalen formation (Worslex et al., 2001). Together these units comprise the Hecla Hoek, and record a polyphase deformation history dominated by Caledonian structures which have been sequentially reactivated during later rift events (Lepvrier et al., 1989; Braathen et al., 1999). NNE-SSW trending, ESE-dipping thrusts, formed between the Middle Ordovician and Late Devonian, and were reactivated during subsequent deformation phases (Braathen et al., 1999; Worslex et al., 2001). This relatively complex history of ancient structures and multiphase reactivation is not unique for Bjørnøya, but rather typical of the Barents Sea (Ritzmann and Faleide, 2007), including the Loppa High.

The Loppa High (Fig. 4) formed around the Selis Ridge, a paleo-high created during periods of rifting starting in the Carboniferous (Gudlaugsson et al., 1998; Glørstad-Clark, 2011; Clark et al., 2014; Gac et al., 2018). Within the Loppa High and Selis Ridge, Koehl et al. (2022) identify overturned, isoclinal, and recumbent folds, as well as major shear zones, which they attribute to the Timian orogeny based on sub-parallel structural trends, as well as structures relating to the Caledonian Orogeny. A number of magmatic bodies have been identified within the Loppa High, mainly based on the interpretation of potential field data (Indrevær et al., 2018; Fichler and Pastore, 2022). Both the paleo-structures and magmatic bodies have been reworked during a series of rift events from the Late Paleozoic to the Paleogene, forming the structure's present configuration (Gabrielsen et al., 1990; Faleide et al., 1993; Green and Duddy, 2010; Glørstad-Clark, 2011; Indrevær et al., 2017).

5 Methods

Our project employs a variety of investigative methods across all scales, from satellite-based potential field measurements to optical and electron microscopy and the description of minute micrometer-scale structures. This approach helps create a complete picture of our investigative targets, namely mineralized hydrothermal systems, at all scales. Detailed methodology for each method is provided in the relevant journal articles. Here, we describe our rationale for choosing the methods in more general terms.

5.1 Geophysical interpretation

Satellite and aerial surveys of the gravimetric and magnetic fields provide an outstanding overview of large-scale structures and crustal compositions, which are not always visible at Earth's surface. Our study relies on such data to describe the regional setting of Pb – Zn mineralizations on the Barents Sea continental shelf, where other data sources are extremely limited. At smaller scales, we use magnetic data collected along flight lines intersecting our field area on Bjørnøya to model a structural and lithological profile across the mineralized area, helping constrain the geometry and composition of the subsurface beneath the Pb – Zn mineralization. Potential field data does have some limitations, including an inherent ambiguity only resolvable through complementary datasets and geological interpretation. In addition, the data used in our study is relatively low-resolution, providing a relatively coarse subsurface resolution.

Seismic time sections provide a more detailed image of the subsurface, including lithotypes, structures, and fluid pathways. Lundin Energy provided two time-sections stretching across the Loppa High, through well 7220/11-3. The relatively high resolution of the time sections allows us to observe the network of faults and deep detachments related to the Loppa High, and a key component of the hydrothermal systems which formed the Pb – Zn mineralizations. The seismic data is complimented by our investigation of well core 7220/11-3, providing detailed lithological constraints for our study and important sample material, including sphalerite and galena-bearing assemblages, with baryte, minor fluorite and accessory pyrite.

5.2 Field surveys

To cover the massive scale gap between regional geophysical data and physical field investigations, we rely on LiDAR data and digital elevation models (DEM) to help visualize and model the topography across our field regions. DEM are particularly useful for mapping lineaments, which we then incorporate into lineament analyses. These analyses provide a useful picture of structural trends, which are often difficult to observe in the field. Both the Reinfjord Ultramafic Complex and Southeastern Bjørnøya are covered by high resolution DEM. Fortunately, shallow sediments and preferential erosion along physical structures in both Reinfjord and Bjørnøya make the DEM particularly useful.

The structures mapped in DEM are complemented by 3D outcrop models, created using both handheld and aerial platforms while in the field. These models have several advantages. When georeferenced, detailed structural measurements are possible using inexpensive software from the comfort of the office. This makes the creation of statistically accurate datasets significantly easier and less expensive, if not a little more tedious. In addition, the models may provide useful insights during interpretation, offering a new "field" perspective which we refer to during later data interpretation and discussion, and provide maps on which one can place the location of samples and observations, helping organize data as collected in the field. Unfortunately, the models are still difficult to share. Ideally, they would be included as regular figures in online and PDF journal articles, aiding communication with fellow scientists. In this work, we include the models only as 2D images.

Field observations and sampling provide the basis for all our studies. Detailed and georeferenced observations of structural, lithological, and textural relationships bring the geology from the real world into our communicative channels. Using the FieldMove ™ software created by Petroleum Experts Ltd we organize all our data instantly in the field, and rapidly expert datasets to ArcGIS Pro ™. The combination of FieldMove ™ and ArcGis Pro ™ leads to efficient map making and interpretation, allowing us to get the most out of our field data.

5.3 Microscopy

The samples we collect in the field a further prepared at the Norwegian University of Science and Technology, Department of Geoscience and Petroleum Sample Laboratory. We cut the samples along targeted planes, generally along the stretching lineation and normal to the foliation. The optical microscope allows us to observe microstructures and microtextures within our samples, often supporting the observations we make in the field and sometimes providing surprising new information. Together with the thin section scanner and high-resolution camera, we gather detailed data from our samples, traceable back to outcrops and field sites. To dive deeper into our samples, we use scanning electron microscope (SEM) and electron microprobe analyses (EPMA), investigating the micrometer domain.

Using the SEM, we employ energy-dispersive X-ray spectroscopy (EDS) to confirm the presence of specific minerals in our thin sections and grain samples. Backscatter and secondary electron images provide extremely high resolution (< 0.5 μm) of mineral phases and textures in samples, helping discern crystallization order and mineral relationships in the rocks. Our samples textures may be further analyzed through electron backscatter diffraction (EBSD). EBSD data quantifies both mineral phases and the orientation of crystals and the lattices. The maps in this study employ step sizes as low as 1 by 1 μm. The subgrain and intragrain structures revealed through EBSD are important observations for documenting specific deformation processes in rocks, which we rely extensively in the Reinfjord Ultramafic Complex.

Finally, we employ EPMA to gather quantitative composition data for mineral phases our samples. The quantitative data are used for thermodynamic modelling and allow for a precise comparison with other geological datasets. In addition, quantitative maps provide detailed information regarding the elemental content within specific crystals and crystal zones.

5.4 Radiogenic and stable isotope analysis

Isotope analyses provide vital information for understanding the formation of ore deposits and mineralizations. We measured sulfur and strontium isotope ration in sulfide and sulfate minerals from Bjørnøya and the Barents Sea. The analyses allow us to suggest a source for the sulfur and provide information regarding the fluid source in the mineralizing hydrothermal systems. This,

when combined with a regional geological study and other data, helps us a create a model for the genesis of the mineralizations.

5.5 Fluid inclusion analysis

To better understand the mineralizing fluids themselves, we analyzed fluid inclusions in calcite and sphalerite related to the Pb – Zn mineralization on Bjørnøya. Through heating and cooling the inclusions we observe freezing, initial melting, ice melting and homogenization temperatures between the fluid and gas phases in the inclusions. When interpreted through numerical modeling, these measurements provide detailed information regarding the salinity and density of the fluid within the inclusion, and isochores for the crystallization of the mineral. This information, when combined with regional geothermal gradients and geological understanding allow us to suggest the pressure and temperature conditions during the formation of the mineralization.

6 Summary and key findings of published work

6.1 Infiltration of volatile-rich mafic melt in lower crustal peridotites provokes lower crustal earthquakes

This paper, based on our observations of lower crustal extensional shear zones in the Reinfjord Ultramafic Complex, describes the formation of the shear zones in relation to mafic dykes, deformation along the shear zones through progressively changing deformation mechanisms, and the potential for the migration of hydrothermal fluids along these structures. The study incorporates LiDAR data, field observations and extensive electron backscatter diffraction (EBSD) mapping to describe the structures in detail. The study compares the structures to evidence documented at the surface the contemporary East African Rift, suggesting a mechanism for the migration of CO_2 at depth.

We found that the shear zones were associated with seismic activity, through the documentation of preserved pseudotachylytes. The onset of deformation began with the formation of numerous microfractures within ultramafic host rocks and associated mafic dykes, along the dyke-host rock interface. CO_2-bearing fluids which caused the fractures led to volume expanding reactions within the rocks (olivine + diopside + CO_2 = dolomite + enstatite), further weakening the zones. Plastic deformation in olivine grains formed planar deformation features, sub grain cells, and new fine grains. This, combined with pining, the maintenance of a fine grain size, and the presence of weak mineral phases allowed for sudden failure during transient brittle conditions, leading to seismic activity and the formation of pseudotachylytes. We conclude that lower crustal earthquakes form as the result of local deformation processes, induced by volatiles originating from volatile-rich mafic magmas.

6.2 Fault-linkage on Southeastern Bjørnøya: Implications for structural interpretations surrounding fertile ore-forming fault systems in the offshore domain

This study aimed to describe the structural setting of the hydrothermal mineral system on Bjørnøya, a previously mined Pb – Zn mineralization emplaced along brecciated hydrothermal veins and within massive carbonate bodies, filling a paleo-karst system. Using potential field data, LiDAR lineament analysis, magnetic modelling, 3D photogrammetric models, Win-Tensor V. 5.9.2 (Delvaux, 2012) as well as hand-sample and mineralogical data from thin sections, we aimed to place the formation of structural and mineral system into a broader regional context, relating the structures to events in the Barents Sea region and providing detailed time constraints of the mineralizing events.

The study resulted in several findings, particularly regarding the structural setting surrounding Bjørnøya during the mineralization. Through our detailed mapping of mineralized veins and related-structures, we were able to constrain the mineralizing event to having been emplaced in a transtensional, fault-linkage setting. NW-SE-trending transtensional faults linking larger NS-trending structures played a key role in accommodating deformation and opening fluid pathways along which mineralizing fluids could migrate. The oblique relation to the mostly NE-SW trending veins is as expected for such a setting, in which oblique slip along transtensional faults is observed, particularly through the offset of markers along said faults. As addressed in the *Explored Avenues* chapter of this thesis and within the article itself, our attempts at directly dating the mineralization using Rb/Sr and U/Pb radiogenic isotope systems failed. Despite this, we suggest a Carboniferous to Permian age for the mineralization and transtensional structures, based on comparisons with neighboring domains such as the Fingerdjupet Subbasin. An age as late as Middle Permian is also possible, constrained by the stratigraphy of Bjørnøya itself. The paper concludes that there is a significant potential to uncover more mineralizations in similar structural settings, i.e., transtensional linkage-zones between large-scale normal faults formed during polyphase rifting in the Barents Sea

6.3 Genesis of Pb – Zn mineralizations in the Barents Sea and consequences for offshore ore exploration on continental shelves

The final paper in this thesis considers the genesis of Pb – Zn mineralizations on Bjørnøya and extrapolates this model to the Loppa High, where similar Pb – Zn mineralizations have been found in well cores. Both the Bjørnøya and Loppa High mineralizations occur atop significant structural highs and in conjunction with crustal-scale deformation structures, with relic detachment faults reaching the crystalline basement. There is widespread evidence of hydrothermal activity, including the presence of hydrothermal breccias with Pb – Zn mineralization in both localities, locally exploiting paleo-karst systems. Through a combination of potential field data, seismic lines, detailed sampling, and electron microprobe, fluid inclusion, and isotope analysis we attempt to develop models for the genesis of the mineralizations.

Our study documented both mineralizations and the hydrothermal systems that formed them, while identifying key criteria for the identification of more mineral systems on continental shelves and in particular the Barents Sea. Both the Bjørnøya and Loppa High mineralizations are positioned within significant fault networks, along for fluid migration from the crystalline basement to the overlying sedimentary basins. The presence of specific lithologies, including widespread dolostone and evaporites was key in trapping the minerals. Frequent rifting events across the Barents Sea likely played a critical role in the formation of the hydrothermal systems, which we suggest having formed near the transition from the Carboniferous to Permian. Additional prospective areas may be delineated based on the presence of similar regional tectonic settings and lithologies. Both structures and lithologies are well-documented across the Barents Sea in datasets collected by the petroleum industry, making exploration in this area promising.

7 Infiltration of volatile-rich mafic melt in lower crustal peridotites provokes lower crustal earthquakes

Journal of Structural Geology 163 (2022) 104708

Contents lists available at ScienceDirect

Journal of Structural Geology

journal homepage: www.elsevier.com/locate/jsg

Infiltration of volatile-rich mafic melt in lower crustal peridotites provokes lower crustal earthquakes

Eric J. Ryan *, Bjørn E. Sørensen, Kristian Drivenes, Rune B. Larsen

Department of Geoscience and Petroleum, Norwegian University of Science and Technology, S.P. Andersens veg 15a, 7031, Trondheim, Norway

A B S T R A C T

We document well-preserved extensional shear zones in a rift-related lower-crustal magmatic conduit system, the Reinfjord Ultramafic Complex. Deformation along the shear zones led to seismic events below the seismogenic zone of continental rifts (10–15 kbar and 850–1150 °C), similar to events observed along the East African Rift today. Processes leading to failure of the weakened rocks caused extremely high strain. We mapped pseudotachylytes along a network of millimeter to meter-scale transtensional shear zones associated with gabbronoritic dykes, and a 2 km long low-angle extensional shear zone. Deformation, initiated through priming of the rock by magmatic fluids, exploited subgrains and microfractures in olivine, with CO_2-bearing fluids leading to volume expanding reactions (olivine + diopside + CO_2 = dolomite + enstatite), enhancing olivine fracturing. Fragmentation of the olivine grains and the addition of weaker phases facilitated strain localization and increased the strain rate by two orders of magnitude through grain size reduction (Sørensen et al., 2019). Sudden failure under transient brittle conditions formed pseudotachylytes. We conclude that failure along shear zones in lower crustal continental rifts is possible without remote stress events, in the presence of pre-existing textural and structural heterogeneities and events of volatile fluid infiltration.

1. Introduction

This study provides *in situ* evidence of the structural framework and deformation mechanisms inside the lower crustal segment of a large magmatic conduit system formed during Ediacaran continental rift setting and the terminal disintegration of the Rodinian supercontinent. We investigate the relationship between the migration of C–O–H-rich melts and deformation mechanisms in large-scale ultramafic structural systems in the mantle and lower crust. The uniquely well-preserved field exposures and samples presented in this study were formed at ca. 1 GPa and allow us to investigate the relationship between deformation and volatile-melt emplacement in continental rifts at a rare level of detail. Through this study we demonstrate the influence of volatile-rich fluids on strain localization and deformation in the lower crust.

Most studies of continental rifts near the crust-mantle boundary highlight rift structures and processes using geodynamic modelling (Ziegler, 1992) and/or geophysical investigations (Zwaan and Schreurs, 2020). Physical models of intracontinental rifts account for the large-scale structures observed along rift transects, including structures related to lithospheric thinning and block faulting (Mckenzie, 1978) and transtensional structures in 3D-space (Brune et al. (2018) and references therein). However, due to the extreme exhumation required to expose the lower crust, few field studies of the deep sections of rifts exist as original geological features are obliterated by deformation and metamorphism.

Researchers have long recognized the presence of mantle-derived C–O–H fluids in rifts (Irwin and Barnes, 1980). Fluid migration along crustal-scale structures brings mantle-derived fluids up to the Earth's surface (Pili et al., 1999), as documented through surface CO_2-outgassing (Lee et al., 2016). The upwards migration of deeply derived fluids is highly dependent on the interaction of rock, magma, and fluids during deformation in the lower crust. C–O–H fluids also play an important role in the formation of mid to upper crustal resources, as deep fluid signatures are found in hydrocarbon reservoirs (Finlay et al., 2010; Fetter et al., 2019) and in Mississippi valley type (MVT) and sedimentary exhalative (SEDEX) ore deposits (Blundell et al., 2003; Schmidt Mumm and Wolfgramm, 2004). Other authors have documented a link between magmatism, fluids, and seismicity at depth of 30–40 km (Lee et al., 2016; Roecker et al., 2017; Weinstein et al., 2017), indicating a link between fluids and seismic activity in continental rift settings. Recently, La Rosa et al. (2021) suggested a link between magmatic or other CO_2-rich fluids and fluid-induced lower crustal earthquakes in the Afar rift.

C–O–H fluids may help drive deformation along migration pathways (Sørensen et al., 2019), but relatively little is known about the effects of such fluids in the mantle and lower crust. CO_2 both embrittles olivine

* Corresponding author.
E-mail addresses: Eric.j.ryan@ntnu.no (E.J. Ryan), bjorn.sorensen@ntnu.no (B.E. Sørensen), kristian.drivenes@gmail.com (K. Drivenes), rune.larsen@ntnu.no (R.B. Larsen).

https://doi.org/10.1016/j.jsg.2022.104708
Received 8 September 2021; Received in revised form 28 July 2022; Accepted 19 August 2022
Available online 30 August 2022

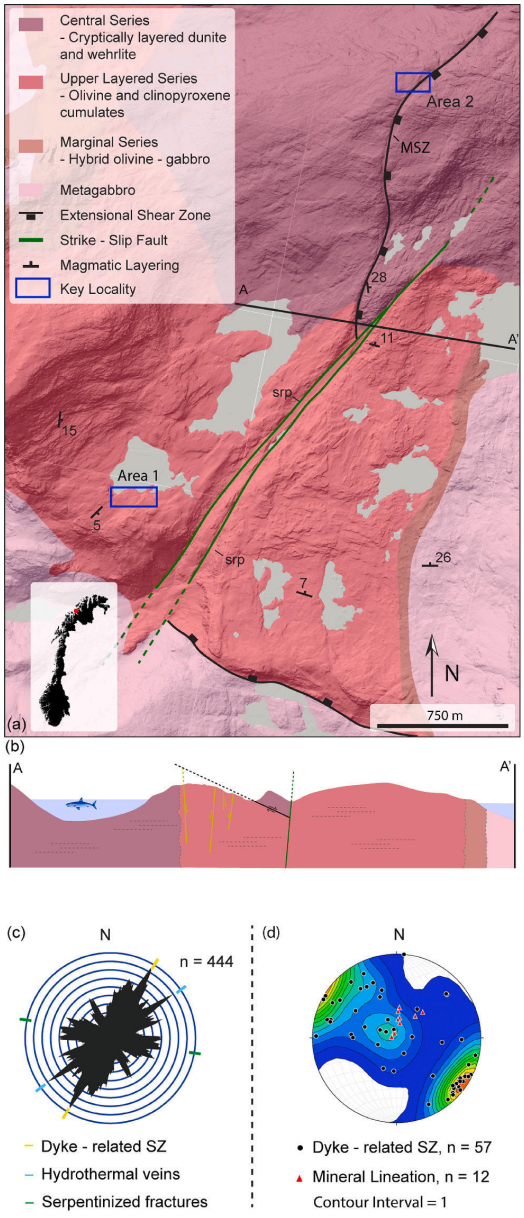

Fig. 1. (a) A map of the central Reinfjord Ultramafic Complex. The main normal shear zone, large serpentinized (srp) strike-slip faults, and key outcrops, Area 1 and Area 2 are shown. (b) A sketch profile across the main shear zone and strike-slip fault in the RUC. Common orientations of the mostly sub-map scale dyke-related shear zones are extrapolated to the profile. (c) A lineament analysis was performed on LiDAR data, visible here as the hillshade background in (a). (d) The orientations of the dyke-related shear zones are shown in the stereonet by contours and black poles to the shear planes. Infrequent mineral lineations along the shear planes are shown as red triangles. The dyke-related shear zones are sub map scale but are thoroughly described in the text. (For interpretation of the references to color in this figure legend, the reader is referred to the Web version of this article.)

(Rovetta et al., 1986) and reacts with ultramafic rocks, forming carbonates (Wyllie et al., 1983) and causing volume expanding mineral reactions (Sørensen et al., 2019). These reactions weaken rocks, leading to strain localization, increased strain rates and/or stress release through brittle failure and earthquakes (Campbell et al., 2020). Lower crustal seismicity occurs at similar depths to those where alkaline magma exsolves CO_2 (Pan et al., 1991; Gerlach et al., 2002). These coinciding depths could indicate a link between magmatic CO_2-bearing fluids and some deformation at certain crustal levels (Wilshire and Kirby, 1989).

A large body of research is dedicated to understanding deformation mechanisms in the mantle and lower crust, particularly in peridotite rocks. The samples collected during this study exhibit a spectacular interplay between ductile and brittle deformation in ultramafic and mafic mineral assemblages. Olivine type fabrics pertaining to specific geodynamic and environments were described by Ismail and Mainprice (1998). Individual type fabrics can also be related to the activation of specific slip systems in olivine (Zhang and Karato, 1995), revealing deformation mechanisms at the smallest scales. More recent experimental work investigates strain localization and grain boundary sliding in olivine (Hansen et al., 2011, 2012), the findings of which we attempt to extrapolate to our own natural samples where intense strain localization occurred. Finally, studies investigating deformation during transient differential stress (Druiventak et al., 2012; Matysiak and Trepmann, 2012, 2015) shed light on the varying deformation mechanisms activated in olivine during lower crustal earthquake cycles and are compared to the findings of this study.

Our observations include mutually overprinting olivine ultramylonites and pseudotachylytes, all formed in the lower crust. Pseudotachylytes, more commonly associated with shallow crustal levels, form as a melt product of frictional heating (Mckenzie and Brune, 1972). Numerous studies document brittle deformation and pseudotachylytes in the lower crust (Hawemann et al. (2018) and references therein). Mutual overprinting relationships between pseudotachylytes and ultramylonites indicate that these structures may form at similar boundary conditions (Sibson, 1980; Papa et al., 2020). Unfortunately, pseudotachylytes formed in the lower crust are prone to recrystallization, alteration, and crystal plastic deformation, making their certain identification difficult (Kirkpatrick and Rowe, 2013). However, numerous observations including vein geometry, the presence of anomalously high-temperature phases, dispersed sulfide droplets, flow textures and the presence of preserved clasts may be used to identify relic pseudotachylytes (Kirkpatrick and Rowe, 2013). Despite a large body of work documenting both ultramylonites and pseudotachylytes in the lower crust, the mechanisms driving deformation at depth remain enigmatic.

Many potential driving mechanisms behind lower crustal and mantle deformation have been proposed, including self-localizing thermal runaway (Braeck and Podladchikov, 2007; John et al., 2009), fluid and reaction-induced weakening (Sørensen et al., 2019), and the downward propagation of rupturing faults (Petley-Ragan et al., 2019). Fluid and reaction-induced weakening has already been documented in the Reinfjord ultramafic Complex (Sørensen et al., 2019), while other works invoke the downward propagation of rupturing faults to explain similar mutually overprinting brittle and ductile features (Jamtveit et al., 2018; Petley-Ragan et al., 2019; Papa et al., 2020). Other studies conclude that shear zones form along preexisting heterogeneities, like dykes, in ultramafic rocks (Toy et al., 2010). In this paper, we combine field, micro and macrostructural studies with geothermobarometry and document the interplay between dykes, fluids, and deformation in the lower crust, revealing the driving forces behind deep deformation and strain localization in this continental rift system.

2. Geological background

This study was conducted within the Reinfjord Ultramafic Complex (RUC) (Fig. 1), part of the Seiland Igneous Province (SIP) in Northern

Norway. The SIP constitutes one part of the Central Iapetus Magmatic Province (CIMP) (Ernst and Youbi, 2017; Pu et al., 2016; Youbi et al., 2020; Gumsley et al., 2020). The CIMP consists of the fragments of a single large igneous province (LIP), now spread across Scandinavia, North America, and Southwestern Greenland (Ernst and Bell, 2010; Tappe et al., 2017), formed during terminal breakup of the Rodinian super continent from 610 to 550 Ma (Kamo et al., 1989; Bingen and Demaiffe, 1998; Cawood et al., 2001; Ernst and Buchan, 2004). As the Iapetus Ocean opened, magma and volatile fluids flooded the rift zones across the modern North Atlantic (Ernst and Bleeker, 2010). The SIP provides excellent exposure of deep, rift-related structures and processes in a high-yielding magmatic conduit system (Grant et al., 2016, 2020; Larsen et al., 2018; Sørensen et al., 2019). Like the larger CIMP, the SIP and RUC are associated with continental rifting, based on rock associations (Krill and Zwaan, 1987; Roberts et al., 2006), extensional tectonics (Andréasson et al., 1998), geochemical analysis (Reginiussen et al., 1995) and geochronological association (Roberts, 2007; Roberts et al., 2010). Having formed at a minimum of 30 km depth, the SIP offers a unique window to tectonic and magmatic rifting processes in the lower crust (Larsen et al., 2018).

During LIP magmatism, volatile fluids are channeled from the mantle to the upper crust (e.g. Ernst et al., 2019) along magmatic pathways. Pastore et al. (2016) used 3D gravity modelling to suggest that the SIP is 2–4 km thick with deep roots extending 6–9 km's downwards. These roots are interpreted as magmatic conduits that transported more than 100,000 km^3 of volatile-rich basic, ultrabasic and alkaline melts (Grant et al., 2016; Larsen et al., 2018). During rifting, the roots also acted as migration pathways for CO_2-rich volatile fluids and melts rich in ore-forming sulfur, volatiles and economic elements (Larsen et al., 2018). The presence of sulfide and platinum group minerals together with carbonates and hydrous minerals demonstrates the importance of volatile-rich melts for the formation and distribution of sulfide mineralizations within the SIP and RUC (Larsen et al., 2018).

The RUC is hosted by the Langstrand Gabbronorite, a subalkaline sub-horizontally layered intrusion. Steeply dipping contacts separate the gabbronorite from the RUC peridotites, creating a cylinder of ultramafic rocks within the gabbronorite (Bennett, 1974; Bennett et al., 1986). A series of three major intrusive phases created the RUC, including the lower layered series, upper layered series, and central series, all superimposed by multiple smaller recharge events (Grant et al., 2016). Each series comprises modally layered, cyclic olivine and pyroxene cumulates, of dunitic, wehrlitic and pyroxenitic compositions (Emblin, 1985; Bennett et al., 1986). The central series partially replaced the upper layered series in the RUC, forming a complex intrusive relationship (Grant et al., 2016). Basic, ultrabasic and alkaline dykes intruded the dunitic rocks of the central series through pervasive emplacement mechanisms. As the dyke infiltration localized, pyroxenitic dikes intruded via ductile fracture and eventually brittle-elastic mechanisms (Orvik, 2019). At the same time, wehrlite-gabbronorite dyke swarms and amphibole-bearing carbonate assemblages formed throughout the RUC (Larsen et al., 2018). Later dyke-parallel shear zones reworked some of the dykes, causing intense strain localization along the dyke contacts (Sørensen et al., 2019).

Numerous authors have documented pre-, syn- and post-magmatic deformation in the SIP and RUC related to continental rifting (Degli Alessandrini et al., 2017; Lee et al., 2020; Sørensen et al., 2019). Volatiles played an important role in the post-magmatic deformation of ultramafic rocks. Volume expansion caused by the reaction between olivine, clinopyroxene and C–O–H fluids, formed dolomite and orthopyroxene along olivine grain boundaries and led to micro-fracturing in large olivine grains (Sørensen et al., 2019). The reaction caused a grain size reduction and a two order of magnitude decrease in rock strength (Sørensen et al., 2019). The grain size reduction increased porosity and permeability, opening the door for fluid migration and metamorphic reactions. The fluid influx and following alteration led to strain localization and an increase in strain rate along the shear zones (Sørensen et al., 2019).

Despite involvement in the Scandian (420 Ma) phase of the Caledonian Orogeny, the shear zones in the central series and greater SIP preserve pre-Caledonian deformation events (Pastore et al., 2016; Larsen et al., 2018). The Kalakk Nappe, to which the SIP belongs, shows multiple phases of widespread amphibolite facies metamorphism. The exact metamorphic history is difficult to decipher, however during the Caledonian Orogeny some metasediments in the SIP locally experienced high-grade metamorphism, at 550–660 °C at 10–12 kb around 430–440 Ma (Gasser et al., 2015). Despite this, the rocks of the RUC are left relatively unaffected by Caledonian events and escaped later tectonic or metamorphic overprint (Larsen et al., 2018), apart from minor serpentinization at lower greenschist facies conditions.

3. Methods

Supplementary to our detailed field study, we used microanalysis techniques including optical microscopy, scanning electron microscopy (SEM), electron microprobe analysis (EPMA), electron backscatter diffraction (EBSD), and X-ray diffraction (XRD) measurements to constrain the mineralogy and deformation mechanisms in our study area. All analyses were carried out in the Norwegian Laboratory for Mineral and Materials Characterization (MiMaC) lab at the Department of Geoscience and Petroleum, Norwegian University of Science and Technology.

3.1. Electron backscatter diffraction

Thin sections of selected samples were chemically polished using OP-U, a 400 Å suspended colloidal silica polishing agent, before being rinsed in 96% alcohol, following the procedure outlined in Moen et al., (2003). We conducted the Electron Backscatter Diffraction (EBSD) analyses on a Hitachi SU-6600 SEM, in variable pressure low vacuum mode at 10–15 Pa, using 20 kV accelerating voltage and 1.70 kV extraction voltage. The samples were mounted on metal pedestals at standard eucentric height with a tilt angle of 70° and working distance of 22.0 mm. EBSD patterns were acquired using a NORDIF UF-1000 detector and NORDIF 3.0 software at 240 × 240-pixel resolution. The samples were analyzed with a step size of 0.5–2 μm, depending on grain size and the size of the area. The frame rate and exposure time were adjusted for each sample to accommodate for different mineral assemblages. We selected numerous acquisition and calibration patterns throughout the scanned areas, using the NORDIF interface and electron backscatter image, ensuring that the pattern center remained calibrated across the large area scans. The orientations of the shear zone boundaries near the sample locations were used as a reference system for the orientation and kinematic interpretation of the samples. To avoid geometric trapezoidal scan distortions in the maps, a beam scan voltage correction was implemented using a EM-Tec LAMC-15 Large area magnification calibration standard (Sørensen et al., 2020). Indexing was done using TSL-OIM 7.2 software. EBSD data cleanup was done according to the procedures described in Sørensen et al. (2020), checking the consistency of indexing and cleanup procedures. EBSD plotting was done using MTEX (Bachmann et al., 2010) version 5.7. Pole figures were calculated using a de la Vallée Poussin kernel with a half width of 10°, making results comparable between datasets. We used one-point-per-grain to plot the orientation data, as our samples have a highly heterogenous grain size distribution and we aimed to avoid oversampling of large grains following Park and Jung (2020). EBSD KAM maps were constructed from smoothed data using the algorithm for half quadratic filter in MTEX (Hielscher et al., 2019).

3.2. Electron microprobe analysis

We analyzed points in olivine, pyroxene, amphibole, feldspar, and carbonate grains using the JEOL JXA-8530F Plus Hyperprobe, the results of which we used for empirical geothermobarometry and

thermodynamic modelling, as well as mineral identification. The acceleration voltage and beam current were set to 15 kV and 10 nA, respectively, and the defocused beam diameter varied between 1 (pyroxene, olivine, and garnet) and 3 (feldspar, amphibole, and carbonates) μm. Peak and background counting times varied between 5″ and 2″ for Na, 50″ and 25″ for F, and 20″ and 10" for the remainder of elements. For more accurate matrix corrections, we added a fixed water content of 2 mass percent to the amphibole analyses, and 44.07 mass percent CO_2 to the carbonate analyses. Typical detection limits (3σ) varied from 180 (Ca) to 900 μg/g (F). Mineral and pure metal standards from Astimex and Micro-Analysis Consultants were used as reference materials and to monitor samples during the analyses. We analyzed a total of 41 olivine, 102 pyroxene, 55 amphibole, 110 feldspar and 4 carbonate points and applied the data to empirical geothermobarometers to unravel the pressure and temperature conditions during deformation in the Reinfjord Ultramafic Complex. Average representative values of the data are provided in Table 2.

3.3. Geothermobarometry

We used a combination of thermodynamic modelling and empirical methods to constrain the pressure and temperature conditions during deformation in the RUC. We created our pseudosection for the peridotite mineral assemblage using Perple_X v. 6.9.1 (Connolly, 1990). and the Holland and Powell (2011) thermodynamic database, with the carbonate solution model from Franzolin et al. (2011), orthopyroxene (Opx (HP)) and clinopyroxene (Cpx(HP)) solution models from Holland and Powell (1996), and olivine solution model (O(HP)) from Holland and Powell (1998). We used the same bulk assemblage as Sørensen et al. (2019), namely SiO_2: 4.43, Al_2O_3: 0.0235, FeO: 1.27, MgO: 6.02, CaO: 0.525 and CO_2 0.980, derived from a linear interpolation of the mineral compositions obtained using EPMA and the amounts of each phase from a syn-tectonic assemblage in a dyke-related shear zone (Sørensen et al., 2019). We were unable to model some complex assemblages using Perple_X. For these assemblages we used equations from the amphibole – amphibole geothermobarometers of Ridolfi et al. (2010) and Ridolfi and Renzulli (2012), and the amphibole - plagioclase geobarometer from Molina et al. (2015). The applicability of each model to our mineral compositions is evaluated in the discussion.

4. Results

4.1. Structural framework

A network of shear zones cuts the Reinfjord Ultramafic Complex (RUC) (Fig. 1a). The most prominent is a large extensional to transtensional shear zone dipping approximately 31° towards 101° (Fig. 1a), referred to as the main shear zone. The main shear zone is oblique to the remainder of the shear zones, which are subvertical and trend to the NNE - SSW. Most of these second order shear zones formed in the footwall of the main shear zone, along hornblende gabbronorite dykes in the peridotite host rocks, as shown in the profile in Fig. 1b. We refer to these shear zones as dyke-related shear zones in the remainder of the text. A digital elevation model (DEM) from the field area shows a high frequency of lineaments (Fig. 1a). We selected and analyzed the orientation of the lineaments from the DEM in a rose diagram (Fig. 1c). Out of the 444 selected lineaments, the orientations correlated to dyke-related shear zones through direct observation during extensive field work form the most prominent peak (Fig. 1c), dominating the structural fabric of the field area. Smaller peaks are attributed to hydrothermal veins and serpentinized fractures (Fig. 1c), neither of which are the focus of this study. The subvertical, NNE-SSW trending shear zones range between less than 1 cm to over 1 m in width and can be followed for up to 250 m along strike. Mineral lineations plunging between 60° and 80° towards the N – NE indicate oblique extensional slip (Fig. 1d). Two main areas were selected for detailed investigations. Area 1 is the type locality of the dyke-related shear zones, while Area 2 is the type locality for the main shear zone. Table 1 provides an overview of key samples from each of the areas.

Table 1
Sample Overview from Area 1, the dyke-related shear zones, and Area 2, the main shear zone. Supplementary microphotographs, taken from similar representative samples, are noted in the Figures column.

	Area	Sample	Lithology	Figures
Dyke-related Shear Zones	Area 1	A1-1	Deformed peridotite with lenses of hornblende gabbronorite dyke. Two sections: A1-1a normal to lineation and foliation; A1-1b parallel to lineation and normal to foliation	Figs. 2–3 – Figs. 4–5
	Area 1	A1-2	Deformed hornblende gabbronorite dyke	Figs. 6–7 – Fig. 8
	Area 1	A1-2	Deformed hornblende gabbronorite	Figs. 6–7 - Fig. 9
Main Shear Zone	Area 2	A2-1	Deformed dunite	Figs. 10–11a
	Area 2	A2-2	Deformed dunite and pyroxenite dyke	Figs. 10–11b
	Area 2	A2-3	Ultramafic - mafic ultramylonite	Figs. 10–11c, e, f - Fig. 12

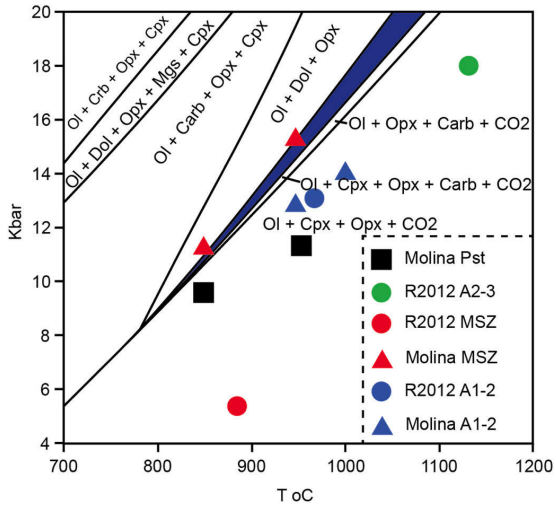

Fig. 2. PT-estimates for the shear assemblages. The pseudosection is modified after Sørensen et al. (2019), using the same bulk assemblage which we confirmed was relevant for our samples through extensive EPMA analyses. Our own empirical estimates are shown using the colored symbols. R2012 refers to empirical analyses performed following the methods outlined in Ridolfi and Renzulli (2012) while *Molina* refers to those performed following Molina et al. (2015). The empirical estimates span a wide range of PT conditions, but cluster between 11 and 15 kbar and 900°–1000 °C for the ultramylonites and 850° and 950 °C and 9.5 and 10.5 kbar for the pseudotachylytes. Pst = pseudotachylyte, MSZ = main shear zone, A1-2/A2-3 = sample names.

4.2. PT – estimates of the Reinfjord Ultramafic Complex

Thermodynamic modelling of a deformed peridotite mineral assemblages from the shear zones indicates high-grade deformation conditions. Following the analysis performed by Sørensen et al. (2019), we

Table 2
Average representative EPMA analyses for phases in the main shear zone (MSZ), dyke-related shear zones (DSZ) and pseudotachylyte.

	Avg. Representative values														
	(n) - number of points analyzed														
	Ultramylonite	**MgO**	**Na2O**	**Al2O3**	**CaO**	**K2O**	**Cr2O3**	**FeO**	**MnO**	**NiO**	**TiO2**	**SiO2**	**Total**		
MSZ	Olivine (41)	42.825		0.314	0.136		0.080	16.576	0.232	0.212	0.052	39.081	**99.028**		
	Orthopyroxene (18)	31.418		0.564	0.164		0.077	11.105	0.279	0.068	0.061	55.527	**99.094**		
	Clinopyroxene (4)	16.795	0.517	1.181	23.015		0.170	3.355	0.113		0.144	53.420	**98.710**		
		MgO	**Al2O3**	**Na2O**	**F**	**SiO2**	**CaO**	**K2O**	**Cr2O3**	**FeO**	**NiO**	**MnO**	**Cl**	**TiO2**	**Total**
	Amphibole (8)	16.441	13.288	3.281	0.223	42.077	11.556	0.664	0.572	6.371	0.070	0.078	0.096	1.773	**96.465**
		MgO	**Na2O**	**Al2O3**	**CaO**	**K2O**	**Cr2O3**	**FeO**	**MnO**	**NiO**	**TiO2**	**SiO2**	**Total**		
	Dolomite (4)	21.633			28.323			3.210	0.182				**55.307**		
		MgO	**Na2O**	**Al2O3**	**CaO**	**K2O**	**Cr2O3**	**FeO**	**MnO**	**NiO**	**TiO2**	**SiO2**	**Total**		
DSZ	Orthopyroxene (41)	22.862	0.090	1.916	0.590	0.087		21.398	0.517	0.078	0.153	52.284	**99.790**		
	Clinopyroxene (32)	13.883	0.993	2.665	22.202	0.080	0.088	6.960	0.197		0.356	52.681	**99.954**		
		MgO	**Al2O3**	**Na2O**	**F**	**SiO2**	**CaO**	**K2O**	**Cr2O3**	**FeO**	**NiO**	**MnO**	**Cl**	**TiO2**	**Total**
	Amphibole (42)	11.320	13.932	2.417	0.103	41.170	11.508	1.499	0.098	12.108	0.088	0.116	0.063	3.109	**97.350**
	Plagioclase (105)	**Na2O**	**Al2O3**	**MgO**	**CaO**	**TiO2**	**SrO**	**BaO**	**FeO**	**K2O**	**SiO2**	**MnO**	**Total**		
		6.579	26.680	0.033	8.791	0.069	0.203		0.118	0.169	57.429		**99.965**		
	Pseudotachylyte														
		Na2O	**Al2O3**	**CaO**	**K2O**	**SiO2**	**Total**								
	Plagioclase (5)	6.16	26.53	9.10	0.22	57.27	**100.18**								
		Na2O	**MgO**	**Al2O3**	**CaO**	**K2O**	**Cr2O3**	**FeO**	**SiO2**	**TiO2**	**Total**				
	Amphibole (5)	1.64	10.65	14.74	11.64	2.14	0.21	13.38	39.95	2.76	**99.18**				
		Na2O	**MgO**	**Al2O3**	**CaO**	**FeO**	**TiO2**	**SiO2**	**TOTAL**						
	Pyroxene (7)	1.04	13.46	4.25	21.40	7.44	0.37	51.41	**99.69**						

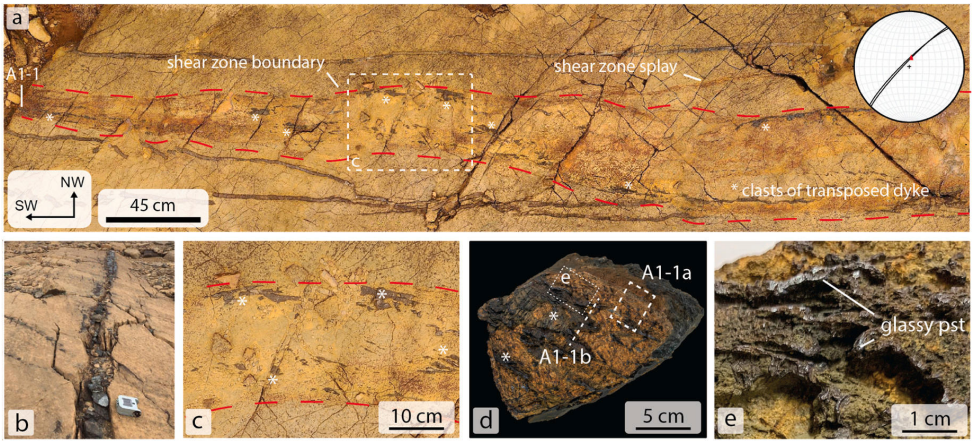

Fig. 3. Aerial image and outcrop photographs of sample A1-1 (a) Aerial image of a completely transposed dyke along a dyke-related shear zone. The sampling location of A1-1 is denoted. Only spaced, dark clasts of the dyke are visible in the high-strain shear zone and are labeled with asterisks, while the boundary of the high-strain region is denoted by a red dashed line. The stereonet shows the orientation of the dyke and corresponding mineral lineations (b) Another example of a dyke-related shear zone, for reference. The dyke is well-preserved in this zone, though the dyke-host rock interfaces have still accommodated significant strain. More dyke-related shear zones are documented in Fig. 8. (c) A close-up of the clasts of transposed dyke, preserved within the shear zone core. The shear zone is visible in the field as a slight color change within the peridotite host rock and is denoted by the dashed red lines. (d) The A1-1 sample. The position of A1-1a and A1-1b are shown as on the sample. (e) Dark glassy bands, shown here reflecting light from a camera flash, indicate the presence of pseudotachylyte (pst) in the sample. (For interpretation of the references to color in this figure legend, the reader is referred to the Web version of this article.)

created a pseudosection (Fig. 2) for the forsterite, enstatite, diopside, dolomite assemblage using the same bulk assemblage from a syntectonic assemblage in a dyke-related shear zone (in molar amounts) SiO2 - 4.43 Al2O3: 0.0235, FeO: 1.278, MgO: 6.02, CaO: 0.525, and CO2: 0.980. This assemblage is stable over a wide range of PT-conditions, ranging from below 800 °C and 8 kbar to above 1100 °C and 20 kbar, providing a minimum PT constraint during deformation. The coeval host rock and dyke deformation allow us to estimate PT-conditions using two unrelated mineral assemblages within individual shear zones.

The Ridolfi et al. (2010), the updated Ridolfi and Renzulli (2012) and the Molina et al. (2015) models produce variable results (Fig. 2) with pressures between 5.7 and 17.9 kbar and temperatures between 880° and 1130 °C. If we base our pressure estimate solely on Molina et al. (2015), with the most representative calibration, we estimate pressures between 11.5 and 15.5 kbar and temperatures between 860 °C and 950 °C in the ductile shear zones. We also analyzed recrystallized pseudotachylytes *section 4.6 Evidence of pseudotachylytes*) using the same models, which indicate pressures between 9 and 12 kbar at temperatures between 850° and 950 °C (Fig. 2). Notably the temperatures in the pseudotachylyte veins exceed the values of the Olivine + Diopside carbonation reaction i.e., Ol + Di + CO2 = En + Dol. The bulk assemblages for the pseudosection and the mineral compositions for the empirical models were based on our EPMA data, a summary of which is shown in Table 2.

4.3. Area 1 – dyke-related shear zones

4.3.1. High-strain dyke-related shear zone

Fig. 3 documents a high-strain example of a dyke-related shear zone, along which the dyke material is completely transposed and incorporated into the structure, to the point where the dyke becomes difficult to identify without close inspection. The shear zone extends for 75 m along strike and varies between 15 and 100 cm in width. The zone dips steeply (85°) towards the northwest (320°), with a pyroxene mineral lineation plunging steeply (75–80°) to the northeast (058°), indicating a slightly oblique normal shear direction. In the field, such high-strain shear zones are marked by a change in color of the rocks with a more orange to yellow tint on weathered surfaces, a black, glassy appearance on fresh surfaces, and the presence of deformed dykes. The dyke along this shear zone is completely transposed, with only spaced clasts of dyke remaining distributed throughout the shear zone core (Fig. 3a and c). Other dykes are less deformed and more easily identifiable in the field, such as the dyke shown in Fig. 3b. The more well-preserved dykes are discussed in 4.3.2. The location of sample A1-1 is shown in Fig. 3a and the sample in Fig. 3d. The dark bands with a glassy appearance (Fig. 3e) are remnants of the transposed hornblende-gabbronorite dyke, which formed pseudotachylytes during deformation. The sample was cut into two perpendicular thin sections (Figs. 3d and 4a). XRD analysis of the deformed host rock, visible in Fig. 4a and b gives the following composition Fo – 78%, En – 8%, Hbl – 6%, Di – 5%, Ant – 3%. The antigorite is constrained to small veinlets, while the trace amounts of dolomite were too low to detect using XRD (<1 wt%).

Despite the high-strain nature of the zone we observe a wide range in accumulated strain, with some olivine grains preserving earlier deformation textures (Fig. 4). Fig. 4a shows both thin sections from the high-strain sample (A1-1). A sharp transition separates the preserved peridotite from the high-strain shear assemblage (Fig. 4a and b). The composition of the shear zones near the host rock contains alternating domains of dyke and peridotite material (Fig. 4a), apparently due to irregular dyke boundaries along the shear zones. Dark bands of ultra-fine-grained material cut the dunitic ultramylonite. The ultra-fine-grained material extends locally from domains of more coarse-grained (≈100 μm EQR) hornblende gabbronorite, but also appear as isolated pockets of dark material in thin sections and cuts discordantly across the shear zone foliation (Fig. 4a and b). Planar deformation features are preserved inside the higher strain zones, where the planes become thick bands of new grains eventually replacing the entire parent grain with peridotite ultramylonite (Fig. 4c). The preserved olivine grains contain minute sets of planar deformation features decorated by new grains (equivalent radius (EQR) = 4–5 μm) (Fig. 4d). EDS and EPMA analyses indicate that these grains are ultra-fine-grained dolomite along microfractures in the olivine. Other dykes exhibit more evidence of fluid infiltration leading to deformation within the host rock, exemplified by the small shear zone extending from a dyke tip into the peridotite host

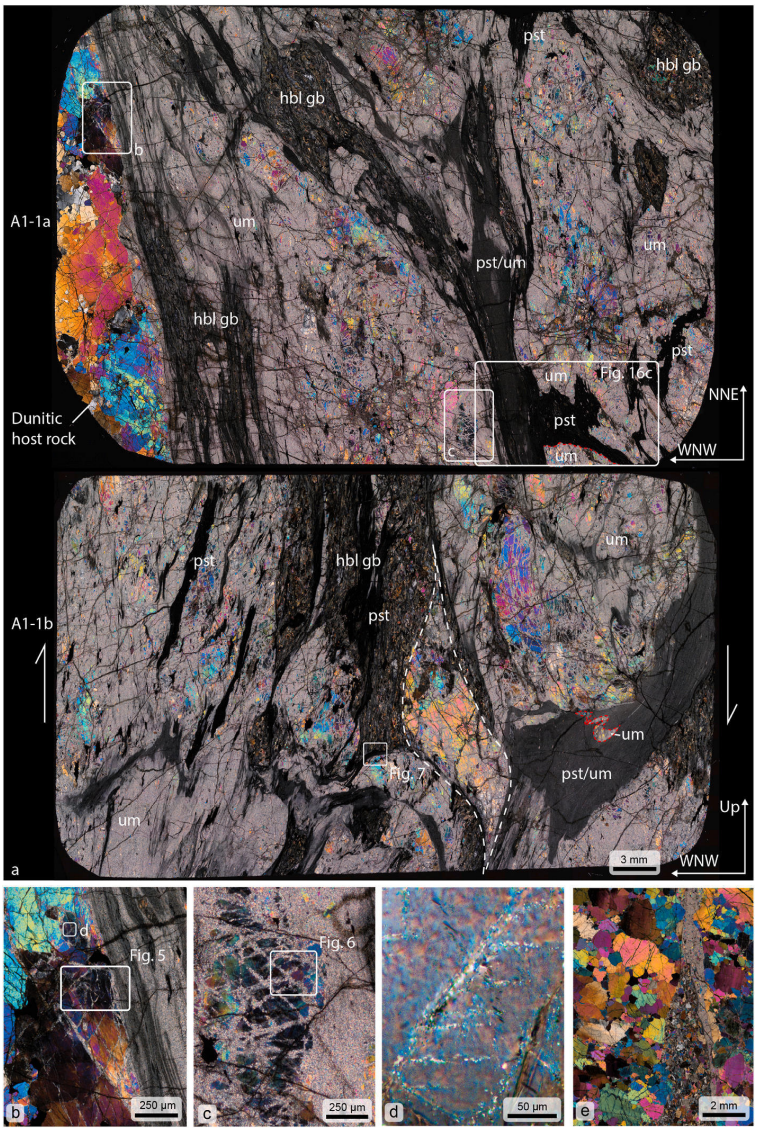

Fig. 4. Thin sections scans and microphotographs from sample A1-1. (a) A1-1a (upper) and A1-1b (lower) thin sections, oriented normal to and along the transport direction of a dyke-related shear zone. The white boxes show the location of EBSD analyses and corresponding microphotographs. The orientation of the thin sections is denoted adjacent on each scan. Arrows indicate the transport direction within the lower scan. Numerous fragments of well-preserved pseudotachylyte veins are visible within the ultramylonite. We also observe pseudotachylytes which cut obliquely across the ultramylonitic foliation (upper image) and deformed, folded clasts of ultramylonite within zones of recrystallized pseudotachylyte (lower image), each denoted by red dashed lines. Hbl gb = hornblende gabbronorite, pst = pseudotachylyte, um = ultramylonite, pst/um = recrystallized/mylonitized pseudotachylyte (b) and (c) Low-strain olivine along and in the shear zone showing distinct planar deformation features. The location of the EBSD maps in Fig. 5 and 6 are shown (d) Small bright grains of trace carbonates following olivine microfractures. (e) More evidence of fluid infiltration from the dyke to the host rock, with a small shear zone full of hydrous amphibole and carbonate extending from the tip of a dyke into the peridotite. (For interpretation of the references to color in this figure legend, the reader is referred to the Web version of this article.)

rock in Fig. 4e.

Three areas of the high-strain sample were mapped using EBSD, denoted by white boxes in Fig. 4a, b and c, revealing various microfabrics along the shear zone (Figs. 5–7). Fig. 5 shows the boundary of the shear zone and the interface between the peridotite and dyke assemblages. We divided the data set into 6 regions, predominantly containing olivine, with hornblende and pyroxene in regions 3 and 5 (Fig. 5a). The kernel average misorientations (KAM) are shown for the partly recrystallized parent olivine grains. Numerous planar deformation features follow the traces of crystallographic planes. The features occur primarily along the {1 2 0}, {1 3 0} and {0 1 0} planes and contain 15 μm wide bands of new olivine grains and secondary phases enstatite, and minor dolomite and pentlandite (Fig. 5a). Secondary features following other crystallographic directions are also visible in the KAM map, though without significant recrystallization (Fig. 5a). The angular and undulatory boundary between the partly recrystallized parent grains and the fine-grained shear zone is consistent with the observed fracture directions of the parent grain (Fig. 5a), which follow the crystallographic axes shown in Fig. 5d. We observe a progressive weakening and a rotation of the olivine CPO moving from the low to high-strain domains, reflecting a distortion of the parent grain orientation (Fig. 5b) and possibly a change in deformation mechanism. The olivine CPOs in regions 1 and 2 are like the orientation of the large parent grain, though the CPO weakens in region 2 approaching the high-strain domain. Regions 3 and 4 contain very weak a-axis girdles with a weak point maximum in the lineation direction in region 4 and b-axis point maxima near the sample foliation pole (WNW), while the c-axis maxima are random. Region 5 contains minor olivine and shows weak to random

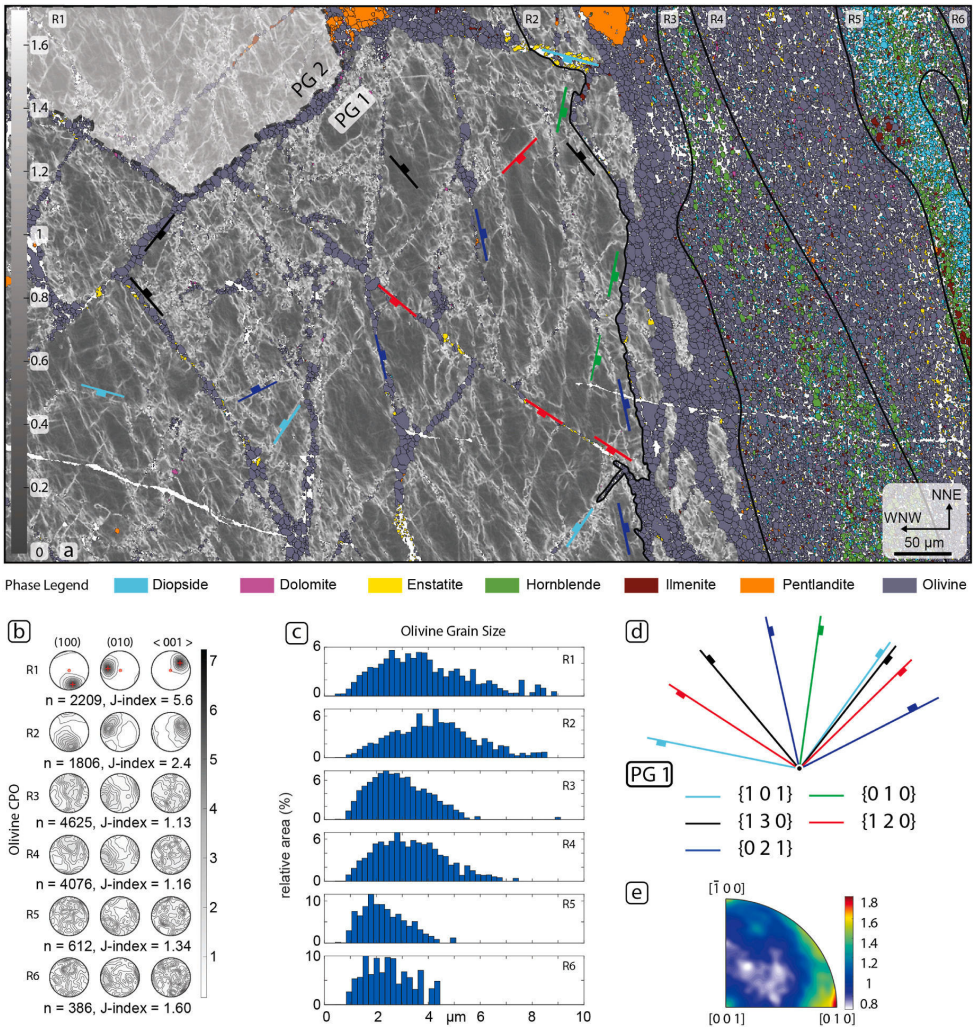

Fig. 5. EBSD data from sample A1-1a. (a) Combined phase and kernel average misorientation (KAM) map. The KAM data are for parent olivine grains, while the recrystallized olivine is denoted in lilac. Two parent olivine grains are present in the sample, PG 1 and PG 2, our analyses focus on the largest parent grain (PG1). (b) Pole figures showing the orientation of the (100), (010) and <001> planes for olivine in each region. Red crosses denote the parent grain orientation in region 2. Red circles in pole figures for region 1 denote the orientation of the stretching lineation. "n" denotes the number of grains. (c) The EQR grain size of olivine within each region, shown in area %. (d) Orientation of the plane trace of crystallographic planes for parent grain 1 (PG1). (e) The misorientation axes of all olivine grains. (For interpretation of the references to color in this figure legend, the reader is referred to the Web version of this article.)

CPO, whereas region 6 shows similar CPO to regions 3 and 4 but includes significantly fewer grains over a smaller area. We observe a progressive grain size reduction moving from the low-strain (region 1) to high-strain domains (Fig. 5c). Average grain sizes range from 3.5 μm EQR in region 1, excluding the large parent grains, and 2 μm EQR in region 6. The misorientation axes for all the olivine grains concentrate around the [0 1 0] direction (Fig. 5e).

Fig. 6 shows a deformed and fractured parent olivine grain within the high-strain domain of the shear zone (Fig. 4c). A combined phase and KAM map is shown in Fig. 6a. The map shows enstatite and dolomite, as well as pentlandite or ilmenite along the planar deformation features. In the center of the map, minute amounts of diopside are also present. The planar deformation features following the crystallographic planes are more developed than those documented along the edge of the shear zone. The larger recrystallized features follow the {001}, {120}, and {010} planes in the KAM map. Sections of the relic grains show a distinct planar subgrain structure, whereas other areas tend towards a more cellular subgrain structure. The new grains are a mix of fragments from the parent grains, subgrains and grains generated through subgrain rotation (small grains within the parent grains), and equant recrystallized olivine with distinct triple junctions, possibly related to late recovery. The misorientation of the recrystallized olivine grains (Fig. 6b) is loosely concentrated around 60° to the parent grains. In both maps, the recrystallized olivine grains show a relatively uniform grain size distribution, with equant grains and frequent triple junctions. Twist and tilt boundaries crosscut the parent grain and are as expected generally parallel to the crystallographic planes (Fig. 6b).

The third EBSD map from a dyke-related shear zone (Fig. 7)

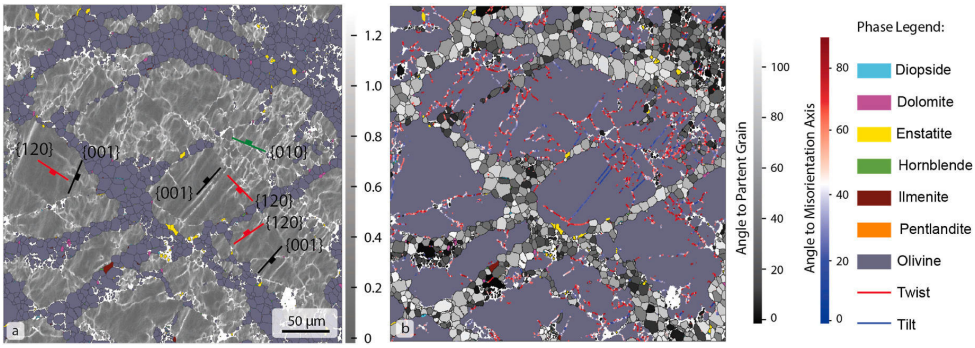

Fig. 6. EBSD data from the fractured parent grain relic in the inside the shear zone displayed in Fig. 4c. (a) Combined phase and KAM map, with the orientation of specific crystallographic planes related to planar deformation features denoted with colored symbols. The KAM map covers the parent olivine grains. (b) Map of the same area showing the misorientation angle of the new olivine grains to the parent grain. The angle of misorientation axes to the boundary trace is also shown, with the kink boundaries in blue and the twist boundaries in red. (For interpretation of the references to color in this figure legend, the reader is referred to the Web version of this article.)

documents an ultra-fine-grained assemblage with distinct compositional zoning from the peridotite shear zone to residual material, probably formed during partial melting of the dyke during frictional heating (*see section 4.6, Evidence of pseudotachylytes*). The phase map (Fig. 7a) was divided into 4 regions, each with a distinct composition (Table 3) and texture. Region 1 contains a clast of hornblende pyroxenite restite, formed through partial melting of a hornblende gabbronorite dyke, region 2 consists of what is apparently recrystallized pseudotachylyte, while regions 3 and 4 are most like the peridotite host rock, with the diopside replaced by finely dispersed dolomite and enstatite. Detailed descriptions of the peridotite can be found in Grant et al. (2016) and Larsen et al. (2018), while the evidence of the replacive dolomite and enstatite is thoroughly discussed in Sørensen et al. (2019). Region 2 has a mixed composition between the dyke and host rock with increased ilmenite and pentlandite, confirmed using EDS. The olivine CPO (Fig. 7c) in the coarse-grained region (Region 4) follows the orientation of a parent grain, with structured local misorientations (Fig. 7a). Moving from region 3 to 1 we observe a progressive weakening of the CPO towards a random configuration. Apart from the parent grains, the average olivine grain size is very fine in all the regions, between 1 and 2 μm EQR, with the finest grain sizes in the high strain regions away from the parent grains (Fig. 7d).

4.3.2. *Low-strain dyke-related shear zone*

Well-preserved hornblende gabbronorite dykes (Fig. 8) allow us to observe the relationship between dykes, host rocks, and shear zones. The hornblende gabbronorite dyke in Fig. 8a may be followed along strike for over 200 m. Shear zones dipping 74° towards 295° exploit both sides of the dyke. Most of the strain was accumulated along the ESE hanging wall. Fig. 8b shows a smaller, equally well-preserved dyke with shear zones exploiting both sides of the structure with minute veins of pseudotachylyte cutting across the shear zones. The westerly shear zone is concentrated in large part within the dyke, seen as the dark foliated region to the left of the image. The shear zone exploits both the dyke and the host rocks and appears as a dark and thin foliated band (2 cm) along the dyke, and a wider (7 cm) band of lighter colored orange rock, containing mostly fine-grained olivine. Fig. 8c shows the same dyke as Fig. 8b, with a significantly more transposed dyke fabric located elsewhere along the strike of the dyke. Dark veins of pseudotachylyte again cut across the shear zone along discrete planes and have a glassy appearance in the field. We prepared two thin sections (A1-2 and A1-3) from a pair of shear zones on either side of a hornblende gabbro dyke (Fig. 8d) for microstructural and EBSD analysis, sampling was done at an adjacent outcrop to preserve the spectacular main locality.

Fig. 9 shows microstructures from the pair of dyke-related shear zones in Fig. 8d. In Fig. 9a, dark bands of hornblende + enstatite + diopside + ilmenite ultramylonite cut the hornblende gabbronorite dyke. Asymmetric plagioclase porphyroclasts within the hornblende-rich high-strain domains indicate that the WNW block of the shear zone moved downwards (Fig. 9b). The porphyroclasts are surrounded by fine-grained pyroxene, amphibole, and plagioclase (Fig. 9c). The tails of the porphyroclasts are recrystallized, with plagioclase, interstitial dolomite, and sub-μm oxides. The relationship between the dyke and peridotite is complex, with a small lens of dyke material completely enclosed within the peridotite zone as in Fig. 4a, and lenses of peridotite surrounded by dyke material (Fig. 9d). Along other contacts we observe simpler relationships (Fig. 9e), probably due to the lower amount of strain accumulated along smaller (≈100 μm wide) shear zones. These better-preserved contacts show evidence of fracturing and fluid infiltration from the dyke into the olivine (Fig. 9e and f) most notably as traces of small carbonate grains along microfractures following crystallographic planes. XRD analyses of the hornblende gabbronorite dyke protolith gave Ab – 30 wt%, Di – 26%, En – 21%, Hbl – 15%, Ilm – 5%, Bio – 1% and Fo – 1%. The higher-strain assemblages contain less pyroxene and more amphibole: Hbl – 34%,Plg – 30%, Di – 17%, En – 12%, Ilm - 4%, Fo – 2%, and Bio - 2%. The shear zones exhibit a variety of CPOs in different mineral phases. (Figs. 10 and 11). Sample A1-2 is from entirely within the dyke assemblage (Fig. 10a). Both the plagioclase and hornblende CPO are weak (Fig. 10b). In the highest strain areas (Region 3 and 4) there is minor alignment of the b-axis in plagioclase, with J-indices as high as 1.9 and 2.1, respectively. This could be attributed to inheritance from parent porphyroclasts, though a b-axis maximum normal to the shear zone foliation is expected during the dynamic recrystallization of plagioclase (Mehl and Hirth, 2008). The b-axis maxima are normal to the shear zone boundary, while a weak a-axis girdle is parallel to the boundaries. Hornblende, the most prevalent phase in the shear zone, is very fine-grained (Fig. 10c). Apart from a few preserved parent grains on the periphery of the shear zone, the grain sizes range from 2 to 7 μm, with peaks between 3 and 4 μm (EQR).

The second sample from the pair of shear zones (A1-3) contains peridotite ultramylonite in addition to dyke-derived assemblages (Fig. 11). The contact between the ultramafic lens and the dyke is fine-grained, indicating local accumulation of strain. The olivine grains display similar textures to those in the high-strain shear zones, with fractured parent olivine grains and ultra-fine-grained ultramylonite (Fig. 11a and b). The phase maps from A1-3 (Fig. 11b) show a progressive change from a peridotite to a dyke-related assemblage, from left to right. Between the two lithologies we observe a reaction texture,

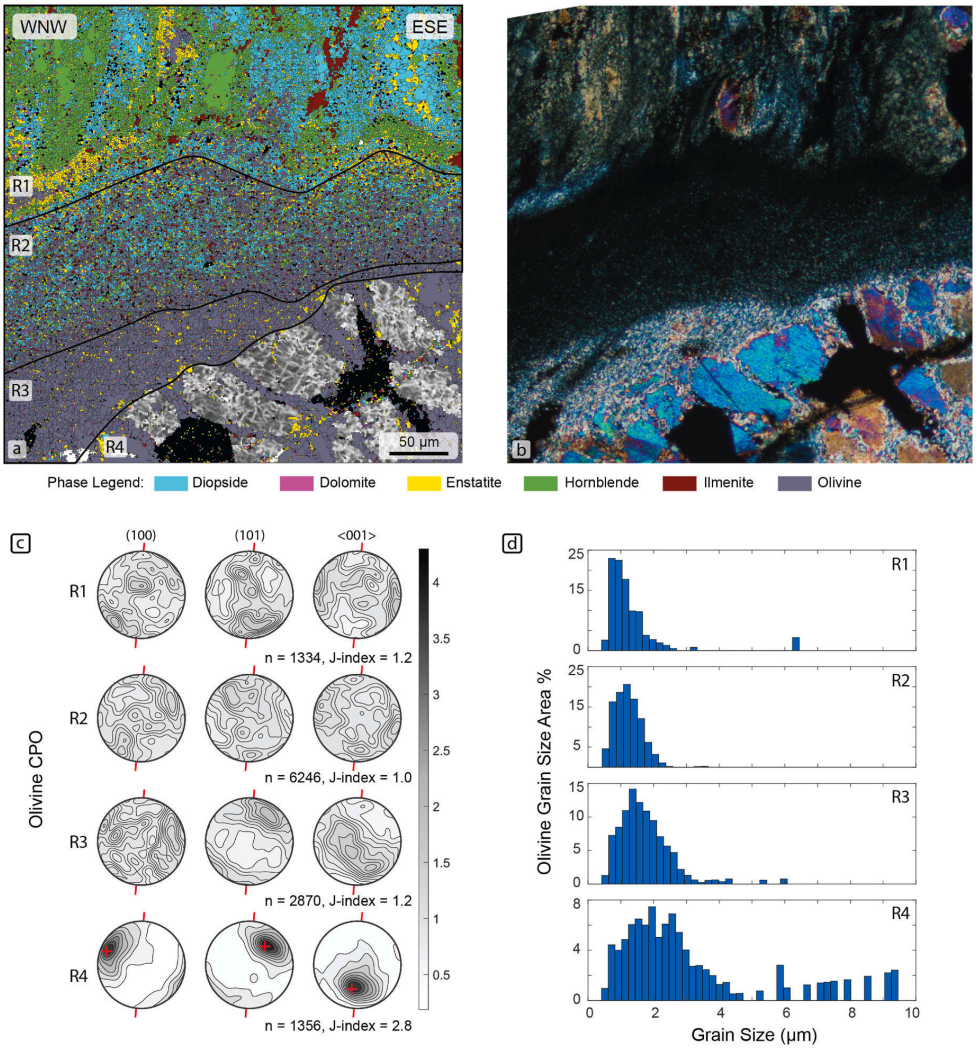

Fig. 7. EBSD data from sample A1-1b. (a) Combined phase and kernel average misorientation (KAM) map (b) Corresponding CPL image (c) Pole figures of the (100), (010) and <001> planes for olivine in each region, with the orientation of the sample stretching lineation denoted by red bars. "n" denotes the number of grains. (d) The grain size of olivine within each region, shown in EQR area %. (For interpretation of the references to color in this figure legend, the reader is referred to the Web version of this article.)

Table 3
Composition by area percentage of each mineral phase in the four regions of Sample A1-1b (Fig. 5), cubic phase predominantly pentlandite and ilmenite with minor chalcopyrite.

	R1	R2	R3	R4
Olivine	6.8	54.7	89.6	81.3
Hornblende	37.6	8.6	0.2	0.3
Diopside	34.5	18.7	0.8	0.5
Ilmenite	5.7	5.6	1.0	0.6
Dolomite	2.0	1.6	1.3	0.7
Enstatite	10.7	7.7	4.8	3.7
Cubic Phase	2.5	3.0	2.3	11.7

comprised by a hornblende-bearing zone (R6) towards the gabbronorite dyke and orthopyroxene towards the peridotite (R7). The KAM map (Fig. 11b) shows internal misorientations in the olivine parent grains. There is notably less organization of the internal misorientation structure here compared to the high-strain samples (Figs. 5–7). In this sample the local misorientation structures form small cells or subgrains, rather than planar deformation features, as described by Lopez-Sanchez et al. (2021). The bands of recrystallized olivine within the parent grain are more chaotic and significantly thicker than in the high-strain samples. The large parent olivine grains control the CPO, with regions 2–4 showing similar CPOs to the large grain in region 1 (Fig. 11c), with weakening in finer-grained domains. The grain size distributions show very fine grain sizes, with most grains less than 5 μm (EQR) (Fig. 11d). The misorientation angle diagram (Fig. 11 e), shows a very high frequency of small (<5°) misorientations, indicating the presence of

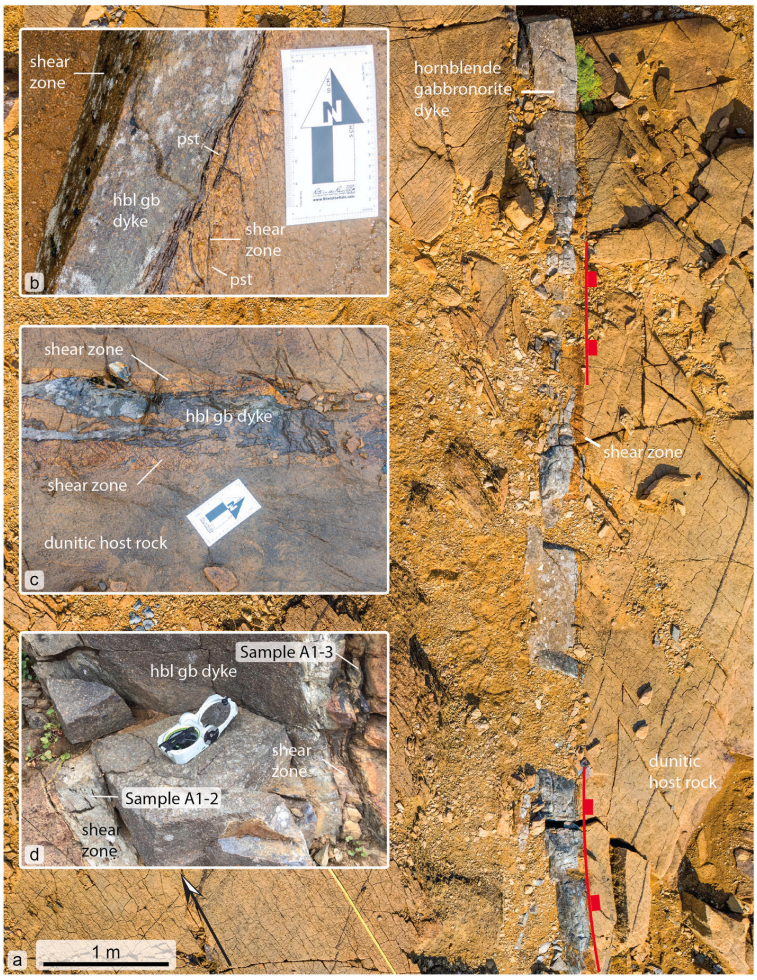

Figs. 8. 3D Model in map view and field photographs showing relations between the dyke and related shear zones. (a) An example of a dyke related shear zone. The orange-colored shear zone, hornblende gabbronorite dyke, and dunitic host rock are labeled accordingly. Notice the darker orange zone surrounding the dyke. This change in color is common within the high-strain shear zones which rework the dunitic host rock. (b) Shear zone along the SE side of a gabbroic dyke with small NS-trending pseudotachylytes veins. The NW side of the dyke is also deformed, though it appears that most of the strain was accommodated by the dyke itself which now displays a pervasive foliation. Pst = pseudotachylyte. (c) A transposed dyke reworked by a dyke-related shear zone. (b) and (c) show the same dyke-related shear zone in which the amount of strain accommodated by the dyke apparently varies along strike, with the most transposed and highly deformed section of dyke shown in (c). (d) Sampling locations for sample A1-2 and A1-3, representing the ultramafic and mafic portions of a dyke-related shear zone like that shown in (a). The compass rests on an undeformed hornblende gabbronorite dyke. The outcrop shown in (a) remains unsampled to preserve the spectacular field exposure. (For interpretation of the references to color in this figure legend, the reader is referred to the Web version of this article.)

subgrains in olivine or a relation of new grains to the parent grain. The hornblende CPO are weak, whilst the plagioclase CPO exhibit clear b-axis maxima normal to the shear zone foliation (Fig. 11f). 1–3 μm (EQR) enstatite and dolomite grains (Fig. 11g) populate the shear zone and are ubiquitous in our samples.

4.4. Area 2 - the main shear zone

The main shear zone dips 31° towards 101° with sparse, ESE-trending mineral lineations along a mostly flat-lying foliation and is marked by increasing strain towards the shear zone core (Fig. 12). The deformation zone extends over 15 m into the footwall (Fig. 12a), while the hanging wall is less deformed. Slabs cut in the field reveal only minor serpentinization and a clear S-foliation indicating an ESE transport direction (Fig. 12b). The core of the shear zone is 5–10 m wide (Fig. 12b and c) and fluctuates along strike. We define the core based on the field expression of the shear zone, where a 10–20 m wide and 3- to 4-m-deep depression stretches for 2 km along strike. Networks of millimeter to centimeter scale ultramylonitic or cataclastic bands brecciate the peridotite (Fig. 12d), while transposed dykes (Fig. 12e), including major gabbronoritic dykes, populate the deformation zone, increasing in intensity towards the main shear zone.

4.4.1. Petrography of the main shear zone

The main shear zone mineral assemblage resembles the dyke-related shear zones, though we observe a more thorough mixing of phases (Figs. 12 and 13). Within the most deformed domain, significant strain obliterated fragments of dykes like those observed in the dyke-related shear zones, though we suspect diopside and hornblende-rich lenses may be the remnants of dykes. This is consistent with our observation of large gabbronoritic dykes bordering the main shear zone. Serpentinization is restricted to small veinlets, leaving the structural fabric of the rock intact, though local serpentinization occurred along olivine grain-boundaries. XRD data from sample A2-2 constrained the following assemblage: Ol – 37%, Liz – 28%, Chl – 13%, Hbl – 9%, Talc – 4%, Mag – 3%, Mgs – 3%, Dol – 2%. The fine-grained fabric of the rock makes the separation of individual assemblages difficult, and the analysis includes late alteration phases. Lenses of mafic ultramylonite from deformed dykes crop out along the shear zone and contain the following mineral assemblage: Hbl – 45%, Ab – 43%, Grt – 4%, Bio – 4%, and Ilm – 4% based on XRD.

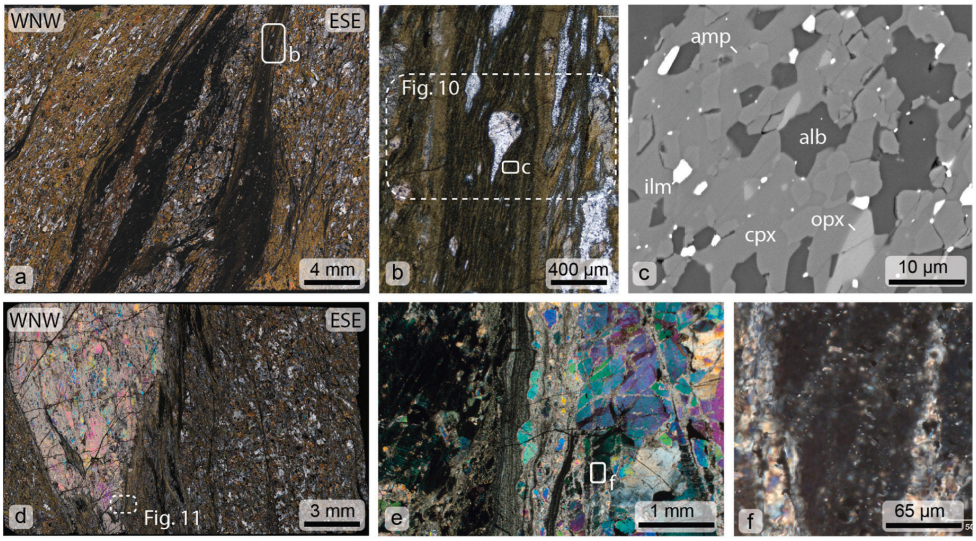

Fig. 9. Microstructures and textures along the dyke-related shear zones from sample A1-2 (a–c) and A1-3 (d). (a) Thin section (A1-2) scan of a hornblende gabbronorite shear zone with dark bands of ultramylonite. (b) Sigmoidal plagioclase clasts within the ultramylonite. The inset was investigated using EBSD (Fig. 9) (c) BSE image, where fine-grained interstitial phases are apparent. (d) Thin section scan of sample A1-3. The scan includes a zone of peridotite ultramylonite mostly surrounded by ultramylonitic hornblende gabbronorite (e) A well-preserved contact between a dyke (left) and the host rock (right). (f) Small bright grains (≈1 μm) of carbonate phases in an extinct olivine grain.

4.4.2. Structural fabric of the main shear zone

Distinct strain localization occurred surrounding the main shear zone. Fig. 13 (a) through (c) show thin sections from samples collected with decreasing distance to the main shear plane. The most distal of the thin sections (A2-1) (Fig. 13a) contains a discrete <0.5 cm band of ultra-fine-grained olivine, part of the irregular network of ultramylonitic or cataclastic bands which rework peridotite (Fig. 12d). The band is surrounded by fractured olivine clasts, while the lower portion of the thin section contains well-preserved olivine with minor serpentine veinlets. Fig. 13b shows a thin section (A2-2) taken adjacent to the highest strain domain of the shear zone. This thin section contains olivine protomylonite and mylonite, as well as lighter areas of altered transposed dykes, containing increased amphibole and pyroxene (Fig. 13b). The final thin section (A2-3) (Fig. 13c) was taken from the core of the main shear zone. Textures surrounding the shear zone show significant strain localization (Fig. 13d). A distinct SC-foliation within the olivine ultramylonite indicates an ESE transport direction (Fig. 13e), consistent with the macrostructures in Fig. 12b. Interstitial secondary phases, including amphibole, clinopyroxene and orthopyroxene, characterize the olivine fabric (Fig. 13f). The fine-grained texture of the rock stands in contrast to the protolith, which contains olivine grains up to cm size.

Using EBSD, we mapped a 3 by 0.5 mm zone across both olivine-rich and more hornblende and diopside-rich high-strain domains (sample A2-3) (Fig. 14a). We divided the EBSD map into four regions, based on textural and compositional similarities. The phase map (Fig. 14b) shows dolomite and enstatite grains, and local hornblende and diopside as interstitial grains between olivine. The dolomite is distributed throughout, though the highest concentration occurs together with very fine-grained olivine at the border between regions 1 and 2. A small serpentine veinlet cuts the ultramylonite (Fig. 14c). The vein is discrete and the ultramylonitic fabric is well-preserved. Fig. 14d shows the complex mineral fabric of olivine, amphibole, pyroxenes, and ilmenite typical of the main shear. The darker olivine-rich bands and the lighter olivine + pyroxene + amphibole rich bands are ultramylonitic, with an average grain size of 7 μm EQR in the olivine-rich domains (region R1) and 4–5 μm EQR in the pyroxene/hornblende rich bands (region R4) (Fig. 14e and f). Grain sizes range between 2 and 12 μm (EQR) in the olivine regions (Fig. 14e), with the highest strain region (R4) exhibiting the finest olivine grain sizes. Hornblende, enstatite, dolomite, and ilmenite are all extremely fine-grained, with peak grain sizes between 2 and 4 μm EQR (Fig. 14f). Rare grains with ca. 75 μm EQR remain in the sample. The CPO of olivine is weak in all regions (Fig. 14g), and nearly random with J-indekses between 1.1 and 1.3. The CPO in region 2 may be reminiscent of a weak A-type olivine fabric (Ismail and Mainprice, 1998), particularly for [100] and [010] axes.

Two samples are represented in the misorientation angle diagrams, including sample A1-1a (Fig. 15a) and A2-3 (Fig. 15b). The samples show very similar trends between low strain and high strain domains. The low strain domains, which we here define as areas with preserved parent grains, contain high frequencies of low angle misorientations, significantly greater than expected for both the uncorrelated and untextured misorientation angle frequencies. In contrast, the high strain areas show only very slight increases in low angle misorientations and generally follow the trend of both uncorrelated and untextured olivine misorientations.

4.5. Evidence of pseudotachylytes

We document dark ultra-fine-grained bands which we interpret as pseudotachylytes (Fig. 16). Most of these pseudotachylytes form at the expense of the gabbronoritic protoliths, particularly at the interface between gabbronoritic and peridotite lithologies, with veinlets of pseudotachylyte extending from the gabbronorite into less deformed rocks (Fig. 16a). The formation of pseudotachylytes at dyke – peridotite interfaces is also particularly apparent in Fig. 4. A section of the pseudotachylyte vein (Fig. 16b) shown in Fig. 16a, now devitrified and recrystallized was used to estimate PT-conditions during recrystallization. The pseudotachylytes exist within the ultramylonites of both gabbroic and dunitic origin (Fig. 16c and d), sometimes cutting the foliation or shear zone fabric obliquely at high angles. The pseudotachylytes contain high concentrations of phases containing incompatible elements as ≈ 1–4 μm EQR ilmenite, pyrrhotite, and chalcopyrite.

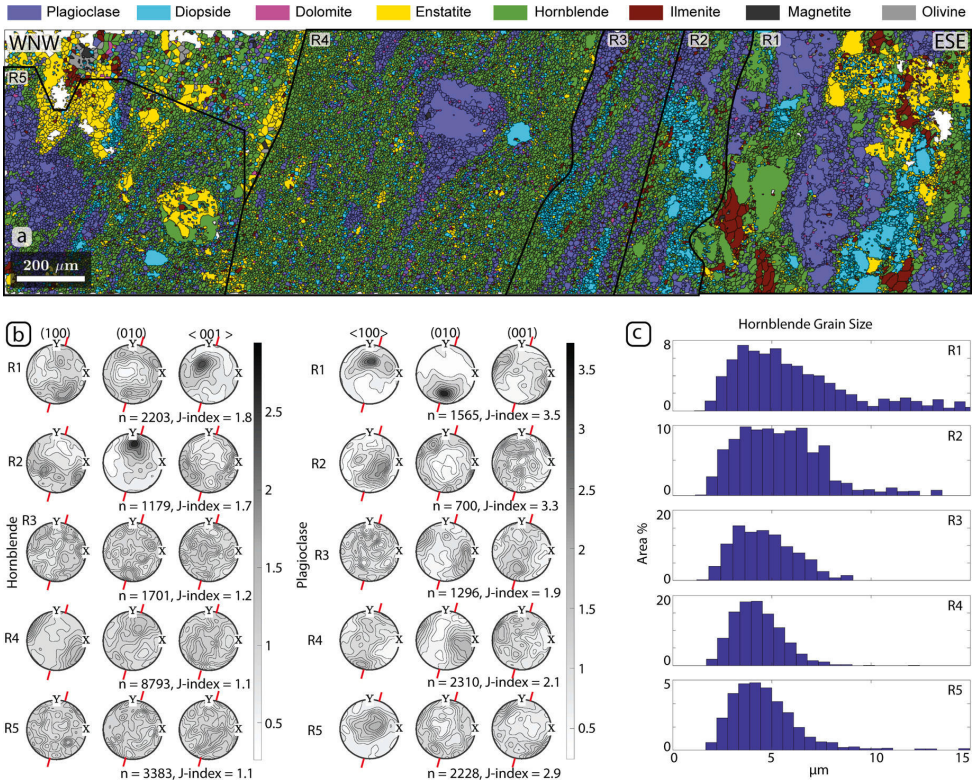

Fig. 10. EBSD data from a dyke-related shear zone (Sample A1-2) shown in Fig. 8 (a) Phase map across the ultramylonitic band, and a sigmoidal plagioclase clast indicating the transport direction along the shear zone. (b) CPO of hornblende and plagioclase for each of the regions denoted in (a) "n" denotes the number of grains. (c) Grain size distribution of hornblende in each of the regions. The higher strain regions have the smallest grain sizes.

These phases contribute to the dark, opaque appearance. Continued plastic deformation along the shear zones recrystallized the pseudotachylytes and incorporated them into the ultramylonites. The pseudotachylytes show varying degrees of recrystallization and the relationship between different deformation styles (Fig. 16c, d, e). In Fig. 16e, the different pseudotachylytes are labeled accordingly. The most significant distinguishing factor between the pseudotachylytes, apart from their cross-cutting relationships (Fig. 16d) is the degree to which they have been recrystallized and incorporated into the ultramylonitic fabric of the shear zones. What we interpret as earlier generations of pseudotachylyte are generally coarser grained, showing higher degrees of recrystallization than their more recent counterparts. Grain sizes within the ultramylonites diminish in proximity to the pseudotachylytes, creating ultrafine-grained assemblages in both the ultramafic and hornblende gabbronorite assemblages (Fig. 16e).

5. Discussion

A single tectonic model accounts for the structural framework constituted by the main shear zone and the dyke-related shear zones. Similar PT-estimates, mineral assemblages, alteration, and microstructures indicate approximately coeval activity along the shear zones within both ultramylonitic and pseudotachylyte domains. There is no evidence of cross-cutting relationship between the dyke-related shear zones and the main shear zone, which could constrain a sequential deformation history. This section considers the evolution of the shear zones as a unified structural framework.

5.1. Geothermobarometry

The pressure and temperature estimates presented in our study indicate slightly higher metamorphic grades than previously published from the Seiland Igneous Province (SIP). Gasser et al. (2015) used thermodynamic modelling and garnet isopleths to model PT conditions of metasedimentary rocks in the southwest SIP. They found pressures between 6.8 and 9.3 kbar and 730 °C – 745 °C in an assemblage dated to 702 ± 5 Ma and 10–12 kbar and 600 °C - 660 °C in 420–440 Ma rocks. On the Øksfjord Peninsula, Menegon et al. (2011) used thermodynamic modelling to estimate PT conditions during shearing in migmatitic gneisses, with results between 760 °C and 820 °C and 7.5 kbar–9.5 kbar. Griffin et al. (2013) estimated PT conditions during magmatic cooling in Nordre Brumannsfjord to 743 °C – 882 °C, with an assumed pressure of 10 kbar, and the emplacement of gabbroic and ultramafic rocks at 8 kbar and 10 kbar respectively. Considering the extent of the SIP, spanning almost 100 km from the NE to SW corners, it is not surprising that a range of pressure and temperature estimates exists. A complete summary of the existing geothermobarometry is available in Larsen et al. (2018).

Earlier studies regarding the emplacement conditions of the RUC and its dykes are consistent with our estimates (Grant et al., 2016; Larsen et al., 2018; Orvik, 2019). Grant et al. (2016) estimated pressures and temperatures up to 10.5 kbar and 1120 °C, respectively using two pyroxene thermobarometry in the wehrlite. Orvik (2019), estimated pressures between 12 and 14 kbar and temperatures between 1010 and 1045 °C in a variety of dykes, using the Ridolfi et al. (2010) and Molina

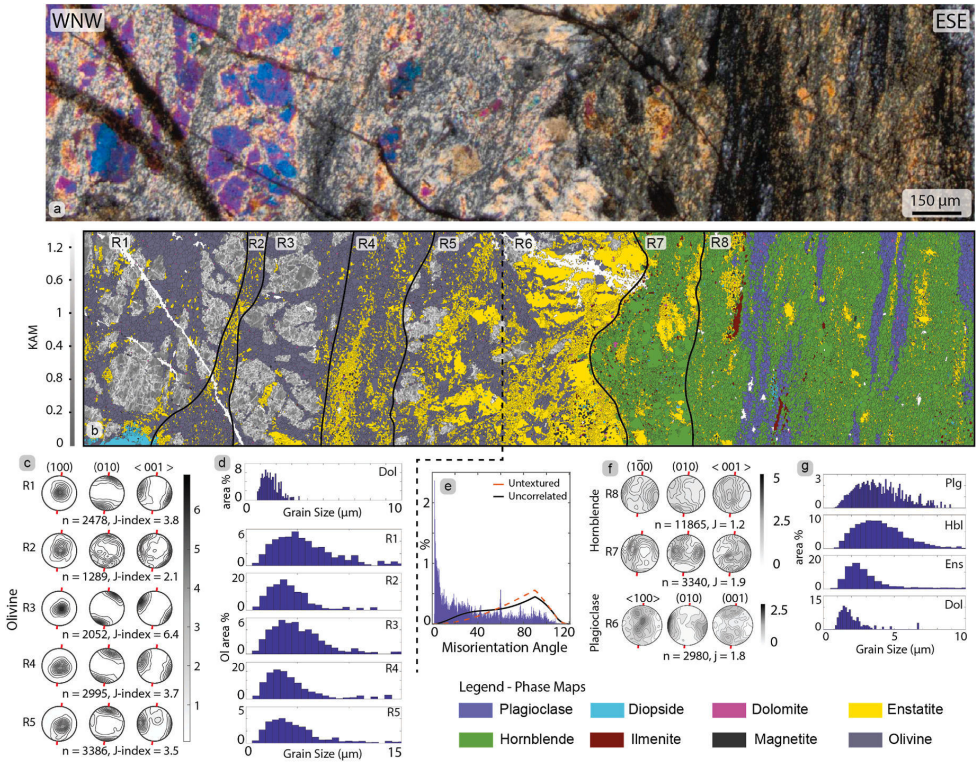

Fig. 11. EBSD data from a dyke-related shear zone (Sample A1-3), divided into a peridotite domain and a hornblende-rich domain. The dashed black line separates the domains which were analyzed separately using EBSD. (a) Microphotograph of the mapped area (b) Phase map of the dyke-related shear zone with KAM for the parent olivine grains. (c) Olivine CPO in each region. The letter "n" denotes the number of grains. (d) Grain size distribution of dolomite and olivine. (e) Misorientation angle plot for olivine grains in the mapped area. The high frequency of low angle misorientations can be attributed to dislocation glide within the olivine and the similar orientation of new grains to their parent grains, typical of low strain zones where parent olivine grains are preserved (f) CPO for hornblende and plagioclase from the hornblende-rich zone. (g) Grain size distribution for plagioclase, hornblende, enstatite, and dolomite in regions 7 and 8.

et al. (2015) empirical models. Larsen et al. (2018) estimated temperatures between 940 °C and 1180 °C using the methods described in Ridolfi and Renzulli (2012), and pressures between 11.6 and 15.46 kbar using the method described in Molina et al. (2015). Finally, thermodynamic modelling of mineral assemblages indicates minimum pressures of 9 kbar (Larsen et al., 2018; Sørensen et al., 2019). The pressure and temperature estimates presented in this study fall within these ranges and indicate very high-grade metamorphic conditions. However, the methods employed by our study and previous studies have limitations.

Erdmann et al. (2014) identified shortcomings in pressure estimates based on Ridolfi et al. (2010) and Ridolfi and Renzulli (2012). However, Ridolfi's methods provide adequate temperature estimates, owing to the strong dependence of amphibole composition on temperature (Erdmann et al., 2014). Equation 1d (eq. 1d) from Ridolfi and Renzulli (2012) also provides reasonable pressure estimates (Molina et al., 2015), and is therefore included in our study. The amphibole – plagioclase Al/Si partitioning barometer from Molina et al. (2015) removes the short comings of the Ridolfi methods for assemblages between 650 °C and 1050 °C. Using Ridolfi's methods to estimate temperatures in our rocks and Ridolfi and Renzulli (2012) eq. 1d and Molina et al. (2015) we find temperatures between 850°–1150 °C and pressures between 10 and 15 kbar (Fig. 2). Considering the consistency with previous studies and the applicability of the applied empirical models to our input data, we feel confident in the accuracy of our PT estimates for the given assemblage.

The PT analysis of recrystallized pseudotachylytes indicates that pseudotachylyte formation also occurred at lower crustal conditions, with pressures between 9 and 12 kbar and temperatures between 850° and 950 °C (Fig. 2). We interpret the analyzed zone (Fig. 16a and b) to be thoroughly reworked, having first formed as a pseudotachylyte before devitrifying and recrystallizing to the ultra-fine-grained assemblage we analyzed. This removes any uncertainty regarding a potential magmatic origin of the analyzed equilibrium state. It should be noted that while the analysis of a recrystallized pseudotachylyte does not directly indicate the conditions during pseudotachylyte formation, the similarity of the PT-estimates from rocks both cut by (A1-2 and A1-3) and post-dating the pseudotachylytes (Molina Pst) (Fig. 12) make a strong argument for the formation of the pseudotachylytes having taken place at lower crustal conditions. Considering the progressive exhumation and cooling of the lower crustal RUC described by Larsen et al. (2018), any later recrystallization and re-equilibrium of the pseudotachylyte assemblage would have resulted in lower PT estimates than correct for the formation of the pseudotachylytes. As such, we consider our PT estimates to be minimum estimates for the RUC pseudotachylytes, strengthening our interpretation of a lower crustal origin.

While our PT-estimates seem accurate, uncertainties exist as to what the values represent. The high temperatures (850°–1150 °C) indicate that the main shear zone and dyke-related shear zones formed shortly after the emplacement of the RUC, while the ambient temperature was still high. The pressure estimates (10–15 kbar) place the structures in the lower crust, consistent with the geodynamic setting proposed by Roberts

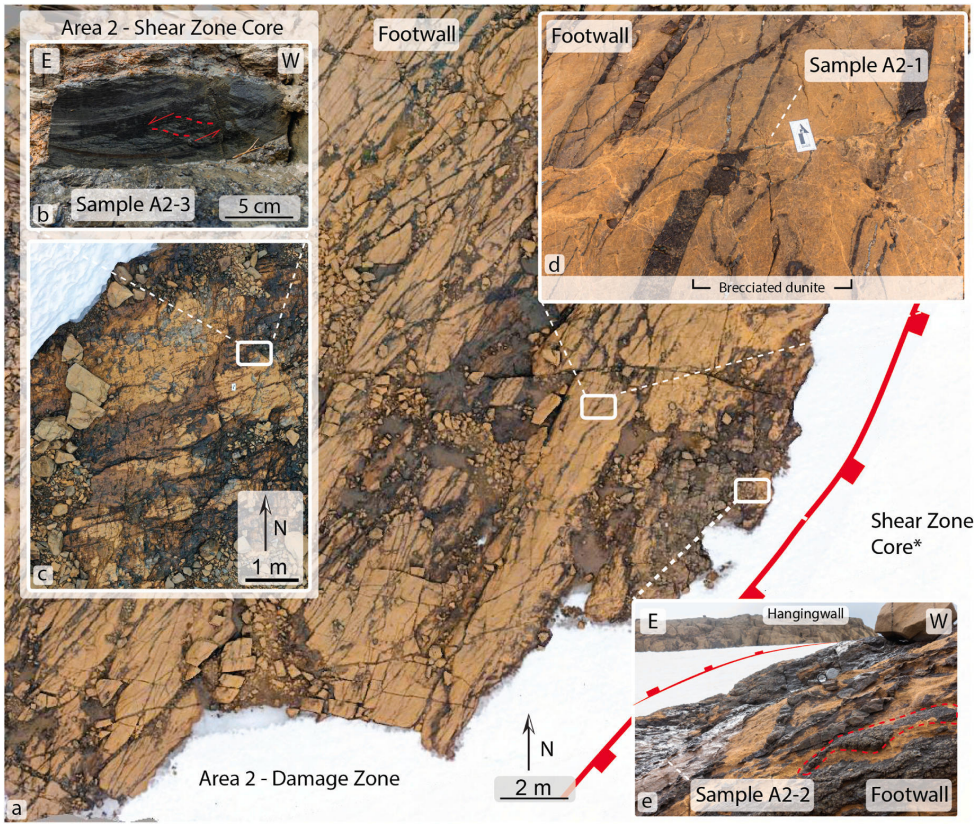

Fig. 12. Map view of 3D model from the main shear zone. a) A network of dykes and sampling locations found in the deformation zone in the footwall of the main shear zone. There is a high frequency of dykes surrounding the shear zone, many of which were apparently incorporated into the zone itself. *The core of the shear zone is generally covered in snow, though inset (b) and (c) show Sample A2-3, from the highest strain domain from the core of the main shear zone. (d) Sample location for A2-1 and a network of orange, ultra-fine-grained zones, brecciating the peridotite host rock in the footwall of the main shear zone. (e) Sampling location for A2-2, with folded and transposed dykes along the boundary to the highest strain domain and shear zone core. (For interpretation of the references to color in this figure legend, the reader is referred to the Web version of this article.)

et al. (2006) and Larsen et al. (2018) for the RUC and Sørensen et al. (2019) for the dyke-related shear zones. However, the direct relation of our samples to high-strain shear zones complicates the interpretation of these structures. Viscous dissipation causes elevated temperatures during ductile deformation (Griggs and Baker, 1969; Braeck and Podladchikov, 2007) while volume-expansion documented in these shear zones (Sørensen et al., 2019) and the generation of melt could lead to locally elevated pressures. Such locally elevated pressures related to frictional melts have been documented in structures linked to lower crustal earthquakes (Zhong et al., 2021), although it is unlikely that short lived temperature and pressure fluctuations like those documented in our study would cause re-equilibration in the mineral assemblage, recrystallized after the frictional melting event. In addition, later re-equilibration in the ascending RUC (Larsen et al., 2018) would have resulted in lower pressure and temperature estimates. This adds to our confidence that the pseudotachylytes did form in the lower crust, at elevated pressures, reaching temperatures above 800 °C during deformation.

5.2. Shear zone development

5.2.1. Initial deformation and the role of magmatic fluids

The shear zones form along pre-existing heterogeneities, namely dyke-host rock contacts, as described in similar lithologies by Toy et al. (2010), often extending into the peridotite away from the dykes themselves, or obliterating the dyke completely (Fig. 3). The frequency of transposed dykes in the deformation zone surrounding the main shear zone, and dykes which by geometrical association must have been included in the main shear zone core indicates that magmatic activity was important for the development of all shear zones in the RUC. The peridotite was apparently altered along the dykes before or during shearing, allowing strain to localize in the stronger rocks. The olivine grains adjacent to the dyke-related shear zones may have been primed for deformation by the intrusion of the dykes. We document evidence of fluid infiltration from the dyke into olivine grains (Fig. 4d and e, and 9f). Our samples contain an increase in dolomite adjacent to the dykes, including in the main shear zone where the remnants of dykes are highly transposed, but still observed as hornblende- and diopside-rich lenses with significant dolomite. During dyke emplacement, reactions between olivine, orthopyroxene, and C–O–H magmatic fluids formed enstatite and dolomite-bearing assemblages, as thoroughly described by Sørensen

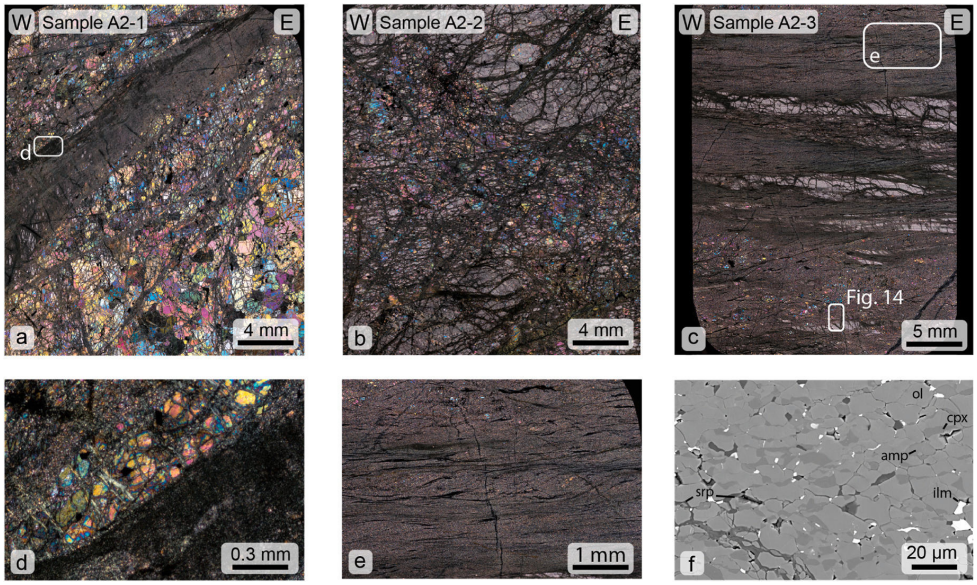

Fig. 13. Microstructures from the main shear zone in Area 2. (a) Dunite from sample A2-1 with a thin (4–6 mm thick) band of ultramylonite, located approximately 10 m into the footwall of the main shear zone. The dark band within the ultramylonite is recrystallized pseudotachylyte. (b) Protomylonite – ultramylonite from sample A2-2 sampled adjacent to the core of the shear zone. The black veinlets are serpentine. (c) Ultramylonite from the highest strain zone of the main shear zone, sample A2-3. The light bands contain more hornblende and diopside than the darker areas. Larger, relics of olivine grains appear as colored, small grains in the lower portion of the thin section. (d) The transition from relatively coarse grained, fractured olivine to a dark ultra-fine-grained olivine, pyroxene, amphibole assemblage. (e) SC-foliation showing top-to-East transport direction in the main shear zone. (f) BSE image from the shear zone core.

et al. (2019). The formation of carbonates (<1 μm EQR) and enstatite along microfractures weakened the olivine grains, providing a locus for deformation. The microfractures in the olivine grains allowed the fluids to migrate through what were originally single crystals, weakening the rock and contributing to strain localization. Locally, the alteration reaction reversed, with the formation of sub-micrometer interstitial diopside amongst the recrystallized olivine grains (Fig. 6a). The equilibration temperature of the pseudotachylyte assemblage exceeds the PT-stability of the dolomite + enstatite assemblage (Fig. 12), hence it would be expected that at least some decarbonation resulted from the frictional heating, something that is confirmed by rarity of enstatite-dolomite grain contacts and diopside inside the shear zones. Frictional heating may have broken down the dolomite and released CO_2 for continued migration along the shear zone. The most important result of fluid migration is the introduction and distribution of new phases along the grain boundary network, which helped maintain very fine grain sizes (2–4 μm EQR) during later deformation. The grain size reduction created a much weaker rock, by a factor of 100 (Sørensen et al., 2019), setting the stage for intense strain localization.

The frequency of shear zones along specific dyke lithologies illustrates the relationship of the shear zones to volatile fluids. The shear zones develop preferentially along volatile-rich hornblende gabbronorite dykes, whereas the majority of pyroxenite and lamprophyre dykes are left undeformed and offset by the shear zones. Volatile content may also have controlled the width of the dyke-related shear zones, with the highest volatile contents leading to wider zones of microfracturing in the peridotite. The microfracturing of olivine grains and extent of the shear zones into the peridotite host rock also suggests that the presence of volatiles, rather than a weak dyke rheology, was paramount in localizing deformation. Had the weak dyke been the cause of strain localization, rather than the fluids, we would expect strain to localize entirely within the dyke and not in the surrounding host rock.

5.2.2. Subgrain structure in relic olivine grains

Subgrain structures exist within the parent olivine grains, including planar deformation features and subgrain cells. The processes which first generated the planes of new grains appear to have continued, creating wider zones of new grains, and locally replacing the parent grains with a polymineralic fine-grained mass. Within the parent grains, the planar structures follow specific crystallographic orientations and are precursory to the recrystallized fractures within the same grains, which are themselves characterized by the alteration assemblage of dolomite and enstatite. Examples of such subgrain structures are documented for olivine in chondrites (Carter et al., 1968; Ruzicka and Hugo, 2018), and other minerals in extremely high-stress environments (Austrheim et al. (2017), and references therein) formed through processes unlikely to have occurred within the RUC. The subgrain cells identified in KAM maps are very similar to textures described by Lopez-Sanchez et al. (2021) attributed to subgrain rotation in olivine. That study also documents a weakening of CPO in fine-grained olivine without invoking grain boundary sliding, but rather through subgrain rotation. Other studies (Druiventak et al., 2012; Matysiak and Trepmann, 2012, 2015) have investigated deformation in olivine at similar lower crustal conditions and identified similar structures formed during transient changes in differential stress as a part of the deep earthquake cycle.

In our rocks, the characteristic subgrain structures and prevalence of both twist and kink subgrain boundaries (Fig. 5) confirm the plastic deformation within the large olivine grains. We suggest that the formation of these structures was vital to shear zone development, weakening the peridotite host rock, increasing permeability, locally reducing grain size, and even controlling the position of the shear zone boundaries. The fine grain size was maintained by the presence of secondary phases pinning the grain-boundaries. As deformation progressed, strain localized within the polyphase domains through grain-size sensitive creep, similar to the deformation focusing mechanism described by Toy

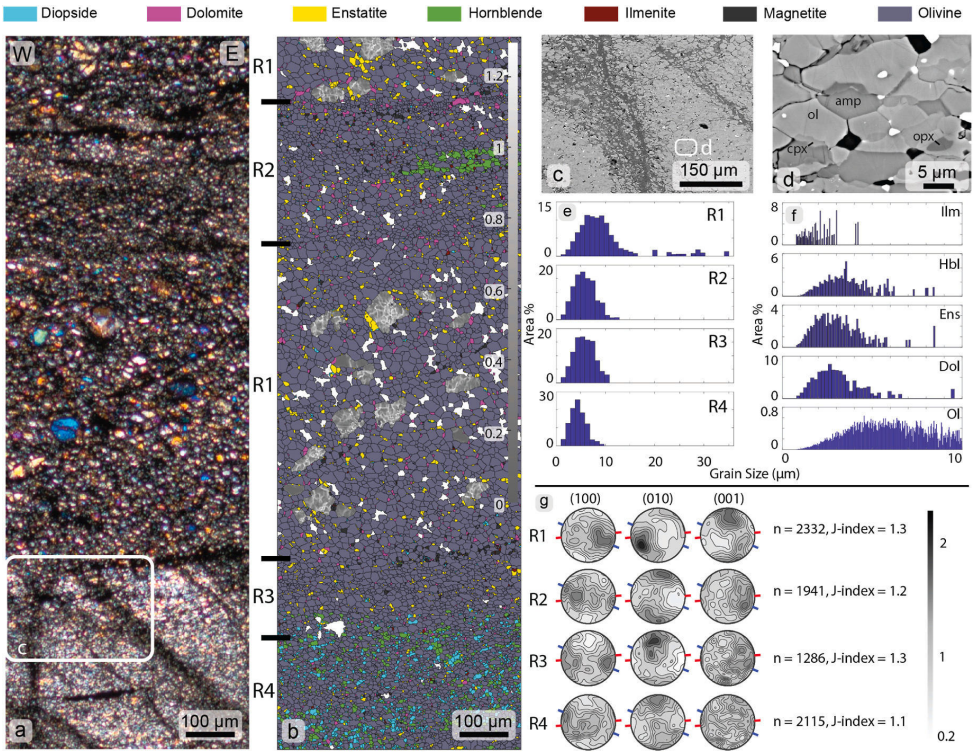

Fig. 14. EBSD data from the ultramylonitic main shear zone (Sample A2-3). (a) CPL image of the EBSD area. (b) Phase map from the EBSD analysis. The grains with KAM maps are parent olivine grains, while the lilac grains are recrystallized olivine. The zones with diopside and hornblende are likely the remainder of completely transposed dykes. (c) BSE image of the lower EBSD area. The black bands are serpentinite. (d) BSE image of the ultramylonitic texture, a complex fabric of olivine, hornblende, pyroxenes, and ilmenite. (e) Grain size distributions for olivine in each of the regions. (f) Grain size distributions for the other mineral phases across all regions. (g) The CPO of olivine in each region. Red bars denote the foliation in the shear zone. Blue bars denote the shear zone boundaries. The letter "n" denotes the number of grains. (For interpretation of the references to color in this figure legend, the reader is referred to the Web version of this article.)

et al. (2010).

5.2.3. *Deformation mechanisms in shear zones*

Our EBSD datasets document a variety of deformation mechanisms in the shear zones. Locally, olivine grains exhibit CPO which may be compared to the well-established type fabrics (Ismail and Mainprice, 1998). The development of subgrain cells in olivine, visible in the KAM maps (Figs. 5–7 and 11) necessitates activity along at least three slip systems in olivine (Lopez-Sanchez et al., 2021). While most of our EBSD analyses resulted in pole figures showing very weak CPOs, some of the larger grains and corresponding fine-grained areas with preserved parent grains show weak type fabrics. The statistical significance of the coarse-grained areas is questionable. We suggest the fine-grained areas to have inherited their fabrics from the parent grains, rather than having formed an actual type fabric, as described by Druiventak et al. (2012). Alternatively, the fabrics could have developed from an initial stage of dislocation glide, as documented in olivine during the initial development of planar deformation features (Matysiak and Trepmann, 2012, 2015). While the new fine-grained regions show a strong orientation related to the parent grains, the more distal fine-grained areas have weaker to random CPOs with lower J-indices, generally not reflecting any fabric at all. Regions 1, 2, 3 and 4 in the ultramafic portion of a dyke-related shear zone (A1-1) (Fig. 5), show stronger fabrics and are comparable to A-type fabrics, as the thin section was oriented normal to the transport direction of the shear zone. We attribute this fabric to the large olivine grain (Fig. 5a), creating a local single grain fabric (Fig. 5b). The areas with the finest-grain size (which indicates significant strain and recrystallization) exhibit relatively weak to random CPOs (Fig. 14). It is probable that the weak to random CPOs are related to diffusion accommodated grain boundary sliding, which may form CPOs in olivine (Drury et al., 2011). The activity of grain boundary sliding is supported by the fine grain size within the shear zones, as well as the wide-spread presence of interstitial phases. The transition from a high frequency of low-angle misorientations in areas near or containing parent grains and characterized by lower strain, to a low frequency of low-angle misorientations in high-strain areas also suggests the activation of diffusion grain boundary sliding in the shear zones (Czaplińska et al., 2015). It should be noted that some studies report strong CPOs resulting from dislocation-accommodated grain boundary sliding (Hansen et al., 2011, 2012), though in our samples only weak to random CPOs develop. This difference could in part be due to the complex mineral assemblage and deformation conditions in nature, compared to the well-controlled conditions in the Hansen et al. (2011) and (2012) experiments. Our results also show a weakening of the CPO in finer grained areas, probably due to a transition to diffusion-accommodated grain boundary sliding or diffusion creep from dislocation creep, consistent with other previous work (Bestmann and Prior, 2003; Warren and Hirth, 2006).

The sample from the main shear zone (A2-3) (Fig. 14) and dyke-related shear zone samples (A1-2 and A1-3) (Figs. 10 and 11) allow us to compare deformation across a variety of assemblages. The CPOs in A1-2, from the mafic portion of the dyke-related shear zone (Fig. 10) are probably related to a multitude of processes. The highest strain region

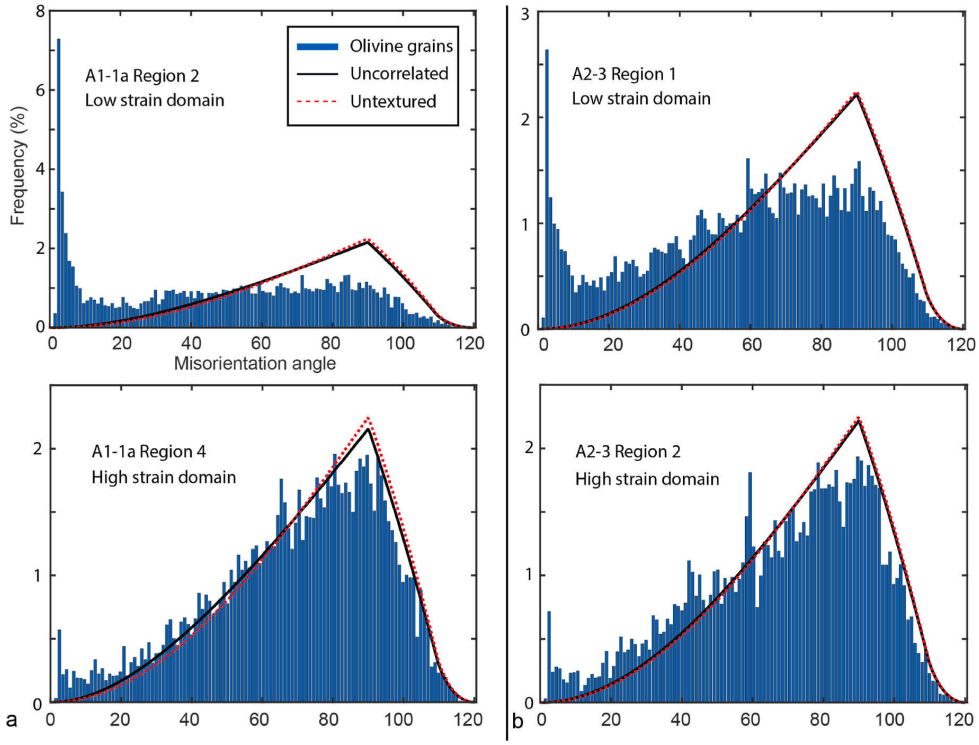

Fig. 15. Misorientation angle diagrams from sample (a) A1-1a and (b) A2-3. The samples show similar trends in the distribution of misorientation angles between olivine grains in low strain and high strain domains. The low strain (A1-1a Region 2) and (A2-3 Region 1) contain numerous relic parent grains and exhibit a high frequency of low-angle misorientation typical of dislocation glide or inherited orientations. The higher strain regions, where no parent grains are preserved, show a low frequency of low angle misorientations, supporting the presence of diffusion accomodated grain boundary sliding.

(R4) has clear, though weak, hornblende and plagioclase CPO's. The hornblende CPO is likely only indicative of the rigid body rotation of amphiboles documented from magmatic flow and in solid-state deformed rocks (Berger and Stünitz, 1996). The plagioclase CPO (Figs. 10b and 11f) may indicate a combination of dislocation creep in the bands dominated by plagioclase and components of grain boundary sliding in the finer-grained zones with mixed composition (Mehl and Hirth, 2008). It is difficult to assess why there is a lack of clear CPO in the remaining regions. The fine grain size and presence of interstitial phases could have contributed to significant grain boundary sliding and diffusion, as the secondary phases helped maintain the fine grain size (Warren and Hirth, 2006; Linckens et al., 2011). As strain localized in the fine-grained regions with significant secondary phases, diffusion creep may have played a dominant role in facilitating deformation in both the hornblende gabbronorite and the peridotite with enstatite and dolomite and promoted weak to non-existent CPO (Linckens et al., 2011).

5.2.4. *Pseudotachylyte formation*

We interpret the dark, ultra-fine-grained bands cutting the ductile deformation fabrics as pseudotachylytes. Pseudotachylytes are only rarely perfectly preserved in nature, with vastly fewer pseudotachylytes recorded than the number of lower crustal earthquakes documented (Kirkpatrick and Rowe, 2013). The pseudotachylytes in our samples, having formed at ambient metamorphic conditions as high as 12 kbar and 900 °C, are, as expected for pseudotachylytes formed at these conditions (Kirkpatrick and Rowe, 2013), completely recrystallized. The most convincing evidence that these features are in fact pseudotachylytes includes the injection vein (Fig. 16a and c), as well as numerous injection veins at the outcrop scale, discrete bands of dispersed immiscible sulfide grains in the recrystallized matrix and the higher content of incompatible elements agreeing with the expected composition of partial melting (Fig. 16b). Finally, flow banding and swirls around relic clasts within the recrystallized pseudotachylytes, following Table 1 in (Kirkpatrick and Rowe, 2013), confirm their origin as frictional melts.

Of critical importance in our field area is the presence of the hornblende gabbronorite dykes. All melts with a traceable origin in our samples originate from lenses of the dykes within the peridotite ultramylonite, or from within the dyke-derived portion of the shear zones. More specifically, the pseudotachylytes form at the interface between ultramafic and dyke-material, with most melting taking place within the dyke material. The core of the main shear zone also contains small domains of what may be recrystallized pseudotachylyte, the origin of which is unclear. We speculate that the most likely origin is hornblende gabbronorite dykes which have either been completely obliterated by extreme strain or are adjacent to the shear zone at depth. The higher offset main shear zone presents a lower preservation potential than the similarly deformed, but lower offset, dyke-related shear zones (Kirkpatrick and Rowe, 2013).

5.3. *Origin of lower crustal earthquakes*

The abundant pseudotachylytes along the well-preserved dyke-related shear zones record numerous deep earthquakes. Many models for the generation of deep earthquakes exist, including self-localizing

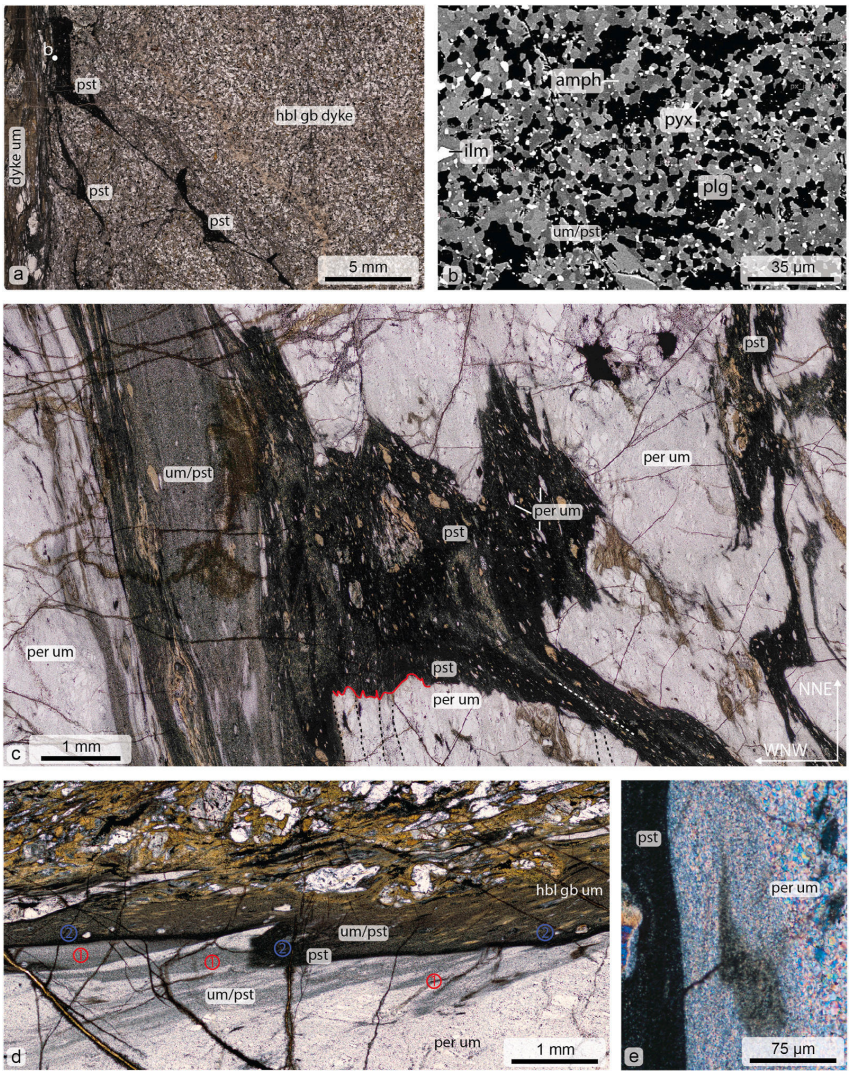

Fig. 16. Pseudotachylyte textures (a) Injection vein texture, with the dark pseudotachylyte vein protruding from a gabbroic ultramylonite into undeformed hornblende gabbronorite dyke. The area where we performed EPMA analysis on a recrystallized, ultramylonitized pseudotachylyte is labeled with a (b). (b) A backscatter image of the recrystallized pseudotachylyte, with amphibole (amph), plagioclase (plg), pyroxene (pyx) and ilmenite (ilm) labeled. (c) A complex zone of pseudotachylytes and ultramylonites from sample A1-1a. Some zones of pseudotachylyte are further recrystallized and mylonitized, while others maintain a dark black color despite wide-spread devitrification. The dark pseudotachylyte contain clasts of peridotite ultramylonite. The red line denotes part of the contact between the pseudotachylyte vein and the ultramylonitic foliation within the peridotite ultramylonite, while the dashed black lines denote the ultramylonitic foliation and the dashed white line denotes the foliation within the well-preserved pseudotachylyte. (d) A second area with pseudotachylytes and ultramylonites. What appears to be two generations of pseudotachylyte can be seen adjacent to the interface of the hornblende gabbronorite and peridotite. A darker generation of pseudotachylyte (2) cuts a lighter generation (1) along the interface. All pseudotachylytes, and the hornblende gabbronorite and peridotite have subsequently been deformed to ultramylonite. (e) A clast of olivine (extreme left) is preserved inside a dark zone of pseudotachylyte. Notice the progressive grain size reduction in the olivine ultramylonite moving towards the pseudotachylyte zone, as well as the "ghost" of mostly recrystallized pseudotachylyte in the fine-grained ultramylonite. pst = pseudotachylyte, um = ultramylonite, per um = peridotite ultramylonite, hbl gb um = hornblende gabbronorite ultramylonite. (For interpretation of the references to color in this figure legend, the reader is referred to the Web version of this article.)

thermal runaway, the downward propagation of stress from shallow ruptures, and fluid and reaction-induced weakening (Jamtveit et al., 2018; Petley-Ragan et al., 2019; Papa et al., 2020). We are not convinced that the structures documented in this study were formed through self-localizing thermal runaway, as such processes may not generate enough heat to form melts, due to significant conductive heat loss (Platt, 2015). Grain boundary sliding, as indicated by our study, is cited as a potential precursor to thermal runaway (Kelemen and Hirth, 2007), though it may also have a prohibitive effect due to the reduction of attainable stresses (Thielmann, 2018). It should be noted that earlier works have proposed the same mechanism for the generation of intermediate-depth earthquakes and peridotite pseudotachylytes in other areas (Deseta et al., 2014). The downward propagation of stress, while plausible and well-documented in other areas (Jamtveit et al., 2018), is not a prerequisite for the structures observed in the RUC. Jamtveit et al. (2018) suggest that the most important effect of downward propagating earthquakes is the increase in permeability along which fluids infiltrate the rocks. We also observe an increase in permeability in the RUC; though in this case related to the emplacement of volatile-rich melts and associated micro-fracturing. The increase in permeability allowed fluids to penetrate the peridotite rocks and led to fluid-induced metamorphic reactions. Deformation localized around the volatile-rich hornblende gabbronorite dykes and in the surrounding peridotite. Thus, magmatic activity via micro-fracturing and fluid reactions causes significant weakening leading to lower crustal earthquakes recorded by the pseudotachylytes. This deep, brittle failure was only made possible via magmatic activity, the emplacement of the dykes, and processes (i.e., fluid infiltration, strain localization) caused by the dykes, a testament to the vital role magmatism plays in localizing deformation within continental rifts. The outcrops documented in this work appear to be an in-situ example of the processes occurring at depth in the East African Rift, as described by La Rosa et al. (2021).

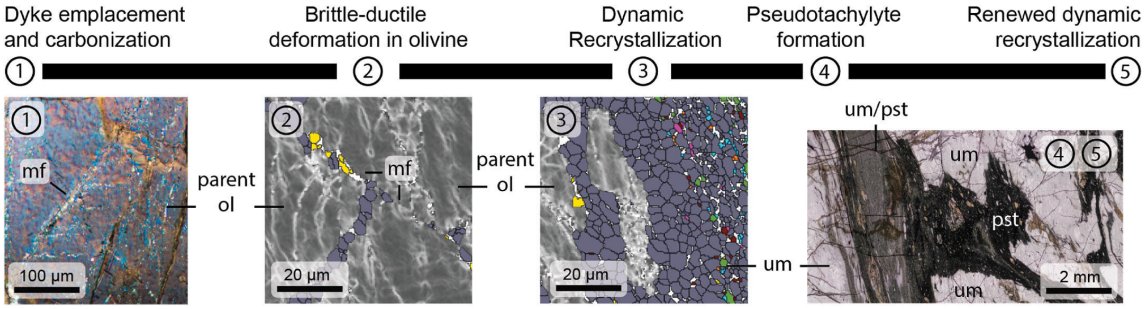

Fig. 17. Simplified timeline of brittle-ductile deformation leading to deep earthquakes in the lower crust. Numbers 1–5 denote the stages of deformation proposed based on the evidence presented in this article. The boxes corresponding to each phase highlight key evidence presented in the article. Box (1) is from Fig. 4d, box (2) and (3) are from Fig. 5a, and box (5)/(6) is Fig. 16c mf = microfracture, parent ol = parent olivine grain, um = ultramylonite, pst = pseudotachylyte, um/pst = devitrified and ultramylonitized pseudotachylyte. The dashed arrow highlights the potential for the formation of new pseudotachylytes following the overprinting of existing pseudotachylytes by ultramylonites.

6. Conclusion

Our results document deformation processes promoted by local heterogeneities and magmatic fluids, leading to deep earthquakes in the lower crust, as summarized in Fig. 17. We documented deformation through a series of five steps:

(1) Dyke emplacement leading to micro-scale fracturing, grain size reduction, and fluid infiltration in the peridotite host rock.
(2) The development of subgrain structures in olivine, including planar deformation features, sub grain cells, and new grains through dislocation creep and corresponding subgrain rotation.
(3) Diffusion accommodated grain boundary sliding and diffusion in fine-grained olivine, accommodated by the presence of secondary interstitial phases within the olivine, inhibiting grain growth despite high temperatures. The high frequency of interstitial phases is related to the presence of dykes and fluid-rock reactions along the dyke-host rock interfaces.
(4) The formation of pseudotachylytes during seismic failure caused by the formation of weaker secondary phases and extreme grain size reduction.
(5) A decrease in strain rate due to stress release, followed by cooling caused the devitrification, mylonitization, and recrystallization of the pseudotachylytes. Heating and cooling during deformation events may have caused repeated carbonation and decarbonation reactions, potentially linking seismicity and CO_2 emissions in rift systems, such as the East African Rift.

The new field evidence documented in this work has important implications for our understanding of deformation and fluid migration in lower crustal mantle-derived ultramafic rocks. The presented evidence documents an example of lower crustal earthquakes, which formed due to local weakening processes along dyke-host rock interfaces, and probably without the outside influence of a remote stress trigger. We hope that our field-based evidence will help extrapolate results from experimental studies and theoretical models to the natural world, thereby improving understanding of deformation and fluid migration from the mantle and lower crust towards the upper crust and finally atmosphere.

CRediT author statement

Eric J. Ryan: Conceptualization, Methodology, Investigation, Writing – Original Draft, Writing – Review and Editing, Visualization; **Bjørn E. Sørensen:** Conceptualization, Methodology, Investigation, Writing – Review and Editing, Supervision, Project Administration; **Kristian Drivenes:** Methodology, Investigation, Writing – Review and Editing; **Rune B. Larsen:** Writing – Review and Editing, Supervision, Project Administration, Funding Acquisition.

Declaration of competing interest

The authors declare that they have no known competing financial interests or personal relationships that could have appeared to influence the work reported in this paper.

Acknowledgements

This work was partly supported by the Research Council of Norway through the funding to The Norwegian Research School on Dynamics and Evolution of Earth and Planets, project number 249040/F60. We sincerely thank Oddmund Hansen for graciously coordinating and enabling our remote and challenging field work. The early draft was vastly improved through suggestions by Julie L. Gresseth. We thank Simone Papa, an anonymous reviewer, and Virginia Toy as editor for thorough and constructive reviews which have significantly improved the quality of our work. Analyses carried out at the EPMA were supported by the Norwegian Laboratory for Mineral and Materials Characterization, MiMaC, project number 269842/F50 of the Norwegian Research council.

References

Andréasson, P.-G., Svenningsen, O.M., Albrecht, L., 1998. Dawn of phanerozoic orogeny in the north atlantic tract; evidence from the seve-kalak superterrane. Scandinavian Caledonides 120, 159–172.
Austrheim, H., Dunkel, K.G., Plümper, O., Ildefonse, B., Liu, Y., Jamtveit, B., 2017. Fragmentation of wall rock garnets during deep crustal earthquakes. Sci. Adv. 3, e1602067.
Bachmann, F., Hielscher, R., Schaeben, H., 2010. Texture Analysis with MTEX–free and Open Source Software Toolbox. Solid State Phenomena. Trans Tech Publ, pp. 63–68.
Bennett, M., Emblin, S., Robins, B., Yeo, W., 1986. High-temperature ultramafic complexes in the North Norwegian Caledonides: I–Regional setting and field relationships. Nor. Geol. Unders. Bull. 405, 1–40.
Bennett, M.C., 1974. The emplacement of a high temperature peridotite in the Seiland province of the Norwegian Caledonides. J. Geol. Soc. 130, 205–226.
Berger, A., Stünitz, H., 1996. Deformation mechanisms and reaction of hornblende: examples from the Bergell tonalite (Central Alps). Tectonophysics 257, 149–174.
Bestmann, M., Prior, D.J., 2003. Intragranular dynamic recrystallization in naturally deformed calcite marble: diffusion accommodated grain boundary sliding as a result of subgrain rotation recrystallization. J. Struct. Geol. 25, 1597–1613.
Bingen, B., Demaiffe, D.O., 1998. The 616 Ma old egersund basaltic dike swarm, sw Norway, and late neoproterozoic opening of the Iapetus. Ocean 106, 565–574.
Blundell, D.J., Karnkowski, P.H., Alderton, D.H.M., Oszczepalski, S., Kucha, H., 2003. COPPER MINERALIZATION OF THE POLISH KUPFERSCHIEFER: A PROPOSED BASEMENT FAULT-FRACTURE SYSTEM OF FLUID FLOW, vol. 98, pp. 1487–1495.
Braeck, S., Podladchikov, Y.Y., 2007. Spontaneous thermal runaway as an ultimate failure mechanism of materials. Phys. Rev. Lett. 98.

Brune, S., Williams, S.E., Müller, R.D., 2018. Oblique rifting: the rule, not the exception. Solid Earth 9, 1187–1206.
Campbell, L.R., Menegon, L., Fagereng, Å., Pennacchioni, G., 2020. Earthquake nucleation in the lower crust by local stress amplification. Nat. Commun. 11.
Carter, N.L., Raleigh, C.B., Decarli, P.S., 1968. Deformation of olivine in stony meteorites. J. Geophys. Res. 73, 5439–5461.
Cawood, P.A., Mccausland, P.J., Dunning, G.R., 2001. Opening Iapetus: constraints from the laurentian margin in newfoundland. Geol. Soc. Am. Bull. 113, 443–453.
Connolly, J., 1990. Multivariable phase diagrams; an algorithm based on generalized thermodynamics. Am. J. Sci. 290, 666–718.
Czaplińska, D., Piazolo, S., Zibra, I., 2015. The influence of phase and grain size distribution on the dynamics of strain localization in polymineralic rocks. J. Struct. Geol. 72, 15–32.
Degli Alessandrini, G., Menegon, L., Malaspina, N., Dijkstra, A.H., Anderson, M.W., 2017. Creep of mafic dykes infiltrated by melt in the lower continental crust (Seiland Igneous Province, Norway). Lithos 274–275, 169–187.
Deseta, N., Andersen, T.B., Ashwal, L.D., 2014. A weakening mechanism for intermediate-depth seismicity? Detailed petrographic and microtextural observations from blueschist facies pseudotachylytes, Cape Corse, Corsica. Tectonophysics 610, 138–149.
Druiventak, A., Matysiak, A., Renner, J., Trepmann, C.A., 2012. Kick-and-cook experiments on peridotite: simulating coseismic deformation and post-seismic creep. Terra. Nova 24, 62–69.
Drury, M.R., Avé Lallemant, H.G., Pennock, G.M., Palasse, L.N., 2011. Crystal preferred orientation in peridotite ultramylonites deformed by grain size sensitive creep, Étang de Lers, Pyrenees, France. J. Struct. Geol. 33, 1776–1789.
Emblin, S.R., 1985. The Reinfjord Ultramafic Complex, Seiland Province: Emplacement History and Magma Chamber Model. University of Bristol.
Erdmann, S., Martel, C., Pichavant, M., Kushnir, A., 2014. Amphibole as an archivist of magmatic crystallization conditions: problems, potential, and implications for inferring magma storage prior to the paroxysmal 2010 eruption of Mount Merapi, Indonesia. Contrib. Mineral. Petrol. 167.
Ernst, R., Bleeker, W., 2010. Large igneous provinces (LIPs), giant dyke swarms, and mantle plumes: significance for breakup events within Canada and adjacent regions from 2.5 Ga to the Present. Can. J. Earth Sci. 47, 695–739.
Ernst, R., Buchan, K., 2004. Igneous Rock Associations in Canada 3. Large Igneous Provinces (LIPs) in Canada and Adjacent Regions: 3 Ga to Present, vol. 31. Geoscience Canada.
Ernst, R.E., Bell, K., 2010. Large Igneous Provinces (LIPs) and Carbonatites, vol. 98, pp. 55–76.
Ernst, R.E., Youbi, N., 2017. How Large Igneous Provinces affect global climate, sometimes cause mass extinctions, and represent natural markers in the geological record. Palaeogeogr. Palaeoclimatol. Palaeoecol. 478, 30–52.
Fetter, N., Blichert-Toft, J., Ludden, J., Lepland, A., Sánchez Borque, J., Greenhalgh, E., Garcia, B., Edwards, D., Télouk, P., Albarède, F., 2019. Lead isotopes as tracers of crude oil migration within deep crustal fluid systems. Earth Planet Sci. Lett. 525, 115747.
Finlay, A.J., Selby, D., Osborne, M.J., Finucane, D.J.G., 2010. Fault-charged Mantle-Fluid Contamination of United Kingdom North Sea Oils: Insights from Re-os Isotopes, vol. 38, pp. 979–982.
Franzolin, E., Schmidt, M., Poli, S., 2011. Ternary Ca–Fe–Mg carbonates: subsolidus phase relations at 3.5 GPa and a thermodynamic solid solution model including order/disorder. Contrib. Mineral. Petrol. 161, 213–227.
Gasser, D., Jerábek, P., Faber, C., Stünitz, H., Menegon, L., Corfu, F., Erambert, M., Whitehouse, M.J., 2015. Behaviour of Geochronometers and Timing of Metamorphic Reactions during Deformation at Lower Crustal Conditions: Phase Equilibrium Modelling and U-Pb Dating of Zircon, Monazite, Rutile and Titanite from the Kalak Nappe Complex, Northern Norway, vol. 33, pp. 513–534.
Gerlach, T.M., Mcgee, K.A., Elias, T., Sutton, A.J., Doukas, M.P., 2002. Carbon Dioxide Emission Rate of Kīlauea Volcano: Implications for Primary Magma and the Summit Reservoir, vol. 107, pp. 3–15. ECV 3-1-ECV.
Grant, T.B., Larsen, R.B., Anker-Rasch, L., Grannes, K.R., Iljina, M., Mcenroe, S., Nikolaisen, E., Schanche, M., Øen, E., 2016. Anatomy of a deep crustal volcanic conduit system; the Reinfjord ultramafic complex, Seiland igneous province, northern Norway. Lithos 252–253, 200–215.
Grant, T.B., Larsen, R.B., Brown, E.L., Müller, A.B., Mcenroe, S., 2020. Mixing of heterogeneous, high-MgO, plume-derived magmas at the base of the crust in the Central Iapetus Magmatic Province (Ma 610-550): origin of parental magmas to a global LIP event. Lithos 364–365, 105535.
Griffin, W.L., Sturt, B.A., O'neill, C.J., Kirkland, C.L., O'reilly, S.Y., 2013. Intrusion and contamination of high-temperature dunitic magma: the Nordre Bumandsfjord pluton, Seiland. Arctic Norway 165, 903–930.
Griggs, D., Baker, D., 1969. The Origin of Deep-Focus Earthquakes, Properties of Matter under Unusual Conditions. In: Mark, H., Fernbach, S. (Eds.). Wiley, New York, pp. 23–42.
Gumsley, A., Manby, G., Domańska-Siuda, J., Nejbert, K., Michalski, K., 2020. Caught between Two Continents: First Identification of the Ediacaran Central Iapetus Magmatic Province in Western Svalbard with Palaeogeographic Implications during Final Rodinia Breakup. Precambrian Research, 105622.
Hansen, L.N., Zimmerman, M.E., Dillman, A.M., Kohlstedt, D.L., 2012. Strain localization in olivine aggregates at high temperature: a laboratory comparison of constant-strain-rate and constant-stress boundary conditions. Earth Planet Sci. Lett. 333, 134–145.
Hansen, L.N., Zimmerman, M.E., Kohlstedt, D.L., 2011. Grain boundary sliding in San Carlos olivine: flow law parameters and crystallographic-preferred orientation. J. Geophys. Res. Solid Earth 116.
Hawemann, F., Mancktelow, N.S., Wex, S., Camacho, A., Pennacchioni, G., 2018. Pseudotachylyte as field evidence for lower-crustal earthquakes during the intracontinental Petermann Orogeny (Musgrave Block, Central Australia). Solid Earth 9, 629–648.
Hielscher, R., Silbermann, C.B., Schmidl, E., Ihlemann, J., 2019. Denoising of crystal orientation maps. J. Appl. Crystallogr. 52, 984–996.
Holland, T., Powell, R., 1996. Thermodynamics of order-disorder in minerals: II. Symmetric formalism applied to solid solutions. Am. Mineral. 81, 1425–1437.
Holland, T., Powell, R., 1998. An internally consistent thermodynamic data set for phases of petrological interest. J. Metamorph. Geol. 16, 309–343.
Holland, T., Powell, R., 2011. An improved and extended internally consistent thermodynamic dataset for phases of petrological interest, involving a new equation of state for solids. J. Metamorph. Geol. 29, 333–383.
Irwin, W.P., Barnes, I., 1980. Tectonic Relations of Carbon Dioxide Discharges and Earthquakes, vol. 85, p. 3115.
Ismail, W.B., Mainprice, D., 1998. An olivine fabric database: an overview of upper mantle fabrics and seismic anisotropy. Tectonophysics 296, 145–157.
Jamtveit, B., Ben-Zion, Y., Renard, F., Austrheim, H., 2018. Earthquake-induced transformation of the lower crust. Nature 556, 487–491.
John, T., Medvedev, S., Rüpke, L.H., Andersen, T.B., Podladchikov, Y.Y., Austrheim, H., 2009. Generation of intermediate-depth earthquakes by self-localizing thermal runaway. Nat. Geosci. 2, 137–140.
Kamo, S.L., Gower, C.F., Krogh, T.E., 1989. Birthdate for the Iapetus Ocean? A precise U-Pb zircon and baddeleyite age for the Long Range dikes, southeast Labrador. Geology 17, 602–605.
Kelemen, P.B., Hirth, G., 2007. A periodic shear-heating mechanism for intermediate-depth earthquakes in the mantle. Nature 446, 787–790.
Kirkpatrick, J.D., Rowe, C.D., 2013. Disappearing ink: how pseudotachylytes are lost from the rock record. J. Struct. Geol. 52, 183–198.
Krill, A.G., Zwaan, K., 1987. Reinterpretation of Finnmarkian deformation on western Sørøy, northern Norway. Nor. Geol. Tidsskr. 67, 15–24.
La Rosa, A., Keir, D., Doubre, C., Sani, F., Corti, G., Leroy, S., Ayele, A., Pagli, C., 2021. Lower crustal earthquakes in the March 2018 sequence along the western margin of Afar. G-cubed 22.
Larsen, R.B., Grant, T., Sørensen, B.E., Tegner, C., Mcenroe, S., Pastore, Z., Fichler, C., Nikolaisen, E., Grannes, K.R., Church, N., Ter Maat, G.W., Michels, A., 2018. Portrait of a giant deep-seated magmatic conduit system: the Seiland Igneous Province. Lithos 296–299, 600–622.
Lee, A.L., Lloyd, G.E., Torvela, T., Walker, A.M., 2020. Evolution of a shear zone before, during and after melting. J. Geol. Soc.
Lee, H., Muirhead, J.D., Fischer, T.P., Ebinger, C.J., Kattenhorn, S.A., Sharp, Z.D., Kianji, G., 2016. Massive and prolonged deep carbon emissions associated with continental rifting. Nat. Geosci. 9, 145–149.
Linckens, J., Herwegh, M., Müntener, O., Mercolli, I., 2011. Evolution of a Polymineralic Mantle Shear Zone and the Role of Second Phases in the Localization of Deformation, vol. 116.
Lopez-Sanchez, M.A., Tommasi, A., Ismail, W.B., Barou, F., 2021. Dynamic recrystallization by subgrain rotation in olivine revealed by electron backscatter diffraction. Tectonophysics, 228916.
Matysiak, A.K., Trepmann, C.A., 2012. Crystal–plastic deformation and recrystallization of peridotite controlled by the seismic cycle. Tectonophysics 530–531, 111–127.
Matysiak, A.K., Trepmann, C.A., 2015. The deformation record of olivine in mylonitic peridotites from the Finero Complex, Ivrea Zone: separate deformation cycles during exhumation. Tectonics 34, 2514–2533.
Mckenzie, D., 1978. Some remarks on the development of sedimentary basins. Earth Planet Sci. Lett. 40, 25–32.
Mckenzie, D., Brune, J.N., 1972. Melting on fault planes during large earthquakes. Geophys. J. Int. 29, 65–78.
Mehl, L., Hirth, G., 2008. Plagioclase preferred orientation in layered mylonites: evaluation of flow laws for the lower crust. J. Geophys. Res. 113.
Menegon, L., Nasipuri, P., Stünitz, H., Behrens, H., Ravna, E., 2011. Dry and Strong Quartz during Deformation of the Lower Crust in the Presence of Melt, vol. 116.
Molina, J.F., Moreno, J.A., Castro, A., Rodríguez, C., Fershtater, G.B., 2015. Calcic amphibole thermobarometry in metamorphic and igneous rocks: new calibrations based on plagioclase/amphibole Al-Si partitioning and amphibole/liquid Mg partitioning. Lithos 232, 286–305.
Orvik, A.A., 2019. Gangsvermen i det Reinfjord Ultramafiske Kompleks: Et vindu inn til de terminale stadiene som formet den Magmatiske Provinsen i Seiland. NTNU.
Pan, V., Holloway, J.R., Hervig, R.L., 1991. The Pressure and Temperature Dependence of Carbon Dioxide Solubility in Tholeiitic Basalt Melts, vol. 55, pp. 1587–1595.
Papa, S., Pennacchioni, G., Menegon, L., Thielmann, M., 2020. High-stress creep preceding coseismic rupturing in amphibolite-facies ultramylonites. Earth Planet Sci. Lett. 541, 116260.
Park, M., Jung, H., 2020. Analysis of electron backscattered diffraction (EBSD) mapping of geological materials: precautions for reliably collecting and interpreting data on petro-fabric and seismic anisotropy. Geosci. J.
Pastore, Z., Fichler, C., Mcenroe, S.A., 2016. The deep crustal structure of the mafic–ultramafic Seiland Igneous Province of Norway from 3-D gravity modelling and geological implications. Geophys. J. Int. 207, 1653–1666.
Petley-Ragan, A., Ben-Zion, Y., Austrheim, H., Ildefonse, B., Renard, F., Jamtveit, B., 2019. Dynamic earthquake rupture in the lower crust. Sci. Adv. 5, eaaw0913.
Pili, E., Sheppard, S.M.F., Lardeaux, J.-M., 1999. Fluid-Rock Interaction in the Granulites of Madagascar and Lithospheric-Scale Transfer of Fluids, vol. 2, pp. 341–350.
Platt, J.P., 2015. Influence of shear heating on microstructurally defined plate boundary shear zones. J. Struct. Geol. 79, 80–89.

Pu, J.P., Bowring, S.A., Ramezani, J., Myrow, P., Raub, T.D., Landing, E., Mills, A., Hodgin, E., Macdonald, F.A., 2016. Dodging snowballs: geochronology of the Gaskiers glaciation and the first appearance of the Ediacaran biota. Geology 44, 955–958.
Reginiussen, H., Ravna, E.K., Berglund, K., 1995. Mafic dykes from Øksfjord, Seiland Igneous Province, northern Norway: geochemistry and palaeotectonic significance. Geol. Mag. 132, 667–681.
Ridolfi, F., Renzulli, A., 2012. Calcic amphiboles in calc-alkaline and alkaline magmas: thermobarometric and chemometric empirical equations valid up to 1,130°C and 2.2 GPa. Contrib. Mineral. Petrol. 163, 877–895.
Ridolfi, F., Renzulli, A., Puerini, M., 2010. Stability and chemical equilibrium of amphibole in calc-alkaline magmas: an overview, new thermobarometric formulations and application to subduction-related volcanoes. Contrib. Mineral. Petrol. 160, 45–66.
Roberts, R., Corfu, F., Torsvik, T., Hetherington, C., Ashwal, L., 2010. Age of alkaline rocks in the Seiland igneous province, northern Norway. J. Geol. Soc. 167, 71–81.
Roberts, R.J., 2007. The Seiland Igneous Province, Northern Norway: Age, Provenance, and Tectonic Significance.
Roberts, R.J., Corfu, F., Torsvik, T.H., Ashwal, L.D., Ramsay, D.M., 2006. Short-lived mafic magmatism at. 560–570 Ma in the northern Norwegian Caledonides: U–Pb zircon ages from the Seiland Igneous Province 143, 887.
Roecker, S., Ebinger, C., Tiberi, C., Mulibo, G., Ferdinand-Wambura, R., Mtelela, K., Kianji, G., Muzuka, A., Gautier, S., Albaric, J., 2017. Subsurface images of the Eastern Rift, Africa, from the joint inversion of body waves, surface waves and gravity: investigating the role of fluids in early-stage continental rifting. Geophys. J. Int. 210, 931–950.
Rovetta, M.R., Delaney, J.R., Blacic, J.D., 1986. A Record of High-Temperature Embrittlement of Peridotite in CO 2 Permeated Xenoliths from Basalt, vol. 91, p. 3841.
Ruzicka, A.M., Hugo, R.C., 2018. Electron backscatter diffraction (EBSD) study of seven heavily metamorphosed chondrites: deformation systematics and variations in pre-shock temperature and post-shock annealing. Geochem. Cosmochim. Acta 234, 115–147.
Schmidt Mumm, A., Wolfgramm, M., 2004. Fluid Systems and Mineralization in the North German and Polish Basin, vol. 4, pp. 315–328.
Sibson, R.H., 1980. Transient discontinuities in ductile shear zones. J. Struct. Geol. 2, 165–171.
Sørensen, B., Hjelen, J., Ånes, H., Breivik, T., 2020. Recent features in EBSD, including new trapezoidal correction for multi-mapping. In: IOP Conference Series: Materials Science and Engineering. IOP Publishing, 012021.
Sørensen, B.E., Grant, T., Ryan, E.J., Larsen, R.B., 2019. In situ evidence of earthquakes near the crust mantle boundary initiated by mantle CO2 fluxing and reaction-driven strain softening. Earth Planet Sci. Lett. 524, 115713.
Tappe, S., Romer, R.L., Stracke, A., Steenfelt, A., Smart, K.A., Muehlenbachs, K., Torsvik, T.H., 2017. Sources and mobility of carbonate melts beneath cratons, with implications for deep carbon cycling, metasomatism and rift initiation. Earth Planet Sci. Lett. 466, 152–167.
Thielmann, M., 2018. Grain size assisted thermal runaway as a nucleation mechanism for continental mantle earthquakes: impact of complex rheologies. Tectonophysics 746, 611–623.
Toy, V.G., Newman, J., Lamb, W., Tikoff, B., 2010. The role of pyroxenites in formation of shear instabilities in the mantle: evidence from an ultramafic ultramylonite, twin sisters Massif, Washington. J. Petrol. 51, 55–80.
Warren, J.M., Hirth, G., 2006. Grain size sensitive deformation mechanisms in naturally deformed peridotites. Earth Planet Sci. Lett. 248, 438–450.
Weinstein, A., Oliva, S.J., Ebinger, C.J., Roecker, S., Tiberi, C., Aman, M., Lambert, C., Witkin, E., Albaric, J., Gautier, S., Peyrat, S., Muirhead, J.D., Muzuka, A.N.N., Mulibo, G., Kianji, G., Ferdinand-Wambura, R., Msabi, M., Rodzianko, A., Hadfield, R., Illsley-Kemp, F., Fischer, T.P., 2017. Fault-magma interactions during early continental rifting: seismicity of the Magadi-Natron-Manyara basins. Africa 18, 3662–3686.
Wilshire, H.G., Kirby, S.H., 1989. Dikes, Joints, and Faults in the Upper Mantle, vol. 161, pp. 23–31.
Wyllie, P.J., Huang, W.L., Otto, J., Byrnes, A.P., 1983. Carbonation of peridotites and decarbonation of siliceous dolomites represented in the system CaO-MgO-SiO2-CO2 to 30 kbar. Tectonophysics 100, 359–388.
Youbi, N., Ernst, R.E., Söderlund, U., Boumehdi, M.A., Lahna, A.A., Tassinari, C.C.G., El Moume, W., Bensalah, M.K., 2020. The Central Iapetus Magmatic Province: an Updated Review and Link with the Ca. 580 Ma Gaskiers Glaciation. Mass Extinctions, Volcanism, and Impacts: New Developments. Geological Society of America Boulder.
Zhang, S., Karato, S.-I., 1995. Lattice preferred orientation of olivine aggregates deformed in simple shear. Nature 375, 774–777.
Zhong, X., Petley-Ragan, A.J., Incel, S.H., Dabrowski, M., Andersen, N.H., Jamtveit, B., 2021. Lower crustal earthquake associated with highly pressurized frictional melts. Nat. Geosci. 1–7.
Ziegler, P.A., 1992. Geodynamics of Rifting and Implications for Hydrocarbon Habitat, vol. 215, pp. 221–253.
Zwaan, F., Schreurs, G., 2020. Rift segment interaction in orthogonal and rotational extension experiments: implications for the large-scale development of rift systems. J. Struct. Geol. 140, 104119.

8 Fault-linkage on Southeastern Bjørnøya: Implications for structural interpretations surrounding fertile ore-forming fault systems in the offshore domain

Title

Fault linkage on southeastern Bjørnøya: Implications for structural interpretations surrounding fertile ore-forming fault systems offshore

Eric J. Ryan[a*], Bjørn E. Sørensen[a], Christine Fichler[a], Rune B. Larsen[a,] Julie L. Gresseth[a], Arne Bjørlykke[b]

[a]Department of Geoscience and Petroleum, Norwegian University of Science and Technology, S.P. Andersens veg 15a, 7031 Trondheim, Norway

[b]Geological Survey of Norway, N–7491 Trondheim, Norway.

[a*]eric.j.ryan@ntnu.no

[*]Corresponding author

Abstract

Exploration for mineral resources offshore requires a detailed understanding and assessment of similar onshore mineral systems. The island of Bjørnøya in the Barents Sea presents a unique opportunity to investigate structurally controlled sulfide-bearing (Pb + Zn + Cu + Au) mineral systems in a tectonic and lithological setting relevant for surrounding subsea domain. We applied geophysical methods including the interpretation of magnetic and gravity data, field mapping, photogrammetry, and stress-tensor analyses to describe the structural setting and estimate the relative timing of structural and ore-forming events. We show that fault linkage between N–S-striking normal faults and NW–SE-striking oblique-slip transtensional faults provided fluid pathways for mineralizing fluids in the mid- to late Paleozoic, probably during the Carboniferous, leading to widespread structurally controlled vein mineralization of sphalerite and galena on southeastern Bjørnøya. Migration of the ore-forming fluids on Bjørnøya depended on movement along active faults causing seismic pumping, while the ore precipitated following the reduction of sulfate to sulfide by hydrocarbons or hydrogen gas. The characteristic structural setting of mineralizations and ore deposits on Bjørnøya may act as an analog model in the search for primary targets of fluid pathways with potential for mineral resources offshore.

Introduction

Owing to its potential for mineral and hydrocarbon resources and carbon storage, the Barents Sea has piqued the interest of geologists for over 100 years (Smelror et al., 2009). Early geologists (Andersson, 1901, Holtedahl, 1920, Horn and Orvin, 1928) explored Bjørnøya in the southwestern Barents Sea at the turn of the 20th century describing the stratigraphy, providing early tectonic assessments and documenting coal and other mineral resources. As the exploitation of arctic mineral resources tapered off, hydrocarbon exploration guided the geological focus in the region, particularly from the mid-1970s and onwards (Smelror et al., 2009). Seminal works based on regional seismic interpretation (Faleide et al., 1984, Gudlaugsson et al., 1998) and aeromagnetic data (Åm, 1975) began to unravel the crustal and basinal geometries of the western Barents Sea. Later, studies based on potential field data (e.g. Rønning and Skilbrei (1998), Olesen et al. (2010), Ritzmann and Faleide (2007), Ebbing et al. (2007), Barrère et al. (2011), Marello et al. (2013), Gernigon et al. (2014) and Fichler and Pastore (2022)) provided further insight into crustal configurations and compositions resulting from orogenic build up and late–post-orogenic Caledonian collapse, followed by episodes with rifting, uplift, and erosion (cf. Smelror et al. (2009)). Despite this solid foundation regarding crustal and tectonic development, much remains unconstrained, particularly concerning the genesis of mineral resources in the Barents Sea.

A wide variety of available data from geological mapping, LiDAR, well core, potential field, and seismic surveys allow geoscientists to apply inter-disciplinary techniques for solving complex geological problems. Recent studies combining new or reprocessed seismic data (i.e. Blaich et al. (2017), Gresseth et al. (2021)), combined with potential field data (Fichler and Pastore, 2022) and finally detailed field analyses on Bjørnøya (Braathen et al., 1999) and Spitsbergen (Braathen et al., 2018) have made significant inroads in our understanding of the deep structures and Paleozoic evolution of the Barents Sea.

These same tools may help extrapolate land-based knowledge of mineral resources offshore, though such a process is not without significant challenges. Compared to petroleum reserves extracted from similar geological settings, which extend for 10's or even 100's of square kilometers, such as the Ghawar oil field in Saudi Arabia (Afifi, 2005), mineral deposits are comparatively miniscule, generally confined to areas on the order of 100's of meters. Even the massive baryte and Zn + Pb + Ag deposits in the Red Dog district in Alaska cover only 0.003% of the area of Ghawar, based on estimates by Kelley and Jennings (2004). The smaller size of mineral deposits, combined with the attenuation of signals and long wavelengths necessary to penetrate both deep seas and thick sedimentary packages common offshore (Landrø and Amundsen, 2018), limits the usefulness of traditional, industry geophysical methods. By identifying key onshore structural settings, including major faults and linear trends, which are identifiable potential field and seismic surveys, we may identify prospective offshore ore areas.

The reactivation of crustal-scale detachments has a significant effect on upper crustal tectonic evolution and basinal development (e.g., Whitney et al. (2013), Osmundsen and Péron-Pinvidic (2018), Serck and Braathen (2019), Naliboff et al. (2020)). Fault linkage, as described by Fossen and Rotevatn (2016), plays a key role in localizing strain and fluid migration in extensional settings. As faults develop and encroach one another's sphere of influence, their stress fields interact. This leads to the development of misoriented structures between the original faults, and a potential for hard linkage where the fault network develops to such an extent that the faults are physically connected. The formation of intersection structures with variable orientations also improves permeability through the creation of new fluid pathways and a significant potential for nonsealing structures. As such, fault linkage settings are often associated with hydrothermal ore deposits and migration pathways for hydrocarbons (Fossen and Rotevatn, 2016). A combination of structural reactivation, fault linkage, and increased fluid migration through seismic pumping (Sibson et al., 1975, Sibson, 2000) may create favorable conditions for ore deposits, while a thorough understanding of these processes is also for hydrocarbon and/or carbon capture systems. Normal faults, in particular, but also oblique-slip faults are associated with increased fluid migration (Muir-Wood and King, 1993) and were suggested to have played an important role in Pb-Zn deposits elsewhere in Scandinavia (Bjørlykke et al., 2021). Our study shows how geophysical, geological, and topographical datasets can be integrated to better constrain the structural development and the geology of Bjørnøya and the surrounding offshore areas of Stappen High, particularly regarding the role of basement structures, fault linkage, fluid migration, and ore formation.

Geological Background

Barents Sea

The Barents Sea stretches from the northern coast of Norway in the South and to Svalbard in the North (70 – 82° N) (Fig. 1). The western boundary is delineated by the continent–ocean boundary to the Greenland Sea in the North and the Norwegian Sea in the South. Towards the east, Novaya Zemlya separates the Barents Sea from the Kara Sea. The evolution of the southwest Barents Sea is intimately linked to basement structures (i.e., thrusts, suture zones) formed prior to, during and following the Caledonian orogeny (Ritzmann and Faleide, 2007, Gernigon et al., 2014, Gresseth et al., 2021).

Early basement development

Early orogenies, including the Timanian, Caledonian, and Uralian played a role in the development of the Barents Sea (Roberts and Olovyanishnikov, 2004, Gernigon and Brönner, 2012, Koehl et al., 2022). From

650 – 550 Ma, the Timanian orogeny is suggested to have resulted in a hundreds to thousands of kilometer long and several kilometer thick NNE-dipping fold and thrust system, stretching from Russia to Northern Norway and the Northern Barents Sea, leading to the accretion of the Barents Sea region onto present-day Norway (Koehl et al., 2022). These structures may have played an important role in the localization of later deformation events, including the N-S-trending Caledonian orogeny (Koehl et al., 2022). The basement beneath the southwest Barents Sea experienced significant contraction during Caledonian orogeny following the collision between Laurentia and Baltica, with major thrusts and fold belts (Ritzmann and Faleide, 2007, Gernigon et al., 2014, Faleide et al., 2018, Braathen et al., 1999), resulting in complex tectonic intra-basement rheological and structural heterogeneities. Carbonate rocks from extensive Laurentian marginal platforms (Gee et al., 2008) are elsewhere associated with numerous Pb – Zn deposits (Taylor et al., 2009). In Eastern Greenland, Pb and Zn deposits are well documented in Carboniferous – Permian rocks, in vein deposits associated with large fault zones (Pedersen and Stendal, 2000).

Some of the structures observed onshore in Northern Norway and on Svalbard can be correlated to basement structures in the southwest Barents Sea (Ritzmann and Faleide, 2007), such as Kongsfjorden–Cowanodden fault zone (Koehl et al., 2022). The precise nature of these structures remains poorly understood (Braathen et al., 2018), though recent works have shed light on the orientation and influence of specific Caledonian structures (Gresseth et al., 2021, Koehl et al., 2022). The array of thrusts and sutures across the Barents Sea exerted a significant control on the development of the rift basins and structural highs during and after the Timanian and Caledonian orogeny (Braathen et al., 1999, Ritzmann and Faleide, 2007, Gernigon et al., 2014, Faleide et al., 2018, Shulgin et al., 2020, Gresseth et al., 2021, Koehl et al., 2022).

Rift basin evolution

The rift basins and structural highs formed through a series of rifting episodes throughout the Mesozoic, following the orogenic collapse of the Caledonides from the Devonian through the Carboniferous (Gernigon et al., 2014), and ending with oceanic breakup in the Cenozoic (Faleide et al. 2008). Initially, widespread exhumation and corresponding erosion effected the hinterland (Gernigon et al., 2014). During rifting, thick sedimentary units were deposited upon the shelf, now recognized as platform deposits above rift-related structures (Gudlaugsson et al., 1998). Wide-spread rifting and the deposition of sedimentary packages continued across the Barents Sea until the Cenozoic, successively towards the west, leaving the oldest, late Paleozoic rift basins in the east (Faleide et al., 2008). During the Paleocene – Eocene transition, the geological evolution of the Barents Sea culminated with the opening of the Norwegian

Greenland Sea and continental separation, establishing the Vestbakken Volcanic Province serving as the continental scarp west of the Caledonian suture zone (Faleide et al., 1996, Gernigon et al., 2019).

The Stappen High and Bjørnøya

The rock record on Bjørnøya (Lepvrier et al., 1989, Braathen et al., 1999, Worsley et al., 2001) and the Stappen High (Blaich et al., 2017) reflects the tectonic evolution of the southwest Barents Sea (Koehl et al., 2022). The Stappen High is bound by the deep Bjørnøya Basin to the south and southeast, the Leirdjupet Fault Complex and Fingerdjupet subbasin to the East and the Sørkapp Basin to the Northeast (Fig. 1A). The western margin of the Stappen High borders the Knølegga Fault Zone and the Vestbakken Volcanic Province, with the continent–ocean boundary further west of these (Blaich et al., 2017, Dumais et al., 2020). Bjørnøya lies near the center of the Stappen High, with exposed rocks within Caledonian nappes in a 25 km^2 area at the southeastern tip of the island, including the Neoproterozoic Russehamna , Sørhamna and Ymerdalen Formations. This is overlain by the Billefjorden, Templefjorden, and Sassendalen groups and Skuld Formation.

On Bjørnøya, Caledonian thrusts and folds indicate a WNW transport direction and are suggested to have formed between the Middle Ordovician and Late Devonian based on the age of the overlying sedimentary strata (Braathen et al., 1999). The thrusts cut the stratigraphy in southeastern Bjørnøya, where the Ediacaran Russehamna Formation is thrust onto the Early Ordovician Sørhamna Formation, which is in turn thrust onto the Middle Ordovician Ymerdalen Formation. The structures were later reactivated during the Paleozoic, with an eastwards to east-southeastwards transport direction, indicating the importance of Caledonian structural grain for later deformation on Bjørnøya, and in the Barents Sea (Lepvrier et al., 1989, Braathen et al., 1999, Blaich et al., 2017). Lepvrier et al. (1989) further divided the Late Paleozoic structural evolution of Bjørnøya into three phases, including the aforementioned E–W extensional phase during the early to middle Carboniferous, followed by an Upper Carboniferous ENE – WSW contractional phase which the authors relate to basinal inversion, and finally a NNW–SSE dextral transtensional phase, followed by the reactivation of the NS-striking extensional faults in the early Permian. Worsley et al. (2001) described a comparable situation with significant faulting on Bjørnøya, reworking the Røedvika, Nordkapp Landnørdingsvika and Kapp Kåre Formations from the Famennian through Moscovian times.

Methods

In addition to a detailed field mapping and sampling campaign we used a variety of methods to investigate the structural evolution of southeastern Bjørnøya and constrain structures associated with the Pb–Zn mineralizations. Sample coordinates as well as the coordinates of field images included in this study are available in the electronic appendix.

Gravity and magnetic data and methods

For grid display, filtering, processing, and survey merging we used both Seequent Geosoft Oasis Montaj™ and Encom ModelVision™. The 2D magnetic profile modelling was performed in Encom ModelVision™, which computes magnetic anomalies under the assumption that the modeled bodies displayed on the profile strike in a vertical angle off the section in the map plane. The regional datasets include gravity and magnetic data. We compiled the gravity data from two datasets (Fig. 2A, B) including both satellite and marine free-air gravity data in the offshore areas and Bouguer gravity data (correction density = 2.67 g/cm^3) on land. Grid cell size was chosen to 2 x 2 km. The magnetic data (total magnetic intensity: TMI) were compiled from five datasets (Fig. 2C, D) and the grid cell size was chosen to 500 x 500 m. We applied filters to the gravity and magnetic data, including the tilt derivative filter (Dentith and Mudge, 2014), enhancing the short wavelength anomalies, and upward continuation filter (Hinze et al., 2013), lowering the noise level on the calculated tilt derivatives. The modelled profile is a part of line T5090 from the BASAR 09 aeromagnetic survey (Fig. 3). The profile spans nearly 6 kilometers with an ENE–WSW strike direction and extends to 500 meters below sea level. The local geomagnetic field has a total intensity of 54363 nT, with an 80.7° inclination and 11.3° declination at acquisition time. The topography in the model was based on Norwegian Polar Institute data, and the sensor height was taken from the BASAR 09 dataset. We removed the regional magnetic background with an offset equal to -70 nT. The base magnetometer on Bjørnøya measured a variation of the earth magnetic field that is within +/- 0.5 nT during the acquisition of this profile, documenting a high quality of the acquired magnetic data. The 20 samples collected during the field campaign included carbonate rocks and mineralized veins, all with magnetic susceptibilities lower than 1.57 x 10^{-5} SI measured with a handhold susceptibility meter.

Lineament Analysis

The large-scale structural fabric of Bjørnøya is reflected by the numerous lineaments we observe in the digital elevation model (DEM) which we have used as the map background (Fig. 4). We performed a lineament analysis (Fig. 5) for southeastern Bjørnøya by manually tracing lineaments at 1:100000 and 1:20000 scales as well as lineaments in the tilt derivative 100 m upward continuation in from Fig. 3C. The DEM was downloaded from the Norwegian Polar Institute and has a 2 x 2 m resolution. To remove

any bias caused by hillshade lighting orientation, we filtered the DEM using the standard deviation of elevation via an ArcGIS toolbox. Rose diagrams, created using Stereonet by Allmendinger et al. (2011) and Cardozo and Allmendinger (2013), were used to compare the trend of the measured lineations with data collected in the field, including faults (Fig. 6A and B) and hydrothermal veins (Fig. 6E, F & Fig 7A, B).

Photogrammetry

We created 3D outcrop models using the ContextCapture suite of software. The 3D model of the pervasively veined islet outcrop (Fig. 8) was created using georeferenced photographs from a DJI Phantom IV Pro drone, allowing us to quantitatively analyze the orientation of individual veins. We used the LIME software (Buckley et al., 2019) to model the orientation of the various planar veins and fracture planes (Fig. 9C). The orientation data were later exported to Win-Tensor V. 5.9.2 (Delvaux, 2012) where we further analyzed the orientation of stress tensors.

Stress tensor Analysis

Using Win-Tensor V. 5.9.2 (Delvaux, 2012) we performed stress tensor analyses for carbonate veins, baryte veins, and all the veins from a 3D outcrop model (Fig. 9). Lineations were exceptionally rare in the field and few precise measurements of the transport directions along faults were made. As such, the data were entered as type 4 (plane alone), type T (tensile fracture), with supposed (S) confidence levels. During data processing we used the Right Dihedron Method for all the datasets before continuing with the Rotational Optimization Methods (Delvaux and Sperner, 2003). This provided principal stress axes for the various data sets which we compare to the orientation and transport direction along larger, locally coeval faults.

Results

The following section describes the results of our geophysical, field, and laboratory analyses.

Gravity and magnetic field data from the Barents Sea, Stappen High, and Bjørnøya

Regional magnetic and gravity surveys reveal the large-scale structural fabric of the Barents Sea region and the Stappen High (Fig. 2). The regional Bouguer gravity map and its filtered map show similar trends, with a 300-kilometer-long NNE–SSW-trending gravity lineament to the north and west of Bjørnøya (Fig. 2A, B), bound to the west by a 70 mGal high and to the east by a low, reaching -30 mGal at its northern extent (Fig. 2A). A weaker, 200-kilometer-long NNE–SSW-trending gravity low is apparent to the east of Bjørnøya, with a low of around 25 mGal bound wo the West and Esat by over 60

mGal highs. The position of Bjørnøya near the edg of a significant gravity high is apparent in both Fig. 2A and B, which reaches nearly 70 mGal to the west of Bjørnøya (Fig. 2A).

The magnetic compilation in Fig. 2C shows prominent linear features which are enhanced by tilt derivative filtering in Fig. 2D. The area immediately to the northeast of Bjørnøya is characterized by multiple NNW–SSE-trending lineaments (Fig. 2D), which extend for 200 kilometers parallel to the strike of the Hornsund Fracture Zone (HSZ) (Ritzmann and Faleide, 2007). Immediately to the east of Bjørnøya, these lineaments show a near N–S trend and separate Bjørnøya from the eastern Stappen High and Fingerdjupet Subbasin. As in the gravity maps, Bjørnøya is positioned near significant anomalies, with a 375 nT high immediately to the southwest of Bjørnøya in Fig. 2C and a NNE–SSE-trending lineament to the east of Bjørnøya in Fig. 2D.

Magnetic profile and model from southeastern Bjørnøya

The BASAR 09 aerial magnetic survey (Brönner et al., 2010) covers significant portions of the Western Barents Sea, including multiple flight lines which intersect the mineralized area (Fig. 3A). Three maps of Bjørnøya, showing the unfiltered magnetic anomalies (Fig. 3A), removal of the 3rd degree polynomial residual (Fig. 3B) and a tilt derivative filter with a 100m upward continuation (Fig. 3C) help demonstrate the relation between the magnetic anomalies and physical geology (Fig. 3D & Fig. 4). One flight line (T5090, Fig. 3), cuts diagonally across the central field area, providing an opportunity to model the structure of the mineralizing system at depth.

We observe a correlation between three magnetic lows and map-scale normal faults (Fig. 3D). The two eastern most normal faults lie in figure 3 near the mineralized veins and the Blyhatten Pb–Zn mine, while the westernmost magnetic low lies in conjunction with a linear structure in the DEM, which was not investigated in our field study. The normal fault which cuts across the most heavily mineralized area in figure 3 does not show a significant response on the magnetic profile. There is also a correlation between the sensor elevation and magnetic response, though this is to be expected when the magnetic lows correspond to topographic highs during an aerial survey. Some of the normal faults probably reactivate Caledonian thrusts.

The crystalline crust bodies (red color) were found to be most suitably modelled by a magnetic susceptibility of 0.002 SI. This reflects the susceptibility of common crystalline basement rocks, where felsic rocks (e.g., granite) or low-grade metamorphic rocks (e.g., metasediments or greenstones) constitute possible alternative interpretations (Clark, 1997). All outcropping units were set to a magnetic susceptibility of 0 SI, in accordance with our samples. The modelled profile (Fig. 3D) provides a simplified interpretation of the deep structure beneath the Blyhatten deposit and the mineralized veins.

Analysis of topographical and cartographic data

The basement of southeastern Bjørnøya is characterized by folded metasedimentary rocks and both normal and transtensional faults with multiple orientations, locally exploiting Caledonian thrusts. The faults are adjacent to prevalent hydrothermal veining and brecciation associated with the Pb–Zn sulfide mineralizations. We collected foliation, fault, fracture, and fold measurements across the study area. The undulatory orientation of bedding planes (Fig. 4) depicts the folded nature of the Hecla Hoek. Large-scale folds (Fig. 4) difficult to observe in the field have axial planes striking approximately N–S and dipping steeply towards the E, while most of the bedding dips slightly (ca. 10 deg) to the east. NW–SE-striking transtensional faults cut N–S-striking normal faults (Fig. 4). The largest of these faults strike WNW–ESE and exert significant control on present day topography. The earliest normal faults follow the same N–S strike as both the thrusts and axial trace of the large-scale folds. These faults are difficult to trace laterally in the field due to significant sedimentary cover, but where identified, locally correlate with Pb–Zn mineralizations. The N–S-striking fault traces are also evident in the DEM map, forming horst and graben structures outlining the present-day topography (Fig. 4).

The lineament analysis performed on LiDAR and filtered magnetic data reveals distinct linear trends (Fig. 5) in the surface structure. The standard deviation of elevation LiDAR data with 100 x 100 m (Fig. 5A) and 25 x 25 m (Fig. 5B) grids reveal two similar trends, with predominately NW–SE and N–S orientations. The 100 m grid revealed a higher frequency of N–S trends than the 25 m grid, which may indicate that the N–S-striking structures typically have a larger scale, in accordance with our field observations. The N–S-trending surfaces correlate to the N–S-striking thrusts and normal faults, while the NW–SE-trending lineations correlate to the transtensional structures. The strong NW–SE trend is still visible in the filtered magnetic data (Fig. 5C), though no longer represents a dominant orientation. The magnetic data also shows a minor E–W trending component, potentially related to mineralized veins.

Analysis of field structures

The NW–SE-striking transtensional faults cut the entirety of the Hecla Hoek and form well defined features in the field (Fig. 6A, B). We observed numerous, smaller (5–20 cm thick) subsidiary faults with steep dips and predominately E–W and NE–SW strikes. Outcrop coverage is sparse inland, with the best non-coastal outcrops surrounding the open pit Blyhatten Pb–Zn mine and the erosional bluffs created by the Russeelva river. The faults are traceable for hundreds of meters. Other common structures include small-scale faults, often associated with baryte and/or calcite veins (Fig. 6D). Most of these faults dip steeply to the SSE, though a significant variation in structural orientation exists among the smaller (1-4

cm thick) structures. Locally, the mineralized veins associated with the faults display clear examples of hydrothermal brecciation (Fig. 6E), while others are distinctly zoned (Fig. 6F). The hydrothermal breccia in Fig. 6E contains angular clasts of dolomitic host rock and mineralized material, with significant amounts of red sphalerite and trace amounts of galena. The matrix consists mostly of baryte, with minor quartz and carbonate. Fig. 6G shows a thin section from this hydrothermal breccia where clasts of sphalerite (4 mm diameter) are visible in the matrix of carbonate host rock, baryte, and quartz.

Much of the Hecla Hoek is characterized by gentle, open folding, typically with N–S-trending fold axes and approximately vertical axial planes. Folds vary from decimeter to meter-scale wavelengths (Fig. 6C), in addition to the larger scale folds included in the geological map (Fig. 4). Folding near and within major tectonic contacts indicates transport directions between units. In the shale between the Russehamna and Sørhamna Formations in Kvalrossbukta, decimeter-scale, tight to isoclinal folds hinges plunge to the SW (215°/10°). Their axial planes define a pervasive cleavage dipping moderately towards the SE (30°/130°) indicating a NW transport direction following the vergence of the folds. The axial planar cleavage is oblique to the bedding, which dips steeply to the NW (50°/310°).

Elsewhere, fault-related baryte veins are visible along the coast within the Russehamna and Sørhamna Formations (Fig. 7). The veins cut the topographic thickness of the coastal cliffs, spanning from sea-level to over 50 meters in elevation. Unfortunately, due to inclement weather and a high sea state these veins remained inaccessible during our field campaign. The veins shown in Fig. 7A, B are both in the immediate vicinity of potential major faults.

The outcrop of the Russehamna islet (Fig. 8) shows a particularly well-preserved array of veins, kept clean due to constant wave action. More than 100 veins cut across the islet, located between two separate branches of the large WSW–ESE transtensional fault cutting Russehamna (Fig. 8E), based on the position of the islet between two significant linear structures in the field (Fig. 4). In the 3D model we observe multiple examples of conjugate veins, with the largest veins striking approximately E–W, with subvertical dips, and a smaller conjugate set of veins striking WNW–ESE, subparallel to the large normal faults. Tensile fractures separate the veins, indicating the direction of principal stress components during hydrothermal activity.

Stress tensor analysis

Most fractures in southeastern Bjørnøya show no significant displacement. The low-grade rocks crosscut by the faults rarely show any lineations and the precise direction of displacement remains uncertain. The orientation data provided by the islet planes gathered from the 3D model show a distinct pattern, consistent with the baryte and calcite veins. Despite sparse kinematic information, WinTensor (Delvaux,

2012) may still be used to constrain the stress tensor field for structures without slip lines. The structural measurements were divided into subsets of data; i) baryte vein fill, ii) calcite vein fill and iii) veins from the islet. The principal paleostress axes for the sets were derived from the WinTensor software (Table 1). Notably, the kinematic analysis indicates a NW–SE- to NNW–SSE-trending extension direction for the veins. This extension direction is highly oblique to the dip-direction of all the larger-scale structures documented in the field and has a 20° – 30° more northerly trend than the NW–striking transtensional faults in Fig. 4.

Discussion

The following section presents a model for the development of southeastern Bjørnøya based on field data, potential field geophysics and regional geological relations. We compare our model with models from existing literature both from Bjørnøya and the Barents Sea and suggest new areas for potential sulfide mineralizations based on the structural setting presented in this paper.

Model for the structural development of Bjørnøya

Caledonian Orogeny and late–post-orogenic collapse

The main structural trend described in this work stems from the Caledonian orogeny and associated N–S-striking thrusting and folding. At the largest scale, regional N–S-striking faults separate the Stappen High from the Fingerdjupet Subbasin in the east and the Knølegga Fault Complex and Vestbakken Volcanic Province in the west (Fig. 1), extending to the North and South of Bjørnøya and creating 400-km long lineaments in the potential field data (Fig. 2). The faults that form these boundaries probably originated during collapse following the Caledonian Orogenesis, forming along preexisting thrusts. As described by Braathen et al. (1999), similar reactivation is documented along thrusts in southeastern Bjørnøya. Large-scale folds with similar N–S trends also rework the surrounding rocks, the axial traces of which are shown in Fig. 4. We relate the folds to the compression and mountain building during the Caledonian Orogeny, following Braathen et al. (1999) on Bjørnøya and elsewhere in the Barents Sea region (Gee and Hjelle, 1966, Harland et al., 1992, Witt-Nilsson et al., 1998, Koehl and Allaart, 2021, Koehl et al., 2022). The structural trends developed during the orogenies directly influenced the subsequent collapse of the mountain belt and subordinate structural evolution.

Using LiDAR data and lineament analysis we quantified the structural fabric of southeastern Bjørnøya (Fig. 5). N–S-striking structures are a key component of the structural fabric at both large 100 x 100 m grid and smaller 25 x 25 m grid scales. Despite a prolonged tectonic evolution, the structural trend first

defined through Caledonian thrusting and later collapse remains preserved. While many of the extensional structures documented in this work directly exploit pre-existing Caledonian features, other structures form along oblique trends possibly related to the Timian orogeny (Koehl et al., 2022), or unrelated to earlier events.

Fault linkage during orogenic collapse

We propose that the structures we interpret to be NW–SE-striking transtensional faults formed because of fault linkage between larger N–S-striking extensional structures (Fig. 10). Some of the NW–SE-striking faults documented in this study were previously mapped as normal faults (Dallmann and Krasil'Scikov, 1996). However, based on the stress field during faulting indicated be the stress tensor analysis (Fig. 9), the offset of cross-cutting features in the field suggest that the faults have a significant oblique component. In addition, movement along linking faults in the fault-linkage model (Fossen and Rotevatn, 2016) is necessarily oblique, following geometrical constraints, supporting our interpretation of oblique transtensional slip along the faults. The fault network formed by the N–S and NW–SE-striking structures is consistent with fault linkage setting, as described by Fossen and Rotevatn (2016). The N–S-striking normal faults in southeastern Bjørnøya were in close enough proximity that significant interaction between the faults could take place. Such interaction apparently resulted in a complex array of structures, including what we interpret to be NW–SE-striking transtensional faults and NE–SW-striking veins, linking the major N–S-striking structures in a single network. This is consistent with the oblique slip along the NW–SE-striking faults as well as the orientation of veins documented on the Russehamna islet (Fig. 8), which in conjunction with the orientation of the larger surrounding faults indicates a transtensional setting. Based on field evidence including the presence of sulfide mineralized breccias in fault cores, we suggest an important interplay between the NW–SE-striking structures and the sulfide mineralizations in southeastern Bjørnøya, typically found in vein clusters or damage zones surrounding the transtensional faults (Fig. 4, Fig. 6, Fig. 7, & Fig. 8). Numerous small faults within the larger damage zones and the juxtaposition of extensional and transtensional fault geometries provided ample fluid pathways for the mineralizing fluids. As the fluids ascended along the fault network, boiling and the expansion of the fluids led to fluid overpressure and the formation of massive hydrothermal breccias and structures (Fig. 6E & Fig. 7), following the processes described by Cox (2010), Cox (2016).

Structural setting and timing of sulfide mineralization and related faulting

We used the array of mineralized baryte and calcite veins to describe the stress field in which the sulfide mineralizations formed and in which faulting events along the NW–SE-striking transtensional faults transpired. We suggest that the mineralizing events and faulting were approximately coeval, based on the presence of mineralized fault breccia along the Russeelva River and the relationship between sphalerite

mineralizations and structurally controlled veins (Fig. 6E, F, G & Fig. 7). The hydrothermal mineralization style is consistent with the faulting style described by Sibson et al. (1975). Fault linkage settings like we suggest for southeastern Bjørnøya are consistent with increased fluid permeability and frequent ore occurrences (Xi et al., 2005, Fossen and Rotevatn, 2016). The geometry and style of fault linkage settings also exert a significant structural control on ore formation (Xi et al., 2005), in part defining the shape and position of ore bodies. Based on our field mapping, the mineralizations on southeastern Bjørnøya are constrained to specific zones with a high frequency of fractures which we consider to be the zones with the most significant fault linkage and fluid migration. The increased number of fractures and deformation zones as well as the presence of intersecting structural features and the rotation or perturbation of the local stress field all contribute to increased permeability and fluid migration in linkage settings, improving conditions for the formation of mineral deposits (Fossen and Rotevatn, 2016). A similar relationship of vein mineralization and faulting is described in Eastern Greenland (Pedersen and Stendal, 2000), in Carbonifeous and Permian strata along the Eastern Fault Zone.

The ore-forming fluids migrated along pressure gradients, following the model described by (Sibson et al., 1975). In normal faults, increasing tectonic shear stress leads to fault dilatancy, forming fractures and reducing fluids pressure. Eventually, the shear stress surpasses the frictional strength of the rocks, causing earthquakes. The resulting relaxation of fractures permits the fluids to migrate upwards. The transtensional faults described in this study may have followed such a fluid migration mechanism.

Dating the sulfide mineralization and associated carbonates using Rb/Sr and U/Pb radiogenic isotope systems was not possible as both Rb and U levels were below detection limits, preventing absolute age constraints for the mineralizations. The orientation and principal stress tensors of associated structures, however, can be used to correlate the mineralization with broader regional events. The mineralized veins and associated NW–SE-striking faults cut the Caledonian thrusts, locally displacing these for nearly 100 meters laterally along strike (Fig. 4). The NW–SE-striking transtensional faults also displace some of the N–S-striking normal faults, indicating slip along the NW–SE-striking structures followed the formation of the N–S-striking structures. The spatial correlation between the frequency of mineralized veins and NW–SE-striking faults as well as the presence of local sulfide mineralization in fault breccia associated with the NW–SE-striking faults suggests that these features are related and approximately coeval. These structures post-date the Caledonian Orogeny, though they may be related to the subsequent orogenic collapse. Constraining a youngest possible age for the faults and mineralization is more difficult. Lepvrier et al. (1989) argue that all significant faults on Bjørnøya are older than late Permian, with most extensional faulting occurring in the Carboniferous to early Permian. The Røedvika Formation, a part of the Billefjorden Group, which lies on top of the pre-Caledonian basement, has a Famennian age (Worsley

et al., 2001, Lopes et al., 2021). The mineralized veins are mostly constrained to the lower, pre-Caledonian units, though some minor mineralization has been found in the Røedvika Formation. Both the N–S-striking extensional faults and the NW–SE-striking transtensional faults cut the Røedvika Formation, indicating they are Famennian or younger age, while there is no evidence that the mineralized structures cut the younger Late Permian Tempelfjorden Group. In summary, the relationship between geological units and cross cutting structures suggests the faulting and mineralization occurred between the latest Devonian (Famennian) and Middle Permian. By comparing southeastern Bjørnøya with nearby geological domains, such as the Fingerdjupet subbasin, we suggest that the fault linkage and formation of ore deposits on Bjørnøya occurred during the Carboniferous, though a later development through the Permian is also plausible. A Permian–Triassic development is less likely, considering the relative tectonic stability of the Barents Sea during this period (Faleide et al., 2008, Serck and Braathen, 2019, Gresseth et al., 2021).

Comparison with previous work

Though many articles consider the large-scale effects of Paleozoic deformation, relatively little is known regarding the detailed effects of the Caledonian orogeny on the western Barents Sea basement. Investigations are hampered by significant sedimentary and oceanic coverage and are forced to rely on interpreted deep seismic profiles. On Bjørnøya, the N–S-striking thrusts, normal faults, and folds described by Braathen et al. (1999) and the faulting patterns identified by Lepvrier et al. (1989) are again described in this work. Building upon these detailed field observations, we further document the structures through magnetic modelling and lineament analysis (Fig. 3 & 5). The results of the magnetic modelling indicate the influence of post-Caledonian extension and normal faulting on shallow crystalline continental crust beneath Bjørnøya (Fig. 3), while the lineament analysis (Fig. 5) highlights the importance of the N–S-striking structural trend for the modern geometry and relief of southeastern Bjørnøya and the NW–SE trend which both this paper and Lepvrier et al. (1989) attribute to transtension. This is also observed on the filtered magnetic map (Fig. 3C). We suggest that the NW–SE-striking structures are related to basement structures in the shallow crystalline crust beneath Bjørnøya. The depth to the crust is in agreement with modelling and geophysical interpretation by Libak et al. (2012), who modelled an over 400 km long profile extending southwest from an area near southeast Bjørnøya. Previously, only the largest scale structures in the western Barents Sea were constrained. More recent works, such as Blaich et al. (2017) and Gresseth et al. (2021), use newer, higher-resolution data to better constrain rift-related structures and detachment faults. Such data are not yet available for the Bjørnøya region.

The model proposed in our study is consistent with the structural evolution proposed by Gresseth et al. (2021), who document a N–S- to NNE–SSW-striking Caledonian detachment fault beneath the Fingerdjupet subbasin active throughout the Devonian and Carboniferous and reactivated in the Mesozoic. The fault thereby exerted significant control on the surrounding structural development. Like the N–S-striking extensional faults on Bjørnøya, the detachment exploited rheologically weak zones where thrusting occurred during the Caledonian Orogeny (Gresseth et al., 2021). Numerous works describe multiphase rifting following the Devonian, through the Carboniferous and into the early Permian (e.g. Faleide et al. (2008)). The faults documented in this work are consistent with the findings of these earlier authors with respect to the orientation of the structures and relative timing based on cross-cutting relationships and tectonostratigraphic relations. Our findings regarding the principal stress tensor analysis (Fig. 9) pertaining to the mineralized veins and corresponding transtensional faults are nearly identical to the stress analysis performed by Lepvrier et al. (1989), with one key difference. Lepvrier et al. (1989) suggested a phase of compression based on striation lineations and a conjugate set of fault planes, one branch of which only includes four measurements. Our NE–SW-striking mineralized vein measurements are consistent with most of their measurements, though the strain analysis indicates NNW–SSE extension, rather than compression. This stress field results in oblique slip along the related NW–SE-striking transtensional faults, which we suggest is consistent with a fault linkage setting (Fossen and Rotevatn, 2016) between large N–S-striking extensional faults related to larger basement structures beneath Bjørnøya. Our proposed model for the development of Bjørnøya is consistent with this previous work and provides a new perspective on the influence of existing structures during mountain chain collapse, fault linkage, and hydrothermal activity.

Onshore–offshore correlation for emerging industries

Field exposures like those in southeastern Bjørnøya are relatively rare, as continental shelves are generally submerged. By combining field studies with geophysical data, as well as drill core and other datatypes, geologists can extrapolate onshore knowledge offshore. It is highly likely that large mineral deposits exist along buried Atlantic margins (Hannington et al., 2017). However, inherent difficulties related to direct targeting of ore deposits offshore, the resolution and attenuation of geophysical signals at depth (Landrø and Amundsen, 2018), the high cost of offshore exploration, and a lack of detailed geological knowledge pertaining to mineral deposits in these areas hamper exploration. Despite these challenges, our study demonstrates that the identification of large-scale ore-forming systems on Bjørnøya may be adapted and used as an analogue model in the search for other mineral deposits at sub-sea

basement culminations in the Barents Sea. Here, shallow water depths facilitate high resolution geophysical techniques and, hypothetically, the identification of significant ore deposits.

Conclusion

N–S-striking normal faults cut the Hecla Hoek basement rocks and are hard-linked by a series of NW–SE-striking likely oblique transtensional faults. A high frequency of subvertical, explosive- to planar hydrothermal veins support a transtensional stress field along ENE–WSW-striking faults. These veins contain sphalerite, galena, and other accessory minerals in a predominantly baryte and/or calcite matrix.

The fault linkage setting created favorable conditions for the formation of mineralizations and several sub-economic ore-deposits on Bjørnøya. By combining land-based field studies with potential field and other offshore data geologists may extrapolate geological knowledge from the onshore to the offshore domain, potentially finding larger deposits, and allowing for more precise prospecting on submerged continental shelf through the development of relevant analogue models.

Regarding exploration for mineral resources in the Barents Sea, the findings in this study indicate that a substantial exploration potential exists in transtensional linkage zones between large-scale faults formed during late–post-Caledonian collapse. This present study highlights the importance of constraining the location and evolution of Late Paleozoic basement-rooted faults, as these structures create the structural template for fluid migration and potential economic mineralization.

Acknowledgements

We heartily acknowledge Professor Atle Mørk for his assistance in organizing, carrying out, and securing funding for the field work upon which this study is based. Funding for this study was also generously provided by the Norwegian Research Council through the Arctic Field Grant program. Finally, we extend a sincere thank you to the editor Dr. Espen Torgersen, and reviewers Dr Jean-Baptiste Koehl and Dr. Ben Snook for an expedient and constructive review process, resulting in an improved version of our study.

References

Afifi, A. M. 2005. Ghawar: The anatomy of the world's largest oil field. *AAPG Search and Discovery,* 20026.

Allmendinger, R. W., Cardozo, N. & Fisher, D. M. 2011. *Structural geology algorithms: Vectors and tensors*, Cambridge University Press.

Åm, K. 1975. Aeromagnetic basement complex mapping north of latitude 62° N, Norway.

Andersson, J. G. 1901. *Über die Stratigraphie und Tektonik der Bären-Insel*, Almqvist & Wiksell.

Barrère, C., Ebbing, J. & Gernigon, L. 2011. 3-D density and magnetic crustal characterization of the southwestern Barents Shelf: implications for the offshore prolongation of the Norwegian Caledonides. *Geophysical Journal International,* 184**,** 1147-1166.

Bjørlykke, A., Lepland, A. & Skår, Ø. 2021. Origin of the mineralised Hawke Bay conglomerate and its importance in formation of the Vassbo lead-zinc deposit, Sweden. *Norwegian Journal of Geology/Norsk Geologisk Forening,* 101.

Blaich, O. A., Tsikalas, F. & Faleide, J. I. 2017. New insights into the tectono-stratigraphic evolution of the southern Stappen High and its transition to Bjørnøya Basin, SW Barents Sea. *Marine and Petroleum Geology,* 85**,** 89-105.

Braathen, A., Maher, H. D., Haabet, T. E., Kristensen, S. E., Tørudbakken, B. O. & Worsley, D. 1999. Caledonian thrusting on Bjørnøya: Implications for Palaeozoic and Mesozoic tectonism of the western Barents Shelf. *Norsk Geologisk Tidsskrift,* 79**,** 57-68.

Braathen, A., Osmundsen, P. T., Maher, H. & Ganerød, M. 2018. The Keisarhjelmen detachment records Silurian-Devonian extensional collapse in Northern Svalbard. *Terra Nova,* 30**,** 34-39.

Brönner, M., Marello, L., Koziel, J., Pascal, C. & Gernigon, L. 2010. Barents Sea Aeromagnetic Remapping BASAR-09-Aquisition and processing report and preliminary interpretation of the SW Barents Sea.

Buckley, S. J., Ringdal, K., Naumann, N., Dolva, B., Kurz, T. H., Howell, J. A. & Dewez, T. J. B. 2019. LIME: Software for 3-D visualization, interpretation, and communication of virtual geoscience models. *Geosphere,* 15**,** 222-235.

Cardozo, N. & Allmendinger, R. W. 2013. Spherical projections with OSXStereonet. *Computers & Geosciences,* 51**,** 193-205.

Clark, D. 1997. Magnetic petrophysics and magnetic petrology: aids to geological interpretation of magnetic surveys.

Cox, S. F. 2010. The application of failure mode diagrams for exploring the roles of fluid pressure and stress states in controlling styles of fracture-controlled permeability enhancement in faults and shear zones. *Geofluids*.

Cox, S. F. 2016. Injection-Driven Swarm Seismicity and Permeability Enhancement: Implications for the Dynamics of Hydrothermal Ore Systems in High Fluid-Flux, Overpressured Faulting Regimes—An Invited Paper. *Economic Geology,* 111**,** 559-587.

Dallmann, W. K. & Krasil'scikov, A. 1996. *Geological map of Svalbard 1:50000, sheet D20G Bjørnøya.* Oslo: Norsk Polarinstitutt.

Delvaux, D. Release of program Win-Tensor 4.0 for tectonic stress inversion: statistical expression of stress parameters. Geophysical research abstracts, 2012. EGU General Assembly Vienna.

Delvaux, D. & Sperner, B. 2003. New aspects of tectonic stress inversion with reference to the TENSOR program. *Geological Society, London, Special Publications,* 212**,** 75-100.

Dentith, M. & Mudge, S. T. 2014. *Geophysics for the mineral exploration geoscientist*, Cambridge University Press.

Dumais, M.-A., Olesen, O., Gernigon, L., Brönner, M., Lim, A. & Johansen, S. 2020. Knipovich Ridge Aeromagnetic Survey 2016: processing and interpretation.

Ebbing, J., Braitenberg, C. & Wienecke, S. 2007. Insights into the lithospheric structure and tectonic setting of the Barents Sea region from isostatic considerations. *Geophysical Journal International,* 171**,** 1390-1403.

Faleide, J. I., Gudlaugsson, S. T. & Jacquart, G. 1984. Evolution of the western Barents Sea. *Marine and Petroleum Geology,* 1**,** 123-150.

Faleide, J. I., Pease, V., Curtis, M., Klitzke, P., Minakov, A., Scheck-Wenderoth, M., Kostyuchenko, S. & Zayonchek, A. 2018. Tectonic implications of the lithospheric structure across the Barents and Kara shelves. *Geological Society, London, Special Publications,* 460**,** 285-314.

Faleide, J. I., Solheim, A., Fiedler, A., Hjelstuen, B. O., Andersen, E. S. & Vanneste, K. 1996. Late Cenozoic evolution of the western Barents Sea-Svalbard continental margin. *Global and Planetary Change,* 12**,** 53-74.

Faleide, J. I., Tsikalas, F., Breivik, A. J., Mjelde, R., Ritzmann, O., Engen, O., Wilson, J. & Eldholm, O. 2008. Structure and evolution of the continental margin off Norway and the Barents Sea. *Episodes,* 31**,** 82-91.

Fichler, C. & Pastore, Z. 2022. Petrology of the crystalline crust in the southwestern Barents Sea inferred from geophysical data. *Norwegian Journal of Geology***,** 40.

Fossen, H. & Rotevatn, A. 2016. Fault linkage and relay structures in extensional settings—A review. *Earth-Science Reviews,* 154**,** 14-28.

Gabrielsen, R. H., Faerseth, R. B. & Jensen, L. N. 1990. *Structural elements of the Norwegian continental shelf. Pt. 1. The Barents Sea region*, Norwegian Petroleum Directorate.

Gee, D. G., Fossen, H., Henriksen, N. & Higgins, A. K. 2008. From the early Paleozoic platforms of Baltica and Laurentia to the Caledonide Orogen of Scandinavia and Greenland. *Episodes,* 31**,** 44-51.

Gee, D. G. & Hjelle, A. 1966. On the crystalline rocks of northwest Spitsbergen. *Norsk Polarinstitutt Årbok,* 1964**,** 31-45.

Gernigon, L. & Brönner, M. 2012. Late Palaeozoic architecture and evolution of the southwestern Barents Sea: insights from a new generation of aeromagnetic data. *Journal of the Geological Society,* 169**,** 449-459.

Gernigon, L., Brönner, M., Roberts, D., Olesen, O., Nasuti, A. & Yamasaki, T. 2014. Crustal and basin evolution of the southwestern Barents Sea: From Caledonian orogeny to continental breakup. *Tectonics,* 33**,** 347-373.

Gernigon, L., Franke, D., Geoffroy, L., Schiffer, C., Foulger, G. R. & Stoker, M. 2019. Crustal fragmentation, magmatism, and the diachronous opening of the Norwegian-Greenland Sea. *Earth-Science Reviews*.

Gresseth, J. L. S., Braathen, A., Serck, C. S., Faleide, J. I. & Osmundsen, P. T. 2021. Late Paleozoic supradetachment basin configuration in the southwestern Barents Sea—Intrabasement seismic facies of the Fingerdjupet Subbasin. *Basin Research*.

Gudlaugsson, S., Faleide, J., Johansen, S. & Breivik, A. 1998. Late Palaeozoic structural development of the south-western Barents Sea. *Marine and Petroleum Geology,* 15**,** 73-102.

Hannington, M., Petersen, S. & Krätschell, A. J. N. G. 2017. Subsea mining moves closer to shore. 10**,** 158.

Harland, W., Scott, R., Auckland, K. & Snape, I. 1992. The Ny Friesland Orogen, Spitsbergen. *Geological Magazine,* 129**,** 679-707.

Harland, W. B., Hambrey, M. J. & Waddams, P. 1993. Vendian geology of Svalbard.

Hinze, W. J., Von Frese, R. R., Von Frese, R. & Saad, A. H. 2013. *Gravity and magnetic exploration: Principles, practices, and applications*, Cambridge University Press.

586 Holtedahl, O. 1920. On the Paleozoic series of Bear Island, especially on the Heclahook system: Norsk
587 Geol. Tidsskr.
588 Horn, G. & Orvin, A. K. 1928. Geology of Bear Island: with special reference to the coal deposits, and
589 with an account of the history of the island.
590 Kelley, K. D. & Jennings, S. 2004. A special issue devoted to barite and Zn-Pb-Ag deposits in the Red Dog
591 district, western Brooks Range, northern Alaska. *Economic Geology,* 99**,** 1267-1280.
592 Koehl, J.-B. P. & Allaart, L. 2021. The Billefjorden Fault Zone north of Spitsbergen: a major terrane
593 boundary? *Polar Research,* 40.
594 Koehl, J.-B. P., Magee, C. & Anell, I. M. 2022. Impact of Timanian thrust systems on the late
595 Neoproterozoic–Phanerozoic tectonic evolution of the Barents Sea and Svalbard. *Solid Earth,* 13**,**
596 85-115.
597 Landrø, M. & Amundsen, L. 2018. *Introduction to exploration geophysics with recent advances*, Bivrost.
598 Lepvrier, C., Leparmentier, F. & Seland, R. 1989. Upper Palaeozoic faulting regimes in Bjornoya
599 (Svalbard, Norway). *Bulletin de la Société géologique de France***,** 411-416.
600 Libak, A., Mjelde, R., Keers, H., Faleide, J. I. & Murai, Y. 2012. An integrated geophysical study of
601 Vestbakken Volcanic Province, western Barents Sea continental margin, and adjacent oceanic
602 crust. *Marine Geophysical Research,* 33**,** 185-207.
603 Lopes, G., Mangerud, G., Clayton, G. & Vigran, J. O. 2021. Palynostratigraphic reassessment of the Late
604 Devonian of Bjørnøya, Svalbard. *Review of Palaeobotany and Palynology,* 286**,** 104376.
605 Marello, L., Ebbing, J. & Gernigon, L. 2013. Basement inhomogeneities and crustal setting in the Barents
606 Sea from a combined 3D gravity and magnetic model. *Geophysical Journal International,* 193**,**
607 557-584.
608 Maus, S., Barckhausen, U., Berkenbosch, H., Bournas, N., Brozena, J., Childers, V., Dostaler, F., Fairhead,
609 J. D., Finn, C., Von Frese, R. R. B., Gaina, C., Golynsky, S., Kucks, R., Lühr, H., Milligan, P., Mogren,
610 S., Müller, R. D., Olesen, O., Pilkington, M., Saltus, R., Schreckenberger, B., Thébault, E. &
611 Caratori Tontini, F. 2009. EMAG2: A 2-arc min resolution Earth Magnetic Anomaly Grid compiled
612 from satellite, airborne, and marine magnetic measurements. *Geochemistry, Geophysics,*
613 *Geosystems,* 10**,** n/a-n/a.
614 Muir-Wood, R. & King, G. C. P. 1993. Hydrological signatures of earthquake strain. *Journal of Geophysical*
615 *Research: Solid Earth,* 98**,** 22035-22068.
616 Naliboff, J. B., Glerum, A., Brune, S., Péron-Pinvidic, G. & Wrona, T. 2020. Development of 3-D Rift
617 Heterogeneity Through Fault Network Evolution. *Geophysical Research Letters,* 47.
618 Npd. 2019. *FactPages and FactMaps* [Online]. Norway: NPD. Available:
619 https://www.npd.no/en/facts/factpages/ [Accessed March 15th 2019].
620 Olesen, O., Brönner, M., Ebbing, J., Gellein, J., Gernigon, L., Koziel, J., Lauritsen, T., Myklebust, R., Pascal,
621 C. & Sand, M. New aeromagnetic and gravity compilations from Norway and adjacent areas:
622 methods and applications. Geological Society, London, Petroleum Geology Conference series,
623 2010. Geological Society of London, 559-586.
624 Osmundsen, P. & Péron-Pinvidic, G. 2018. Crustal-scale fault interaction at rifted margins and the
625 formation of domain-bounding breakaway complexes: Insights from offshore Norway. *Tectonics,*
626 37**,** 935-964.
627 Pedersen, M. & Stendal, H. 2000. Mineral occurrences in central East and North-East Greenland—new
628 possibilities? *Applied Earth Science,* 109**,** 42-48.
629 Ritzmann, O. & Faleide, J. I. 2007. Caledonian basement of the western Barents Sea. 26**,** n/a-n/a.
630 Roberts, D. & Olovyanishnikov, V. 2004. Structural and tectonic development of the Timanide orogen.
631 *Geological Society, London, Memoirs,* 30**,** 47-57.

Rønning, S. & Skilbrei, J. R. 1998. Acquisition and processing report HRAMS97-1. Southwestern Barents Sea High Resolution Aeromagnetic Survey 97-98. Report 98.131 ed.: Geological Survey of Norway (NGU).
Sandwell, D. T., Müller, R. D., Smith, W. H., Garcia, E. & Francis, R. 2014. New global marine gravity model from CryoSat-2 and Jason-1 reveals buried tectonic structure. *science,* 346**,** 65-67.
Serck, C. S. & Braathen, A. 2019. Extensional fault and fold growth: Impact on accommodation evolution and sedimentary infill. *Basin Research,* 31**,** 967-990.
Shulgin, A., Faleide, J. I., Mjelde, R., Breivik, A. & Huismans, R. 2020. Crustal domains in the Western Barents Sea. *Geophysical Journal International,* 221**,** 2155-2169.
Sibson, R. H. 2000. Fluid involvement in normal faulting. *Journal of Geodynamics,* 29**,** 469-499.
Sibson, R. H., Moore, J. M. M. & Rankin, A. H. 1975. Seismic pumping--a hydrothermal fluid transport mechanism. 131**,** 653-659.
Smelror, M., Petrov, O., Larssen, G. B. & Werner, S. 2009. Geological history of the Barents Sea. *Norges Geol. undersøkelse***,** 1-135.
Taylor, R. D. L., Bradley, D. L., Pisarevsky, D. C. & Sergei, A. 2009. Mineral resource data for Mississippi Valley-Type and clastic-dominated sediment-hosted lead-zinc deposits.
Whitney, D. L., Teyssier, C., Rey, P. & Buck, W. R. 2013. Continental and oceanic core complexes. *Geological Society of America Bulletin,* 125**,** 273-298.
Witt-Nilsson, P., Gee, D. G. & Hellman, F. J. 1998. Tectonostratigraphy of the Caledonian Atomfjella Antiform of northern Ny Friesland, Svalbard. *Norsk Geologisk Tidsskrift,* 78**,** 67-80.
Worsley, D., Agdestein, T., Gjelberg, J. G., Kirkemo, K., Mørk, A., Nilsson, I., Olaussen, S., Steel, R. J. & Stemmerik, L. 2001. The geological evolution of Biørnøya, Arctic Norway: implications for the Barents Shelf. *Norwegian Journal of Geology/Norsk Geologisk Forening,* 81.
Xi, X.-S., Tang, J.-R., Kong, H. & He, S.-X. 2005. Control of relay structure on mineralization of sedimentary-exhalative ore deposit in growth faults of graben systems. *Journal of Central South University of Technology,* 12**,** 340-345.

Figure Text

Figure 1. Regional map of the (A) structural elements in the Barents Sea and in Northern Norway (NPD, 2019). The inset (B) shows the basic geology of Bjørnøya from (Dallmann and Krasil'Scikov, 1996), and a simplified stratigraphy. The position of Bjørnøya is denoted on the regional map. Modified from Sigmond (2002), Gabrielsen et al. (1990), and Gernigon and Brönner (2012).

Figure 2. Compilation of regional gravity and magnetic maps from the western Barents Sea, showing the magnetic response of key structural elements in the Barents Sea. The white lines denote structural elements in the Barents Sea from NPD (2019). HSZ = Hornsund Fault Zone, SH = Stappen High. Other structural elements are identified in figure 1. (A) Offshore free-air and onshore Bouguer gravity anomaly map (Marine and land gravity data by Olesen et al. (2010), Free-air satellite gravity data by Sandwell et al. (2014). The white lines denote major lineaments traced manually from the dataset. (B) Filtered gravity anomaly map of the dataset in (A). (C) Magnetic anomaly (TMI) map compiled from DRAGON Aeromagnetic data compilation by Olesen et al. (2010), KRAS-16 Aeromagnetic survey by Dumais et al. (2020), BASAR-09 Aeromagnetic survey by Brönner et al. (2010), HRAMS Aeromagnetic survey by

Rønning and Skilbrei (1998) and EMAG2 Aeromagnetic data compilation by Maus et al. (2009). (D) Filtered magnetic anomaly map of the dataset in (C).

Figure 3. BASAR-09 magnetic map of Bjørnøya. (A) Unfiltered magnetic anomalies. (B) Residual after removal of 3rd degree polynomial. (C) Tilt derivative filtered and upward continuated (100 m). (d) Interpreted magnetic profile, combined with field observations (position of faults) along survey line T5090. The dashed arrows indicate the original transport direction along later-reactivated Caledonian thrusts. The projected position of the mine and vein mineralizations are also shown on the profile.

Figure 4. Structural and lithological map of southeastern Bjørnøya. Upper-hemisphere stereonets show the orientation of the bedding and mineralized veins (poles to planes) in the study. Prominent structural features include NS-striking thrusts and normal faults, NS-striking fold axes, and NW-SE-striking transtensional faults. The position of prominent mineralization is noted on the map and a tectonostratigraphic column includes the lithologies and their specific ages, after Harland et al. (1993), for the field area. The location of the profile X–X' interpreted in Fig. 3D is denoted on the map as a black dashed line.

Figure 5. Rose diagrams for the lineations selected from the DEM and filtered magnetic data. (A) Lineation rose for the 100m x 100m standard deviation of elevation grid (B) Lineation rose for the 25m x 25m grid highlighting smaller structures than the larger 100m x 100m grid. (C) Lineation rose for lineations selected from the tilt-derivative filtered magnetic data (Fig. 3C).

Figure 6. Field photographs from southeastern Bjørnøya. (A) Two interpreted NW-SE-striking transtensional faults cutting the Russehamna Formation near the northerly contact with the Sørhamna Formation. The faulted cliff face is approximately 50 meters high. The fault traces are clearly visible in LiDAR data, extending over 100 meters inland. (B) Outcrop photograph of the core of a NW–SE-striking fault. The red zone denotes the fault core of a NW-SE-striking transtensional fault, exposed along the Russeelva river. The inset shows fault breccia, locally with dispersed sphalerite and baryte-filled veins, indicating coeval faulting and mineralization. The core is covered by undeformed rock at the bend in the river, where the red zone stops. (C) Open, gentle folding of inferred Caledonian age, along the Russeelva river. (D) A small fault in the Russehamna Formation, with a baryte core. The fault shows less than 10 cm of displacement and is typical of the damage zones surrounding the transtensional faults. (E) Hydrothermal breccia with sphalerite along a typical baryte vein near the Russeelva river. (F) Planer mineralization style along a second hydrothermal vein, showing multiple generations of sphalerite (red, yellow, and grey) and baryte. (G) Thin section of the breccia in (C), the clasts of sphalerite are distinct

703 within the light-colored baryte and quartz (sub image resolution) matrix, with angular clasts of the
704 carbonate host rock. The holes appear yellow, following the use of colored epoxy.

705 Figure 7. Large mineralized baryte veins along the coast of Bjørnøya. (A) A network vein near the contact
706 between the Russehamna and Sørhamna Formations just north of Sørhamna (Fig. 4). (B) A second large
707 vein near the northern extent of the Russehamna Formation, adjacent to the faults in Fig. 6A. The cliff
708 face is approximately 50 meters high.

709 Figure 8. 3D model from Russehamna, created via photogrammetry with georeferenced images. (A) and
710 (B) show two profiles flown along the northwestern portion of either side of a small islet. The position of
711 the profiles is noted in (C). (D) Conjugate tensile veins filled with baryte. (E) The position of the islet
712 compared to two branches of a large transtensional fault system (black lines).

713 Figure 9. Principal stress tensor analyses, all showing an NNW extension direction. (A) The baryte veins
714 show a low variation in orientation. (B) The calcite veins, with significantly more variable orientation. It
715 is unclear whether this is related to different generations of veins or has another cause. (C) The stress
716 tensor analyses for the veins shown in (C). The results are like the baryte veins in (A), through with a
717 steep southeasterly, rather than northwesterly dip. (D) An overview of the planes selected in the LIME
718 software (Buckley et al., 2019).

719 Figure 10. A model of fault linkage and the position of mineralization pathways on southeastern
720 Bjørnøya, modified from the general fault linkage model of Fossen and Rotevatn (2016). The interaction
721 of oblique faults and corresponding damage zones provides ample pathways for fluids to migrate from
722 depth (grey color – damage zone, pink color – Hekla Hoek basement rocks, red color – crystalline
723 basement).

724

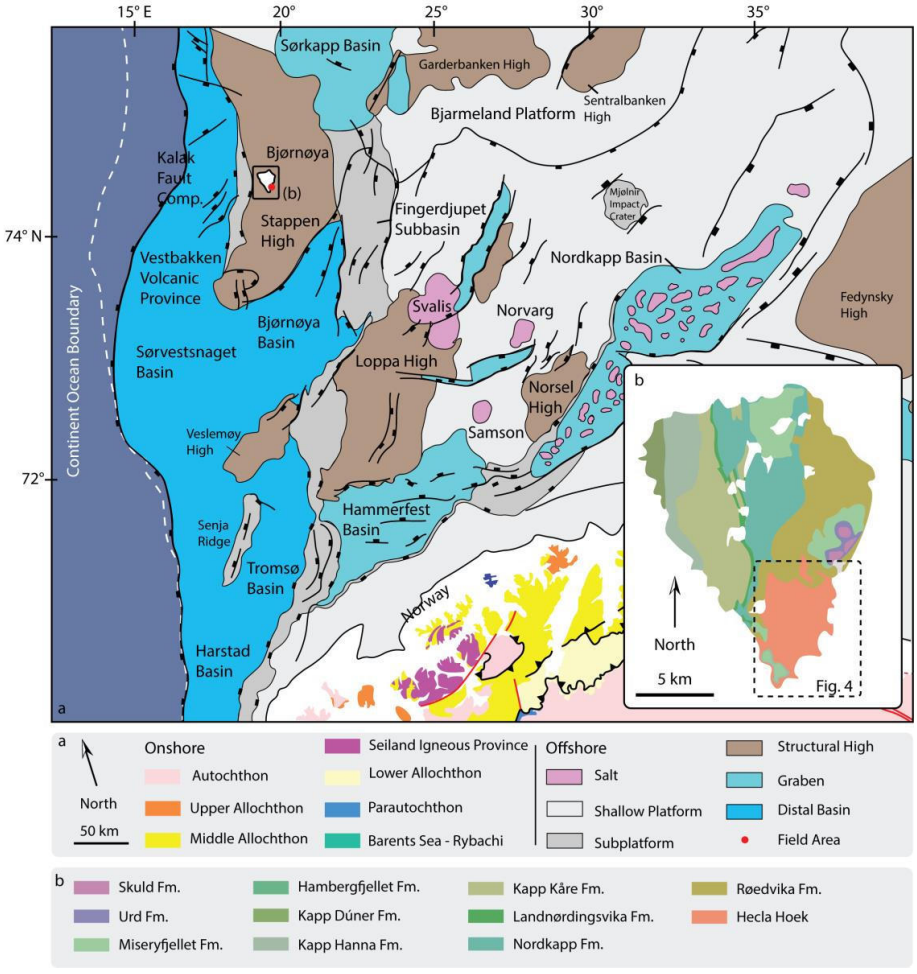
15° E
20°
25°
30°
35°
74° N
72°
Sørkapp Basin
Garderbanken High
Sentralbanken High
Bjarmeland Platform
Kalak Fault Comp.
Bjørnøya
(b)
Stappen High
Fingerdjupet Subbasin
Mjølnir Impact Crater
Nordkapp Basin
Fedynsky High
Vestbakken Volcanic Province
Svalis
Norvarg
Bjørnøya Basin
Sørvestsnaget Basin
Loppa High
Norsel High
Samson
Veslemøy High
Continent Ocean Boundary
Hammerfest Basin
Senja Ridge
Tromsø Basin
Norway
Harstad Basin
a
b
North
5 km
Fig. 4
a
North
50 km
Onshore
Autochthon
Upper Allochthon
Middle Allochthon
Seiland Igneous Province
Lower Allochthon
Parautochthon
Barents Sea - Rybachi
Offshore
Salt
Shallow Platform
Subplatform
Structural High
Graben
Distal Basin
Field Area
b
Skuld Fm.
Urd Fm.
Miseryfjellet Fm.
Hambergfjellet Fm.
Kapp Dúner Fm.
Kapp Hanna Fm.
Kapp Kåre Fm.
Landnørdingsvika Fm.
Nordkapp Fm.
Røedvika Fm.
Hecla Hoek

725

726 Fig. 1

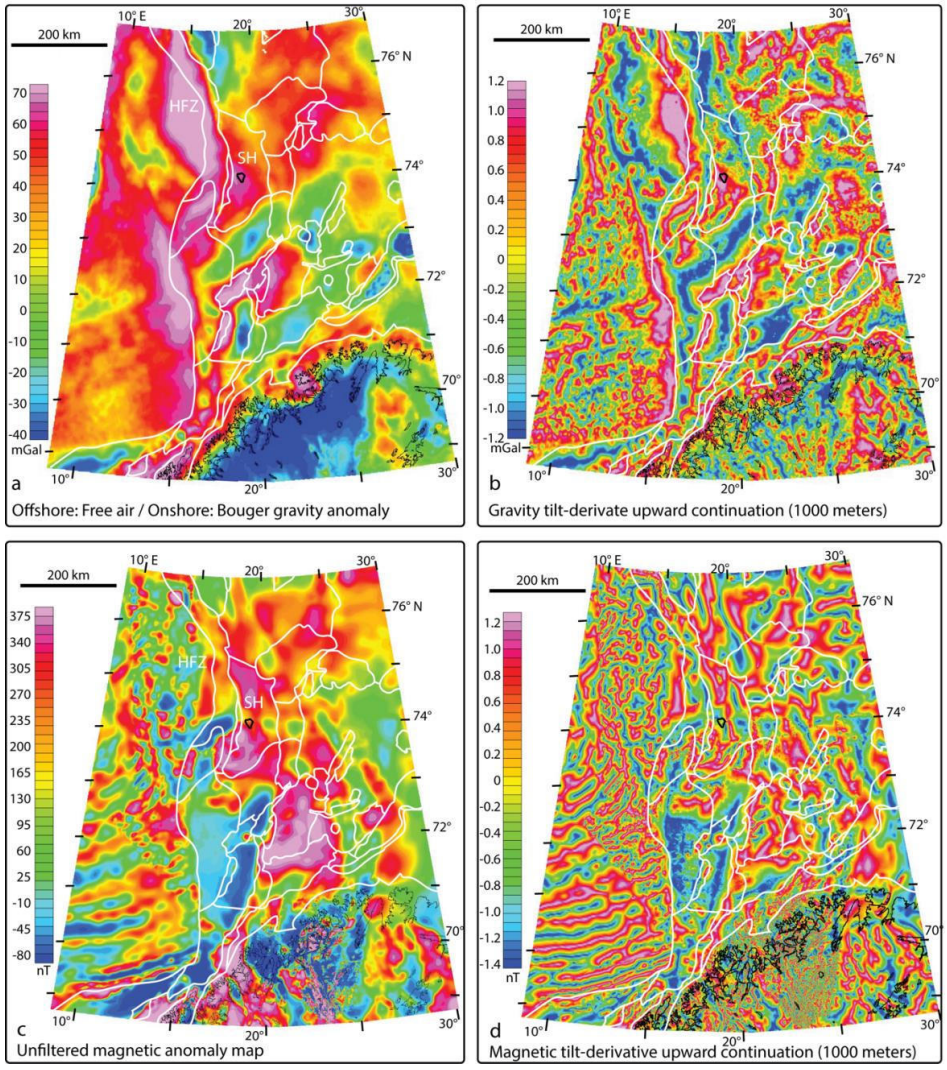
200 km
10° E
20°
30°
76° N
74°
72°
70°
HFZ
SH
70
60
50
40
30
20
10
0
-10
-20
-30
-40
mGal
a
Offshore: Free air / Onshore: Bouger gravity anomaly
1.2
1.0
0.8
0.6
0.4
0.2
0
-0.2
-0.4
-0.6
-0.8
-1.0
-1.2
b
Gravity tilt-derivate upward continuation (1000 meters)
375
340
305
270
235
200
165
130
95
60
25
-10
-45
-80
nT
c
Unfiltered magnetic anomaly map
-1.4
d
Magnetic tilt-derivative upward continuation (1000 meters)

727

728 Fig. 2

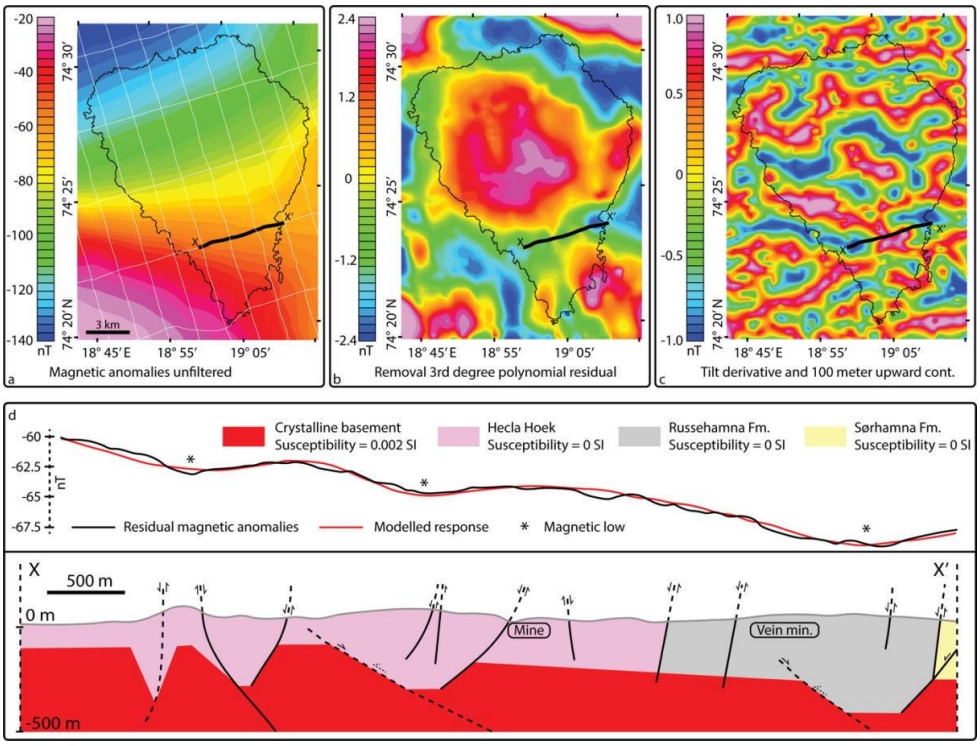
a
Magnetic anomalies unfiltered
b
Removal 3rd degree polynomial residual
c
Tilt derivative and 100 meter upward cont.
nT
3 km
18° 45′E
18° 55′
19° 05′
74° 30′
74° 25′
74° 20′N
d
Crystalline basement
Susceptibility = 0.002 SI
Hecla Hoek
Susceptibility = 0 SI
Russehamna Fm.
Susceptibility = 0 SI
Sørhamna Fm.
Susceptibility = 0 SI
Residual magnetic anomalies
Modelled response
Magnetic low
X
X′
500 m
0 m
-500 m
Mine
Vein min.

729

730 Fig. 3

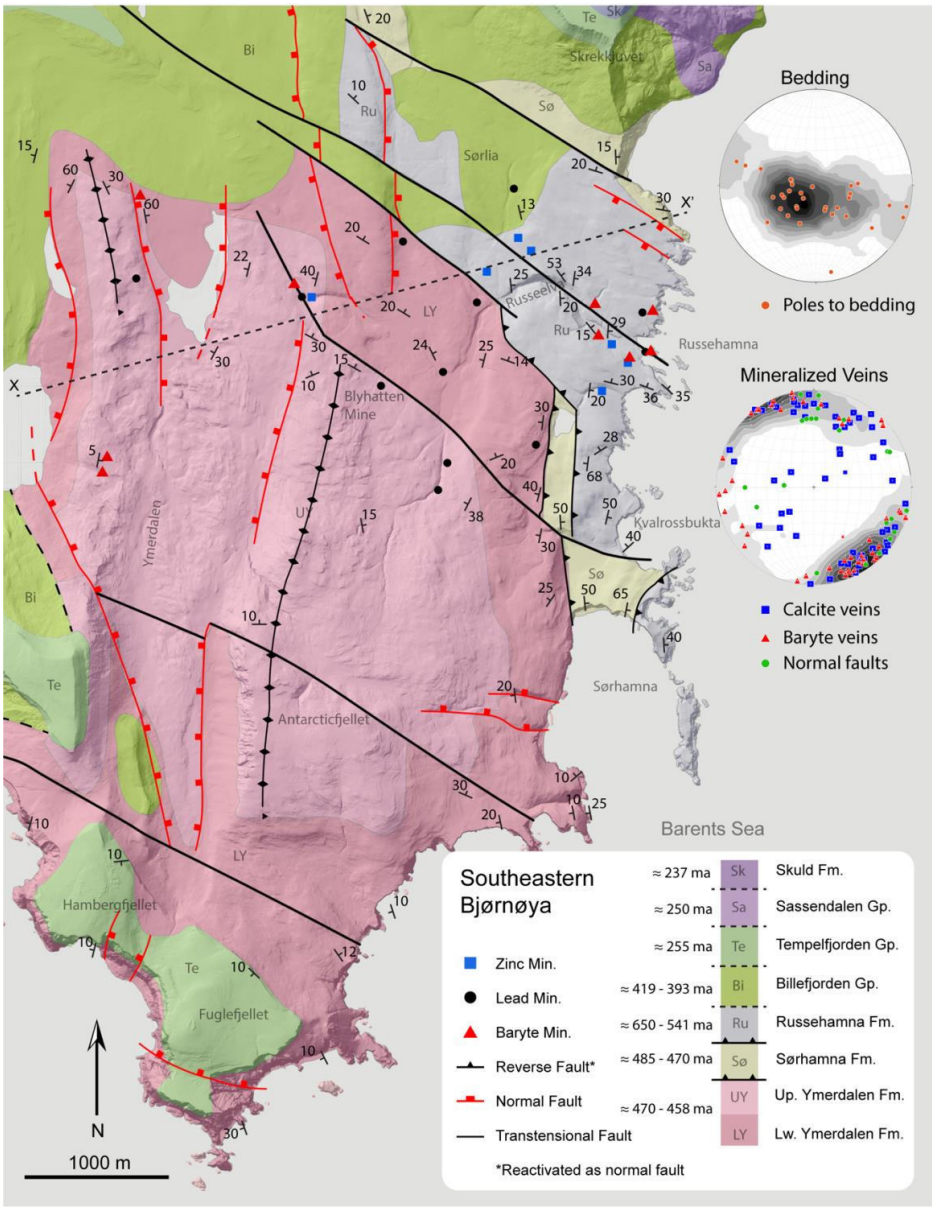
Bedding
Poles to bedding
Mineralized Veins
Calcite veins
Baryte veins
Normal faults
Southeastern Bjørnøya
Zinc Min.
Lead Min.
Baryte Min.
Reverse Fault*
Normal Fault
Transtensional Fault
*Reactivated as normal fault
≈ 237 ma Sk Skuld Fm.
Sa Sassendalen Gp.
≈ 255 ma Te Tempelfjorden Gp.
≈ 419 - 393 ma Bi Billefjorden Gp.
≈ 650 - 541 ma Ru Russehamna Fm.
≈ 485 - 470 ma Sø Sørhamna Fm.
UY Up. Ymerdalen Fm.
≈ 470 - 458 ma
LY Lw. Ymerdalen Fm.
Barents Sea
Russehamna
Kvalrossbukta
Sørhamna
Blyhatten Mine
Ymerdalen
Antarcticfjellet
Hambergfjellet
Fuglefjellet
Sørlia
Skrekkgjuvet
N
1000 m

731

732 Fig. 4

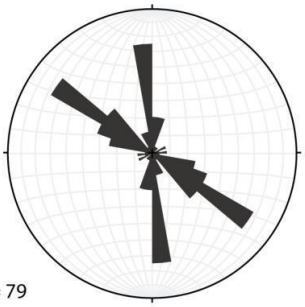

a.
N = 79
Standard Deviation of Elevation 100 x 100

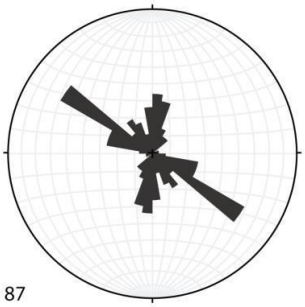

b.
N = 87
Standard Deviation of Elevation 25 x 25

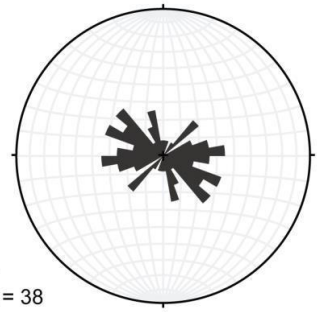

c.
N = 38
Filtered magnetic continuation lineation

733

734 Fig. 5

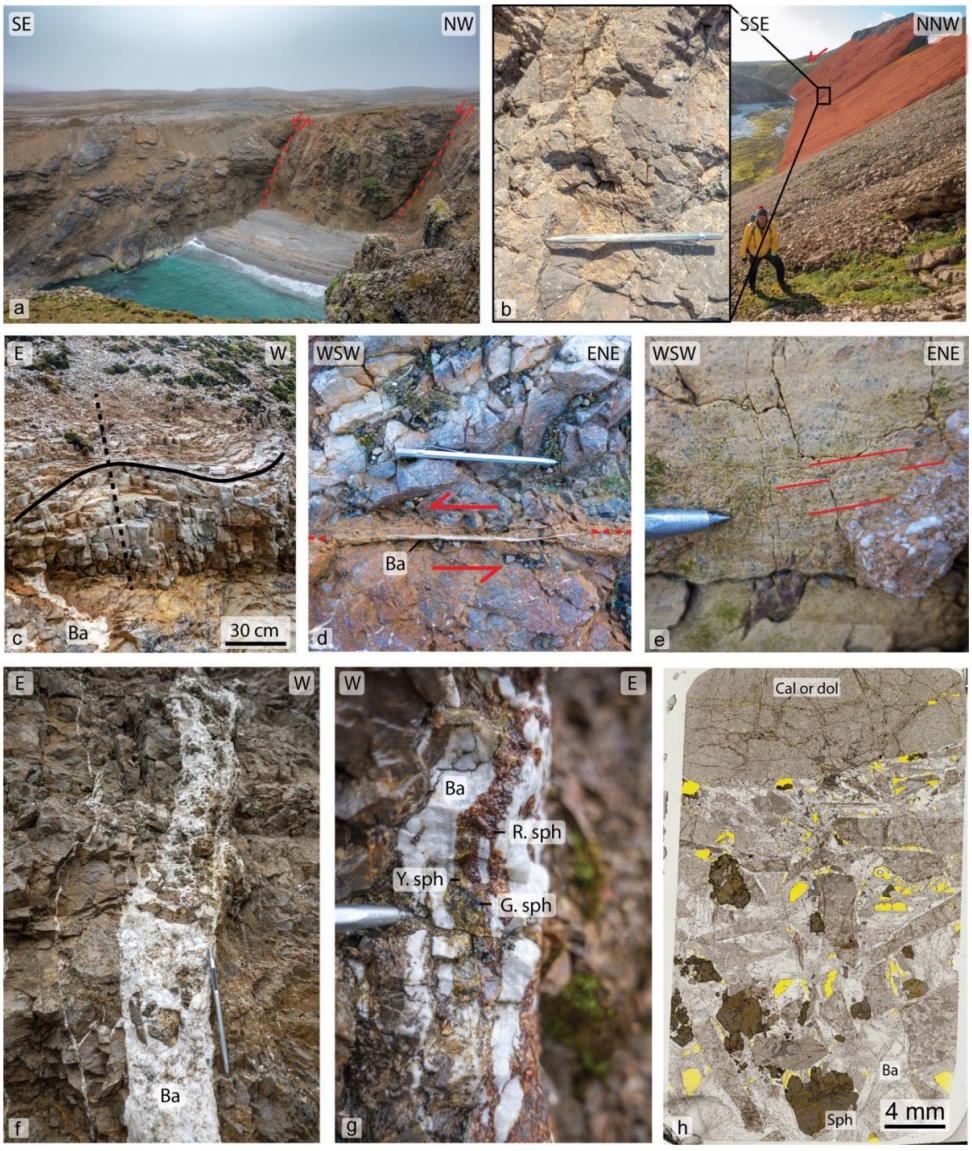
SE
NW
a
b
SSE
NNW
E
W
c
Ba
30 cm
WSW
ENE
d
Ba
WSW
ENE
e
E
W
f
Ba
W
E
g
Ba
R. sph
Y. sph
G. sph
Cal or dol
Ba
Sph
4 mm
h

735

736 Fig. 6

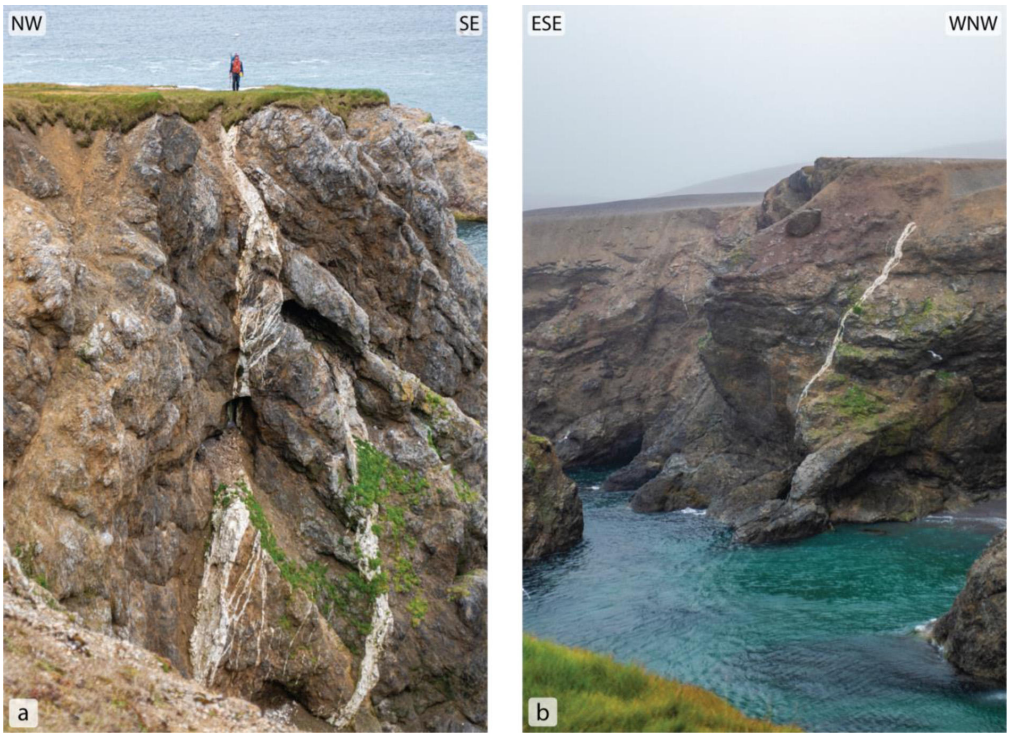

Fig. 7

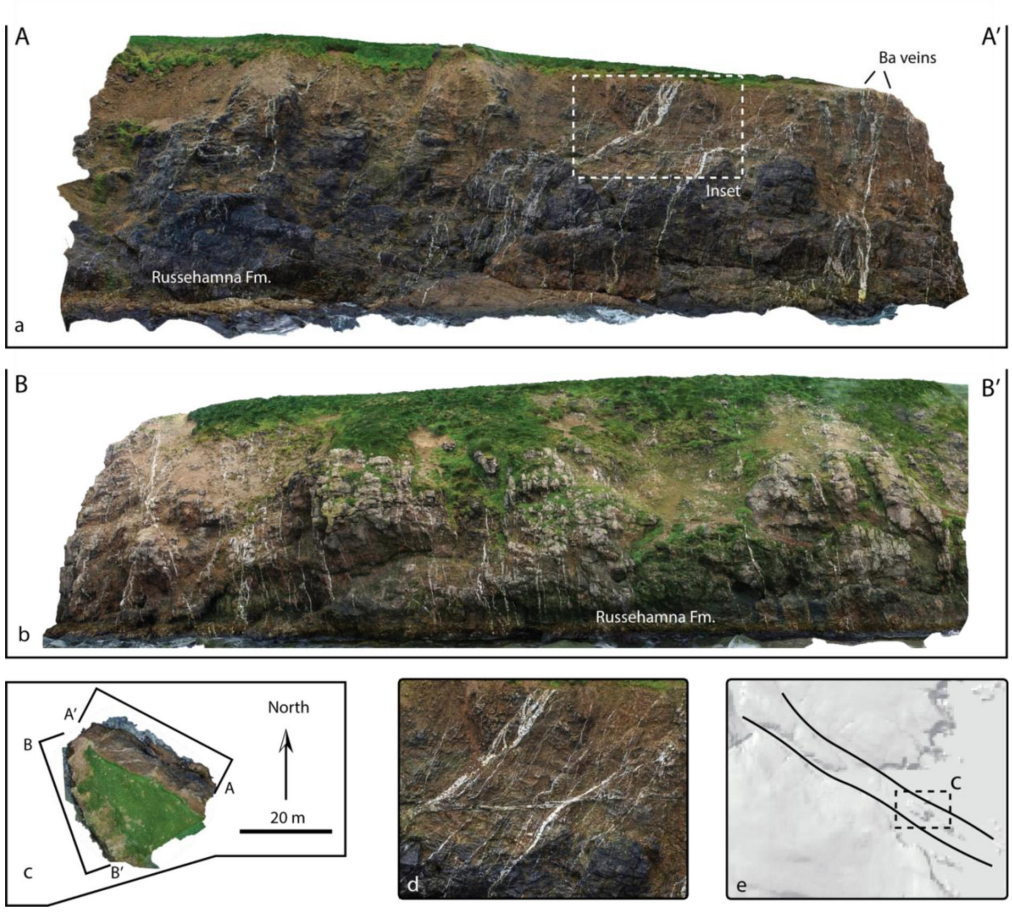
A
A′
Ba veins
Inset
Russehamna Fm.
a
B
B′
Russehamna Fm.
b
A′
B
A
North
20 m
B′
c
d
C
e

739

740 Fig. 8

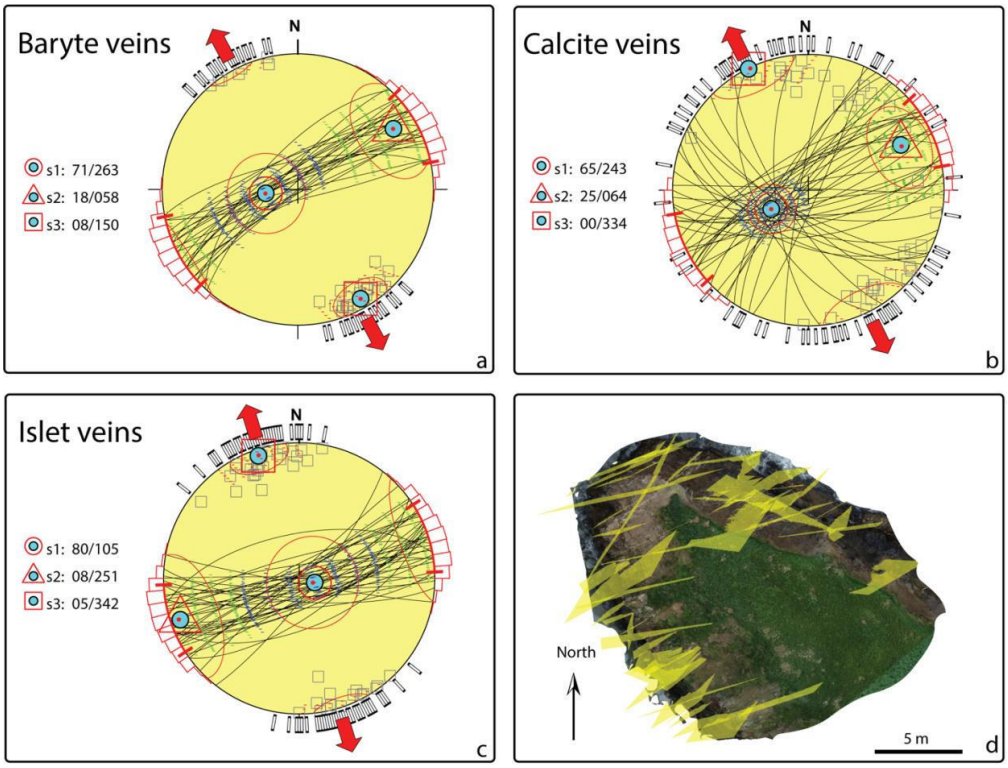
Baryte veins
N
s1: 71/263
s2: 18/058
s3: 08/150
a
Calcite veins
N
s1: 65/243
s2: 25/064
s3: 00/334
b
Islet veins
N
s1: 80/105
s2: 08/251
s3: 05/342
c
North
5 m
d

Fig. 9

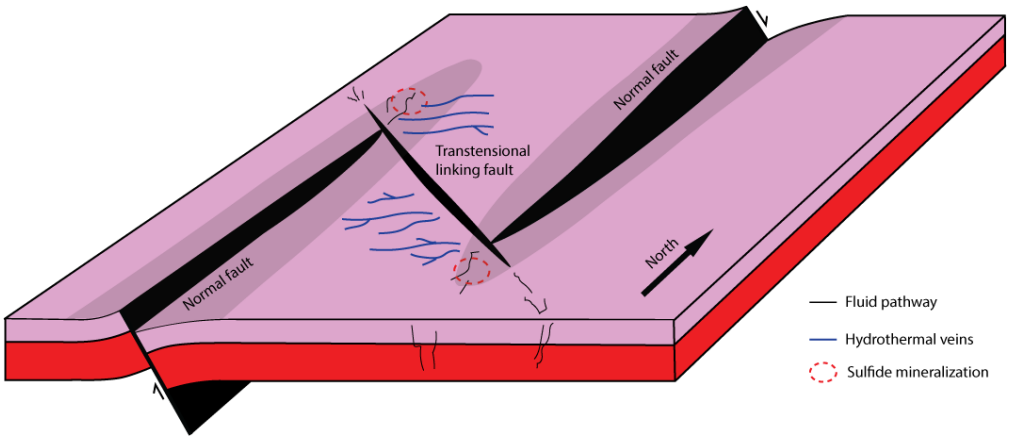

746

747 Fig. 10

748

Table 1 - Principal stress axes from the kinematic analysis

	Principal Stress Tensors		
	Baryte veins	Calcite veins	Islet veins
n	49	57	43
σ1	71 / 263	65 / 243	80 / 105
σ2	18 / 058	25 / 064	08 / 251
σ3	08 / 150	00 / 334	05 / 342

9 Genesis of Pb – Zn mineralizations in the Barents Sea and consequences for offshore ore exploration on continental shelves

This paper is under review for publication and is therefore not included.

10 Epilogue

10.1 Introduction

This project investigated the onshore – offshore correlation of mineralized hydrothermal systems. By employing a combination of methods, from geophysical and field studies to microanalysis and geochemical investigations, we described in detail hydrothermal systems, related structural features, and local mineralizations, all with relevance to the offshore domain, particularly through their relation to rift zones and rifted margins. Our investigations into the role of hydrothermal fluids in deep rift settings, in epithermal systems on continental shelves, and the extrapolation of onshore knowledge to the offshore domain resulted in fruitful contributions, described below.

10.2 Answers to research questions

10.2.1 The role of hydrothermal systems in deep rift settings

Through our study of the Reinfjord Ultramafic Complex we highlighted the critical role fluids play in facilitating lower crustal deformation in rift zones. Fluids related to mafic dykes exploited microfractures within the peridotite host rock, causing volume-expanding metamorphic reactions and a grain size reduction, further fracturing and weaking the rocks. Deformation localized along the dyke – peridotite interface, first through crystal plastic mechanisms and later through transient brittle failure, forming wide-spread pseudotachylytes.

Had the Reinfjord Ultramafic Complex been a completely dry setting, the deformation observed in our study would not have taken place. Similar shear zones and deformation mechanisms may help explain the presence of CO_2-outgassing and deep earthquakes along modern day rifts, such as the East African Rift System. Further hydrothermal veins in proximal areas, rich in sulfides strengthen the link to ore deposits. These veins were studied during field work and sampled, but they were left out of this PhD allowing us to further focus on Bjørnøya, as an onshore analogue to mineralized hydrothermal on the continental shelf.

10.2.2 The role of hydrothermal systems in epithermal deposits on continental shelves

Hydrothermal fluids are, of course, paramount to many mineral deposits, including the epithermal sedimentary-hosted Pb – Zn mineralizations documented on Bjørnøya and the Barents Sea. Our studies help link such mineralizations to deep structures, such as detachment faults, and the hydrothermal systems which may form above them at shallow crustal levels. Through magnetic modelling we recreated the geometry of the fault systems across southeastern Bjørnøya. These fault systems can be directly linked to the mineralization through mineralized fault cores, and fault-related hydrothermal veins containing mineralized (Sph + Brt + Gn) breccia. NW – SE trending Transtensional faults linking larger NS trending normal faults created fluid pathways during active faulting. The mineralization on Bjørnøya is compared with another Sph + Brt + Gn mineralization on the Loppa High. The two mineralizations relation to large scale structures, timing, and relation to rift events are all similar. The precise fluid and sulfur sources between the mineralizations may vary, though fluid mixing between connate seawater and crustal sources is suspected in both cases. The connection between hydrothermal systems and deep structures allows us to extrapolate our findings to similar settings, recognizable in potential field data which is widely available across most continental shelves.

10.2.3 The extrapolation of onshore data to the nearshore and offshore domains

Using potential field, seismic, and well core data we demonstrated a potential to find mineralizations within the subsea domain. The wealth of geological data collected by the petroleum industry over the last 50 years across Norwegian continental shelves may be reprocessed, helping discover new mineral deposits in Norwegian waters. The same approach could be refined and applied to more areas, making complex offshore prospecting more palatable through the onshore – offshore correlation of mineralized hydrothermal systems.

10.2.4 The role of hydrothermal systems in island arc deposits

While our investigation into the Lykling gold deposit emplaced within an island arc setting was cut short following circumstances outside our control, our initial analyses suggest a clear link between fluids, deformation, and mineralization. Further work, including more detailed structural, fluid inclusion, and isotope analyses would most certainly document the specifics of this relationship, reconciling the formation of the Lykling gold deposit with local and regional geological processes. Good geophysical coverage, the presence of available well-cores, and a growing body of work regarding the influence of basement fractures like those observed on Lykling on offshore hydrocarbons makes the gold deposits and ideal candidate for further work into the onshore – offshore correlation of ore-forming hydrothermal systems.

10.3 Conclusion

As the demand for mineral resources continues to grow, geoscientists will be forced to explore new frontiers, including submerged continental shelves. The continuation of fertile onshore domains and geological features to the subsea domain suggests the presence of rich mineral resources in relatively near shore settings. By expanding our knowledge of rift systems, sedimentary basins, and other near-shore geological features, we contribute to our understanding of the resource-forming systems in the offshore domain. By helping to close the knowledge gap between present day knowledge, and that which will be required to develop resources in offshore settings, we hope to contribute to the development of resources important or a greener future, if possible, through environmentally responsible practices.

11 References

Amaliksen, K. 1980. Gullkorekomster på Bømlo. *In:* UNDERSØKELSE, N. G. (ed.).

Andersen, T. B., Jamtveit, B., Dewey, J. F. & Swensson, E. 1991. Subduction and eduction of continental crust: Major mechanisms during continent-continent collision and orogenic extensional collapse, a model based on the south Norwegian Caledonides. *Terra Nova,* 3**,** 303-310.

Andersson, J. G. 1901. *Über die Stratigraphie und Tektonik der Bären-Insel*, Almqvist & Wiksell.

Arndt, N. T., Fontboté, L., Hedenquist, J. W., Kesler, S. E., Thompson, J. F. H. & Wood, D. G. 2017. Future Global Mineral Resources. *Geochemical Perspectives***,** 1-171.

Beaulieu, S. E., Graedel, T. E. & Hannington, M. D. 2017. Should we mine the deep seafloor? *Earth's Future,* 5**,** 655-658.

Bebbington, A., Hinojosa, L., Bebbington, D. H., Burneo, M. L. & Warnaars, X. 2008. Contention and Ambiguity: Mining and the Possibilities of Development. *Development and Change,* 39**,** 887-914.

Blaich, O. A., Tsikalas, F. & Faleide, J. I. 2017. New insights into the tectono-stratigraphic evolution of the southern Stappen High and its transition to Bjørnøya Basin, SW Barents Sea. *Marine and Petroleum Geology,* 85**,** 89-105.

Blanks, D. E., Holwell, D. A., Fiorentini, M. L., Moroni, M., Giuliani, A., Tassara, S., González-Jiménez, J. M., Boyce, A. J. & Ferrari, E. 2020. Fluxing of mantle carbon as a physical agent for metallogenic fertilization of the crust. *Nature Communications,* 11.

Blundell, D. J., Karnkowski, P. H., Alderton, D. H. M., Oszczepalski, S. & Kucha, H. 2003. COPPER MINERALIZATION OF THE POLISH KUPFERSCHIEFER: A PROPOSED BASEMENT FAULT-FRACTURE SYSTEM OF FLUID FLOW. 98**,** 1487-1495.

Boyd, R., Bjerkgård, T., Nordahl, B. & Schiellerup, H. 2016. Mineral Resources in the Arctic Geological Survey of Norway.

Braathen, A., Maher, H. D., Haabet, T. E., Kristensen, S. E., Tørudbakken, B. O. & Worsley, D. 1999. Caledonian thrusting on Bjørnøya: Implications for Palaeozoic and Mesozoic tectonism of the western Barents Shelf. *Norsk Geologisk Tidsskrift,* 79**,** 57-68.

Clark, S. A., Glorstad-Clark, E., Faleide, J. I., Schmid, D., Hartz, E. H. & Fjeldskaar, W. 2014. Southwest Barents Sea rift basin evolution: comparing results from backstripping and time-forward modelling. *Basin Research,* 26**,** 550-566.

Cocks, L. R. M. & Torsvik, T. H. 2005. Baltica from the late Precambrian to mid-Palaeozoic times: the gain and loss of a terrane's identity. *Earth-Science Reviews,* 72**,** 39-66.

Corfu, F., Andersen, T. & Gasser, D. 2014. The Scandinavian Caledonides: main features, conceptual advances and critical questions. *Geological Society, London, Special Publications,* 390**,** 9-43.

Curewitz, D. & Karson, J. A. 1997. Structural settings of hydrothermal outflow: Fracture permeability maintained by fault propagation and interaction. *Journal of Volcanology and Geothermal Research,* 79**,** 149-168.

Daly, J. S., Balagansky, V. V., Timmerman, M. J. & Whitehouse, M. J. 2006. The Lapland-Kola orogen: Palaeoproterozoic collision and accretion of the northern Fennoscandian lithosphere. *Geological Society, London, Memoirs,* 32**,** 579-598.

Davidheiser-Kroll, B., Stuart, F. & Boyce, A. 2014. Mantle heat drives hydrothermal fluids responsible for carbonate-hosted base metal deposits: evidence from 3 He/4 He of ore fluids in the Irish Pb-Zn ore district. *Mineralium Deposita,* 49**,** 547-553.

Delvaux, D. Release of program Win-Tensor 4.0 for tectonic stress inversion: statistical expression of stress parameters. Geophysical research abstracts, 2012. EGU General Assembly Vienna.

Ellefmo, S. L. 2022. Conceptual 3D Modeling and Direct Block Scheduling of a Massive Seafloor Sulfide Occurrence. *Perspectives on Deep-Sea Mining.* Springer.

Ernst, R. & Bleeker, W. 2010. Large igneous provinces (LIPs), giant dyke swarms, and mantle plumes: significance for breakup events within Canada and adjacent regions from 2.5 Ga to the Present. *Canadian Journal of Earth Sciences,* 47**,** 695-739.

Faleide, J. I., Tsikalas, F., Breivik, A. J., Mjelde, R., Ritzmann, O., Engen, O., Wilson, J. & Eldholm, O. 2008. Structure and evolution of the continental margin off Norway and the Barents Sea. *Episodes,* 31**,** 82-91.

Faleide, J. I., Vågnes, E. & Gudlaugsson, S. T. 1993. Late Mesozoic-Cenozoic evolution of the south-western Barents Sea in a regional rift-shear tectonic setting. *Marine and Petroleum Geology,* 10**,** 186-214.

Fetter, N., Blichert-Toft, J., Ludden, J., Lepland, A., Sánchez Borque, J., Greenhalgh, E., Garcia, B., Edwards, D., Télouk, P. & Albarède, F. 2019. Lead isotopes as tracers of crude oil migration within deep crustal fluid systems. *Earth and Planetary Science Letters,* 525**,** 115747.

Fichler, C. & Pastore, Z. 2022. Petrology of the crystalline crust in the southwestern Barents Sea inferred from geophysical data. *Norwegian Journal of Geology***,** 40.

Finlay, A. J., Selby, D., Osborne, M. J. & Finucane, D. J. G. 2010. Fault-charged mantle-fluid contamination of United Kingdom North Sea oils: Insights from Re-Os isotopes. 38**,** 979-982.

Flood, B. 1967. Sulphide mineralizations within the Hecla Hoek complex in Vestspitsbergen and Bjørnøya. *Norsk Polarinstitutt Årbok,* 1967**,** 109-127.

Fossen, H. & Hurich, C. a. J. J. O. T. G. S. 2005. The Hardangerfjord Shear Zone in SW Norway and the North Sea: a large-scale low-angle shear zone in the Caledonian crust. 162**,** 675-687.

Gabrielsen, R. H., Faerseth, R. B. & Jensen, L. N. 1990. *Structural elements of the Norwegian continental shelf. Pt. 1. The Barents Sea region*, Norwegian Petroleum Directorate.

Gac, S., Hansford, P. A. & Faleide, J. I. 2018. Basin modelling of the SW Barents Sea. *Marine and Petroleum Geology,* 95**,** 167-187.

Gee, D. 1975. A tectonic model for the central part of the Scandinavian Caledonides. *American Journal of Science,* 275**,** 468-515.

Gee, D. G., Fossen, H., Henriksen, N. & Higgins, A. K. 2008. From the early Paleozoic platforms of Baltica and Laurentia to the Caledonide Orogen of Scandinavia and Greenland. *Episodes,* 31**,** 44-51.

Gernigon, L. & Brönner, M. 2012. Late Palaeozoic architecture and evolution of the southwestern Barents Sea: insights from a new generation of aeromagnetic data. *Journal of the Geological Society,* 169**,** 449-459.

Gernigon, L., Brönner, M., Dumais, M.-A., Gradmann, S., Grønlie, A., Nasuti, A. & Roberts, D. 2018. Basement inheritance and salt structures in the SE Barents Sea: Insights from new potential field data. *Journal of Geodynamics,* 119**,** 82-106.

Gernigon, L., Brönner, M., Roberts, D., Olesen, O., Nasuti, A. & Yamasaki, T. 2014. Crustal and basin evolution of the southwestern Barents Sea: From Caledonian orogeny to continental breakup. *Tectonics,* 33**,** 347-373.

Glørstad-Clark, E. 2011. Basin analysis in the western Barents Sea area: the interplay between accommodation space and depositional systems. *University of Oslo, Oslo, doi,* 10.

Grant, T. B., Larsen, R. B., Anker-Rasch, L., Grannes, K. R., Iljina, M., Mcenroe, S., Nikolaisen, E., Schanche, M. & Øen, E. 2016. Anatomy of a deep crustal volcanic conduit system; The Reinfjord Ultramafic Complex, Seiland Igneous Province, Northern Norway. *Lithos,* 252-253**,** 200-215.

Green, P. & Duddy, I. Synchronous exhumation events around the Arctic including examples from Barents Sea and Alaska North Slope. Geological Society, London, Petroleum Geology Conference series, 2010. Geological Society of London, 633-644.

Gresseth, J. L. S., Braathen, A., Serck, C. S., Faleide, J. I. & Osmundsen, P. T. 2021. Late Paleozoic supradetachment basin configuration in the southwestern Barents Sea—Intrabasement seismic facies of the Fingerdjupet Subbasin. *Basin Research*.

Gudlaugsson, S., Faleide, J., Johansen, S. & Breivik, A. 1998. Late Palaeozoic structural development of the south-western Barents Sea. *Marine and Petroleum Geology,* 15**,** 73-102.

Gumsley, A., Manby, G., Domańska-Siuda, J., Nejbert, K. & Michalski, K. 2020. Caught between two continents: first identification of the Ediacaran Central Iapetus Magmatic Province in Western Svalbard with palaeogeographic implications during final Rodinia breakup. *Precambrian Research***,** 105622.

Hannington, M., Petersen, S. & Krätschell, A. J. N. G. 2017. Subsea mining moves closer to shore. 10**,** 158.

Harris, P., Macmillan-Lawler, M., Rupp, J. & Baker, E. 2014. Geomorphology of the oceans. *Marine Geology,* 352**,** 4-24.

Hartz, E. H. & Torsvik, T. H. 2002. Baltica upside down: a new plate tectonic model for Rodinia and the Iapetus Ocean. *Geology,* 30**,** 255-258.

Hein, J. R., Mizell, K., Koschinsky, A. & Conrad, T. A. 2013. Deep-ocean mineral deposits as a source of critical metals for high-and green-technology applications: Comparison with land-based resources. *Ore Geology Reviews,* 51**,** 1-14.

Holtedahl, O. 1920. On the Paleozoic series of Bear Island, especially on the Heclahook system: Norsk Geol. Tidsskr.

Indrevær, K., Gabrielsen, R. H. & Faleide, J. I. 2017. Early Cretaceous synrift uplift and tectonic inversion in the Loppa High area, southwestern Barents Sea, Norwegian shelf. *Journal of the Geological Society,* 174**,** 242-254.

Indrevær, K., Gac, S., Gabrielsen, R. H. & Faleide, J. I. 2018. Crustal-scale subsidence and uplift caused by metamorphic phase changes in the lower crust: a model for the evolution of the Loppa High area, SW Barents Sea from late Paleozoic to Present. *Journal of the Geological Society,* 175**,** 497-508.

Koehl, J.-B., Polonio, I. & Rojo, L. A. 2022. *The nature of basement rocks in the Loppa High revealed by new 3D seismic attribute and spectral decomposition*.

Larsen, R. B., Grant, T., Sørensen, B. E., Tegner, C., Mcenroe, S., Pastore, Z., Fichler, C., Nikolaisen, E., Grannes, K. R., Church, N., Ter Maat, G. W. & Michels, A. 2018. Portrait of a giant deep-seated magmatic conduit system: The Seiland Igneous Province. *Lithos,* 296-299**,** 600-622.

Lawrence, R. & Moritz, S. 2019. Mining industry perspectives on indigenous rights: Corporate complacency and political uncertainty. *The Extractive Industries and Society,* 6**,** 41-49.

Leach, D. L., Sangster, D. F., Kelley, K. D., Large Ross, R., Garven, G. & Allen, C. R. 2005. Sediment-hosted Pb-Zn Deposits: a global perspective. *Economic Geology,* 100**,** 561-608.

Leclerc, F., Feuillet, N. & Deplus, C. 2016. Interactions between active faulting, volcanism, and sedimentary processes at an island arc: Insights from Les Saintes channel, Lesser Antilles arc. *Geochemistry, Geophysics, Geosystems,* 17**,** 2781-2802.

Lee, H., Muirhead, J. D., Fischer, T. P., Ebinger, C. J., Kattenhorn, S. A., Sharp, Z. D. & Kianji, G. 2016. Massive and prolonged deep carbon emissions associated with continental rifting. *Nature Geoscience,* 9**,** 145-149.

Lepvrier, C., Leparmentier, F. & Seland, R. 1989. Upper Palaeozoic faulting regimes in Bjornoya (Svalbard, Norway). *Bulletin de la Société géologique de France***,** 411-416.

Lesage, M. 2020. A framework for evaluating deep sea mining systems for seafloor ma ssive sul phides deposits.

Lowenstern, J. 2001. Carbon dioxide in magmas and implications for hydrothermal systems. *Mineralium Deposita,* 36**,** 490-502.

Miller, K. A., Thompson, K. F., Johnston, P. & Santillo, D. 2018. An overview of seabed mining including the current state of development, environmental impacts, and knowledge gaps. *Frontiers in Marine Science*, 418.

Mitchell, A. H. & Bell, J. D. 1973. Island-Arc Evolution and Related Mineral Deposits. *The Journal of Geology,* 81, 381-405.

Nordås, J., Amaliksen, K., Brekke, H., Suthern, R., Furnes, H., Sturt, B., Robins, B. & Gee, D. 1985. Lithostratigraphy and petrochemistry of Caledonian rocks on Bømlo, SW Norway. *The Caledonide Orogen—Scandinavia and Related Areas: New York, John Wiley & Sons Ltd*, 679-692.

Olesen, O., Brönner, M., Ebbing, J., Gellein, J., Gernigon, L., Koziel, J., Lauritsen, T., Myklebust, R., Pascal, C. & Sand, M. New aeromagnetic and gravity compilations from Norway and adjacent areas: methods and applications. Geological Society, London, Petroleum Geology Conference series, 2010. Geological Society of London, 559-586.

Pastore, Z., Fichler, C. & Mcenroe, S. A. 2016. The deep crustal structure of the mafic–ultramafic Seiland Igneous Province of Norway from 3-D gravity modelling and geological implications. *Geophysical Journal International,* 207, 1653-1666.

Pedersen, R. B. & Dunning, G. R. 1997. Evolution of arc crust and relations between contrasting sources: U-Pb (age), Nd and Sr isotope systematics of the ophiolitic terrain of SW Norway. *Contributions to Mineralogy and Petrology,* 128, 1-15.

Piaoer, F., Qingyan, T., Mingjie, Z., Zhaowei, Z., Liwu, L. & Wenyuan, L. 2012. Ore Genesis of the Kalatongke Cu-Ni Sulfide Deposits, Western China: Constraints from Volatile Chemical and Carbon Isotopic Compositions. *Acta Geologica Sinica - English Edition,* 86, 568-578.

Ritzmann, O. & Faleide, J. I. 2007. Caledonian basement of the western Barents Sea. 26, n/a-n/a.

Robb, L. 2004. *Introduction to ore-forming processes*, Blackwell publishing.

Robert, B., Domeier, M. & Jakob, J. 2021. On the origins of the Iapetus ocean. *Earth-Science Reviews,* 221, 103791.

Roberts, D. & Siedlecka, A. 2002. Timanian orogenic deformation along the northeastern margin of Baltica, Northwest Russia and Northeast Norway, and Avalonian–Cadomian connections. *Tectonophysics,* 352, 169-184.

Roberts, R. J., Corfu, F., Torsvik, T. H., Ashwal, L. D. & Ramsay, D. M. 2006. Short-lived mafic magmatism at 560–570 Ma in the northern Norwegian Caledonides: U–Pb zircon ages from the Seiland Igneous Province. 143**,** 887.

Rona, P. A. 2008. The changing vision of marine minerals. *Ore Geology Reviews,* 33**,** 618-666.

Ryan, E., Fichler, C., Sørensen, B., Larsen, R. & Viola, G. Onshore - Offshore Correlation of Ore-forming Hydrothermal Systems: A First Look. Winter Meeting, 2019 Bergen, Norway. Geological Society of Norway.

Ryan, E. J., Sørensen, B. E., Drivenes, K. & Larsen, R. B. 2022. Infiltration of volatile-rich mafic melt in lower crustal peridotites provokes lower crustal earthquakes. *Journal of Structural Geology,* 163**,** 104708.

Schmidt Mumm, A. & Wolfgramm, M. 2004. Fluid systems and mineralization in the north German and Polish basin. 4**,** 315-328.

Segalstad, T. 2006. Stable isotope evidence for ba-pb-zn vein mineralizations by fluid circulation in the sedimentary basin at Svalbard/Segalstad TV, Sundblad K. & Kjærnet T. *geological Survey of finland bulletin*.

Serck, C. S., Faleide, J. I., Braathen, A., Kjølhamar, B. & Escalona, A. 2017. Jurassic to early cretaceous basin configuration (s) in the Fingerdjupet Subbasin, SW Barents Sea. *Marine and Petroleum Geology,* 86**,** 874-891.

Sørensen, B. E., Grant, T., Ryan, E. J. & Larsen, R. B. 2019. In situ evidence of earthquakes near the crust mantle boundary initiated by mantle CO2 fluxing and reaction-driven strain softening. *Earth and Planetary Science Letters,* 524**,** 115713.

Torsvik, T. H. & Cocks, L. R. M. 2005. Norway in space and time: a centennial cavalcade. *Norwegian Journal of Geology/Norsk Geologisk Forening,* 85.

Van Doorn, E., Laugesen, J., Haeckel, M., Mestre, N., Skjeret, F. & Vink, A. 2022. Risk Assessment for Deep-Seabed Mining. Springer International Publishing.

Vidal, O., Le Boulzec, H., Andrieu, B. & Verzier, F. 2021. Modelling the Demand and Access of Mineral Resources in a Changing World. *Sustainability,* 14**,** 11.

Wedding, L., Reiter, S., Smith, C., Gjerde, K., Kittinger, J., Friedlander, A., Gaines, S., Clark, M., Thurnherr, A. & Hardy, S. 2015. Managing mining of the deep seabed. *Science,* 349**,** 144-145.

Worslex, D., Agdestein, T., Gjelberg, J. G., Kirkemo, K., Mørk, A., Nilsson, I., Olaussen, S., Steel, R. J. & Stemmerik, L. 2001. The geological evolution of Biørnøya, Arctic Norway: implications for the Barents Shelf. *Norwegian Journal of Geology/Norsk Geologisk Forening,* 81.

Worsley, D., Agdestein, T., Gjelberg, J. G., Kirkemo, K., Mørk, A., Nilsson, I., Olaussen, S., Steel, R. J. & Stemmerik, L. 2001. The geological evolution of Biørnøya, Arctic Norway: implications for the Barents Shelf. *Norwegian Journal of Geology/Norsk Geologisk Forening,* 81.

Wullf, P. W. 1993. En Befaring af ca 100 mineraliseringer i Sunnhordland, SV-Norge.

12 List of publications

The author, Eric James Ryan, participated in the following publications (in chronological order) during the project period of this thesis. The list includes both journal articles and conference proceedings. The three final publications (17, 18, and 19) constitute chapters within this thesis, while the remainder of the publications either supplement this work or encompass other work in the field of geology. Publications in which Eric James Ryan is first author or noted with the authors name in bold.

1. **Ryan, E.J.,** Fichler, C., Sørensen, B.E., Larsen, R.B. and Viola, G.A. (2019, January). Onshore – Offshore correlation of mineral systems along the Norwegian Continental Shelf: A first look. In *Abstract and Proceedings of the Geological Society of Norway (p. 84).*

2. **Ryan, E.J.,** Viola, G. & Sørensen, B.E. (2019, January). Structural Evolution of the Eastern Elba Nappe Stack, innermost Northern Apennines, Central Italy. In *Abstract and Proceedings of the Geological Society of Norway (p. 84).*

3. Sørensen, B.E.*, Grant, T., Larsen, R., Ryan, E.J. & Voll, M.O. (2019, January). Strain localization induced by late magmatic flux and reaction-driven strain softening, effects of primary mineralogy on the rheological response during reaction. In *Abstract and Proceedings of the Geological Society of Norway (p. 98).*

4. Sørensen, B. E., Grant, T., Ryan, E. J., & Larsen, R. B. (2019). In situ evidence of earthquakes near the crust mantle boundary initiated by mantle CO2 fluxing and reaction-driven strain softening. *Earth and Planetary Science Letters*, *524*, 115713.

5. Larsen, R. B., Sørensen, B. E., Nikolaisen, E., Orvik, A. A., & Ryan, E. J. (2019, December). Asthenospheric Mafic-Ultramafic Melts are Dripping Wet at Emplacement in

the Deep Lithosphere. Evidence From the Ediacaran age Seiland Igneous Province, N. Norway. In *AGU Fall Meeting Abstracts* (Vol. 2019, pp. V13C-0164).

6. **Ryan, Eric James**, Bjorn Eske Sorensen, and Rune B. Larsen. "Understanding Sulfide Mineralization in the Reinfjord Ultramafic Complex: Field study, microanalysis and thermodynamic modeling." *AGU Fall Meeting Abstracts*. Vol. 2019. 2019.

7. Sørensen, B. E., Larsen, R. B., Grant, T., Ryan, E. J., Orvik, A. A., & Sakariasen, J. (2019, December). Impact of volatiles and variations in local bulk composition on deformation and magma emplacement processes in the deep crust and upper mantle parts of continental rift systems. In *AGU Fall Meeting Abstracts* (Vol. 2019, pp. V31H-0085).

8. **Ryan, E.J.,** Sørensen, B.E. & Larsen, R.B (2020, January). Hydrothermal ore-forming processes in the deep-seated parts of a continental rift system and implications for hydrothermal processes in rift-related systems on the Norwegian continental shelf. In *Abstract and Proceedings of the Geological Society of Norway The 34th Nordic Geological Winter Meeting (p. 186).*

9. Ceccato, A., Viola, G., Antonellini, M., Tartaglia, G., & Ryan, E. J. (2020, May). In-situ petrophysical and geomechanical characterization and 3D modelling of a mature normal fault zone (Goddo fault, Bømlo-Norway). In *EGU General Assembly Conference Abstracts* (p. 6691).

10. Papeschi, S., Musumeci, G., Massonne, H. J., Mazzarini, F., Ryan, E. J., & Viola, G. (2020). High-P (P= 1.5–1.8 GPa) blueschist from Elba: Implications for underthrusting and exhumation of continental units in the Northern Apennines. *Journal of Metamorphic Geology*, *38*(5), 495-525.

11. **Ryan, E**., Papeschi, S., Viola, G., Musumeci, G., Mazzarini, F., Torgersen, E., ... & Ganerød, M. (2021). Syn-orogenic exhumation of high-P units by upward extrusion in an accretionary wedge: Insights from the Eastern Elba nappe stack (Northern Apennines, Italy). *Tectonics*, *40*(5), e2020TC006348.

12. Ceccato, A., Viola, G., Antonellini, M., Tartaglia, G., & Ryan, E. J. (2021). Constraints upon fault zone properties by combined structural analysis of virtual outcrop models and discrete fracture network modelling. *Journal of Structural Geology*, *152*, 104444.

13. Papeschi, S., Ryan, E., Musumeci, G., Mazzarini, F., Garofalo, P. S., & Viola, G. (2021). Geology of the Northern Apennines nappe stack on eastern Elba (Italy): new insights on the Neogene orogenic evolution of the Northern Tyrrhenian Sea. *Journal of Maps*, *17*(2), 533-546.

14. Sørensen, B. E., Ryan, E., Larsen, R., Drivenes, K., & Grant, T. (2021, December). Effect of volume expansion on style of mineral reactions during mixed-volatile infiltration in ultramafic-mafic rocks from the Reinfjord lower crustal field laboratory. In *AGU Fall Meeting Abstracts* (Vol. 2021, pp. V54C-01).

15. **Ryan, E**., Sørensen, B. E., Larsen, R., & Drivenes, K. (2021, December). The Development of Shear Zones in a Lower Crustal Continental Rift Zone. In *AGU Fall Meeting Abstracts* (Vol. 2021, pp. T45D-0262).

16. Sørensen, B. E., Ryan, E. J., Larsen, R., & Grant, T. (2022). *Infiltration of volatile-rich mafic melt in lower crustal peridotites provokes deep earthquakes, initiates km scale shear zones and volatile transfer from the lower crust to the atmosphere* (No. EGU22-10545). Copernicus Meetings.

17. **Ryan, E. J**., Sørensen, B. E., Drivenes, K., & Larsen, R. B. (2022). Infiltration of volatile-rich mafic melt in lower crustal peridotites provokes lower crustal earthquakes. *Journal of Structural Geology*, 104708.

18. **Ryan, E. J**., Sørensen, B. E., Fichler, C., Larsen, R. B., Gresseth, J. L., Bjørlykke, A. (2022). *Fault linkage on southeastern Bjørnøya: Implications for structural interpretations surrounding fertile ore-forming fault systems offshore*. Norwegian Journal of Geology, (In press).

19. **Ryan, E. J.,** Sørensen, B. E., Larsen, R. B., Fichler, C., Bjørlykke, A., Drivenes, K. (2022) *Genesis of Pb – Zn mineralizations in the Barents Sea and consequences for offshore ore exploration on continental shelves.* Ore Geology Reviews, (in review)

ISBN 978-82-326-6754-3 (printed ver.)
ISBN 978-82-326-5879-4 (electronic ver.)
ISSN 1503-8181 (printed ver.)
ISSN 2703-8084 (online ver.)

NTNU

Norwegian University of
Science and Technology